POLYTECHNIQUE MONTRÉAL
affiliée à l'Université de Montréal

RANS Computation of Heat Transfer Over Rough Surfaces

AVIRAL PRAKASH
Département de génie mécanique

Mémoire présenté en vue de l'obtention du diplôme de *Maîtrise ès sciences appliquées*
Génie aérospatial

Juin 2019

POLYTECHNIQUE MONTRÉAL
affiliée à l'Université de Montréal

Ce mémoire intitulé :

RANS Computation of Heat Transfer Over Rough Surfaces

présenté par **Aviral PRAKASH**
en vue de l'obtention du diplôme de *Maîtrise ès sciences appliquées*
a été dûment accepté par le jury d'examen constitué de :

Jérôme VÉTEL, président
Éric LAURENDEAU, membre et directeur de recherche
Bruno BLAIS, membre

ACKNOWLEDGMENTS

First and foremost, I would like to thank my supervisor Dr. Eric Laurendeau for providing me with the opportunity to work on this interesting project. He was very supportive throughout the project, guided me aptly and gave me enough freedom to explore the research domain. This balance allowed me to realize my future in this research area.

Throughout my time here in Montreal, I was lucky to have an amazing company of colleagues. All of them were helpful in many ways. Whether it is technical or casual discussions over lunch, it helped me understand different perspectives and allowed me to de-stress. I would also like to thank all my friends outside of the workplace for generating a social atmosphere that allowed me to settle and prosper in the distinct multicultural environment offered by this city. The time spent during the masters had an immense contribution to my overall development.

The project was sponsored by NSERC Collaborative Research and Development Grant with Bombardier Aerospace. I would also like to thank Mitacs Inc. for their support through the Globalink Graduate Fellowship program. Earlier in 2016, I had a wonderful research internship experience under the supervision of Dr. Frédérick Gosselin and Dr. Eric Laurendeau as a part of Mitacs Globalink Research Internship Program 2016. This motivated me to come back to Polytechnique Montreal for my masters.

Lastly and most importantly, I would like to thank my parents for their incessant love and support.

RÉSUMÉ

Un modèle précis de simulation de la résistance au frottement et du transfert de chaleur sur des surfaces rugueuses est une exigence importante dans les domaines de la conception pour plusieurs industries. La résolution des équations RANS est une des méthodes de modélisation les plus réalisables dans le contexte industriel actuel et nécessite l'extension des modèles de turbulence RANS afin d'intégrer l'effet de rugosité.

Le présent travail étudie les approches issues de la littérature du modèle de turbulence à faible nombre de Reynolds et à nombre de Reynolds élevé (lois de paroi) pour simuler l'effet de la rugosité. Le transfert de chaleur sur les surfaces lisses est modélisé sur la base de l'hypothèse d'analogie de Reynolds. L'hypothèse n'est pas valable pour les surfaces rugueuses et conduit à une prédiction excessive du nombre de Stanton. L'objectif de ce mémoire est d'intégrer la correction thermique pour surmonter cette hypothèse dans les deux approches et améliorer la prévision du transfert de chaleur sur des surfaces rugueuses.

Tout d'abord, différentes extensions de rugosité pour les modèles de turbulence Spalart-Allmaras et $k-\omega$ SST sont implémentées dans le solveur RANS interne. La précision et la robustesse numérique de ces extensions sont discutées. La correction thermique par Aupoix est mise en œuvre pour surmonter l'hypothèse de l'analogie de Reynolds et l'amélioration des prévisions de transfert de chaleur est évaluée. La correction conduit à une meilleure cohérence dans la prédiction du coefficient de frottement et du nombre de Stanton.

Deuxièmement, les lois de paroi basées sur la loi logarithmique sont appliquées et étendues pour modéliser le flux et le transfert de chaleur sur des surfaces rugueuses. La mise en œuvre de lois de paroi rugueuses est compatible avec l'extension de rugosité du modèle de turbulence à faible nombre de Reynolds. La dépendance des lois de paroi à l'espacement par rapport à la paroi est évaluée pour des surfaces lisses et rugueuses avec une hauteur de rugosité variable. On observe que la loi de paroi ressemble au comportement physique attendu. La formulation actuelle de la loi de paroi donne des résultats supérieurs indépendants de l'espacement près de la paroi pour les surfaces rugueuses par rapport à d'autres formulations de lois de paroi rugueuses. Trois variantes de conditions aux limites approximatives pour le modèle de turbulence $k-\omega$ SST sont analysées et il est observé que la cohérence des variables de turbulence conduit à une amélioration des résultats. Le travail montre que l'hypothèse de l'analogie de Reynolds peut être utilisée comme stratégie efficace pour vérifier l'extension de la rugosité des lois de paroi. Trois corrections thermiques sont explorées pour améliorer la prévision du transfert de chaleur sur des surfaces rugueuses. La correction thermique de Aupoix est

étendue à l'approche de loi de paroi. L'approche actuelle surmonte quelques restrictions offertes par l'approche de la loi de paroi analytique. Les deux autres corrections reposent uniquement sur une échelle de rugosité c'est-à-dire une rugosité équivalente avec grains de sable, qui n'est pas adéquate pour modéliser avec précision le frottement et le transfert de chaleur. Ceci est exploré en considérant un cas avec deux types de rugosité différents produisant le même coefficient de frottement mais avec des nombres de Stanton différents. Il est observé que la correction Aupoix nécessite un paramètre physique supplémentaire en entrée et capture plus précisément la physique du transfert de chaleur. Cependant, la nécessité de paramètres physiques supplémentaires pourrait poser des problèmes de modélisation lorsque les données expérimentales sur la distribution de la rugosité ne sont pas disponibles. Les deux autres corrections ont montré un bon accord avec plusieurs cas expérimentaux et ont pu être utilisées en l'absence de données de géométrie de rugosité.

La discussion se termine en mentionnant les nombreuses limitations et difficultés numériques rencontrées lors de la modélisation de l'écoulement sur des surfaces rugueuses. Les futures orientations pour faire avancer les frontières de la recherche sont finalement proposées.

ABSTRACT

An accurate model for simulating friction drag and heat transfer over rough surfaces is a major requirement in the design and development domain of several industries. Computational modeling via the RANS equations is the most computationally feasible in today's industrial scenario and requires the extension of RANS turbulence models to incorporate the effect of roughness.

The present work discusses both the low-Reynolds and high-Reynolds number (Wall function) turbulence model approaches to simulate the effect of roughness. Heat transfer over smooth surfaces is often modeled based on the Reynolds analogy assumption. The assumption does not hold over rough surfaces and leads to an overprediction of Stanton number. The objective of this thesis is to incorporate the thermal correction overcoming the assumption in both approaches and improve the heat transfer prediction over rough surfaces.

Firstly, different roughness extensions proposed in the literature for the Spalart-Allmaras and $k-\omega$ SST turbulence models are implemented in an in-house RANS solver. The accuracy and numerical robustness of these extensions are discussed. The thermal correction by Aupoix is implemented to overcome the assumption of Reynolds analogy and the improvement in predictions of heat transfer is assessed. The correction leads to consistency in the prediction of the skin-friction coefficient and Stanton number.

Secondly, the log-law based wall functions are implemented and extended to model flow and heat transfer over rough walls. The implementation of rough wall functions is consistent with the low-Reynolds number turbulence model roughness extension. The near-wall spacing dependence characteristics of wall functions are assessed for smooth and rough walls with varying roughness heights. It is observed that the wall functions resemble the expected physical behavior. The present wall function formulation gives superior near-wall spacing independent results for rough walls compared to other rough wall function formulations. Three variants of rough boundary conditions for the $k-\omega$ SST turbulence model are analyzed, and it is observed that the consistency of turbulence variables leads to improved results. The work shows that the Reynolds analogy assumption can be used as an effective strategy to verify the roughness extension of wall functions. Three thermal corrections are explored to improve the heat transfer prediction over rough surfaces. The Aupoix thermal correction is extended to the wall function approach. The present approach overcomes a few restrictions offered by the Analytical Wall Function (AWF) approach. The other two corrections rely only on one roughness scale (equivalent sand-grain roughness) which is not adequate for accurate

modeling of both friction drag and heat transfer. This is explored by considering a case with two different roughness types resulting in same skin-friction coefficients but different Stanton numbers. It is observed that the Aupoix correction requires an additional physical parameter as input and captures the physics of heat transfer more accurately. However, the requirement of additional physical parameters could pose modeling constraints when the experimental roughness distribution data is not available. The other two corrections showed good agreement with several other experimental cases and could be used in the absence of roughness geometry data.

The discussion concludes by mentioning the several limitations and numerical difficulties experienced while modeling flows over rough surfaces. Future directions to advance the research frontiers are proposed.

TABLE OF CONTENTS

REFERENCES . . . 87

LIST OF TABLES

LIST OF FIGURES

LIST OF SYMBOLS AND ABBREVIATIONS

c	reference chord	m
C_f	skin friction coefficient	-
c_p	specific heat capacity at constant pressure	J/(kg · K]
h	roughness height	mm
k	turbulent kinetic energy	m^2/s^2
k_c	thermal conductivity	W/(m · K)
k_s	equivalent sand-grain roughness height	mm
Ma	Mach number	-
p	pressure	Pa
Pr	Prandtl number	-
Pr_t	turbulent Prandtl number	-
q	heat flux	W/ m^2
r	adiabatic recovery factor	-
Re	Reynolds number	-
S_{corr}	corrected surface area ratio	-
St	Stanton number	-
T	temperature	$^\circ$ C
u	wall-parallel velocity	m/s
u_i	velocity component in i-direction	m/s
x_i	cartesian co-ordinates in i-direction	m
y	wall-normal distance	m

Greek symbols

α	thermal diffusivity	J/(m^3· K)
δ	boundary layer thickness	m
κ	Von-karman constant	-
μ	dynamic viscosity	Pa · s
ν	kinematic viscosity	m^2/s
$\tilde{\nu}$	Spalart-Allmaras variable (modified eddy viscosity)	m^2/s
ρ	density	kg/m^3
τ	shear stress	Pa
ω	specific turbulence dissipation rate	s^{-1}

Subscripts and Superscripts

∞	freestream property
$+$	non-dimensionalised in inner region
ref	reference value
rms	root mean square value
r	rough wall
0	shifted wall value (for rough walls)
s	smooth wall
t	turbulent value
w	wall value

Abbreviations

AWF	Analytical Wall Functions
AoA	Angle of Attack
CFD	Computational Fluid Dynamics
DEM	Discrete Element Method
DNS	Direct Numerical Simulation
ESGR	Equivalent sand-grain roughness
HTC	Heat Transfer Coefficient
LES	Large-Eddy Simulation
WI	Low-Reynolds number turbulence model simulation
MATD	Matrix Artificial Dissipation
NS	Navier-Stokes
RANS	Reynolds Averaged Navier-Stokes
SST	Shear Stress Transport
WAF	Wall Function Simulation

LIST OF APPENDICES

CHAPTER 1 INTRODUCTION

Computational Fluid Dynamics (CFD) has evolved over the years and is imperative in the design and development process of several industries. Even though wind-tunnel experiments are still being used to improve CFD capabilities, their direct involvement in the industrial design process is limited. This rapidly expanding research area focuses on concepts of physics, mathematics, computer science and related disciplines. The work in this thesis constricts to the physical modeling aspect and involves improving models for incorporating additional physics.

1.1 Basic Concepts

The section discusses the concepts of fluid mechanics and turbulent flow simulations.

1.1.1 Navier-Stokes equations

The flow and heat transfer in a fluid is governed by a set of partial differential equations known as Navier-Stokes equations.

$$\frac{\partial \rho}{\partial t} + \frac{\partial}{\partial x_j}(\rho u_j) = 0 \tag{1.1}$$

$$\frac{\partial \rho u_i}{\partial t} + \frac{\partial}{\partial x_j}(\rho u_i u_j) = -\frac{\partial P}{\partial x_i} + \frac{\partial \tau_{ij}}{\partial x_j} \tag{1.2}$$

$$\frac{\partial \rho E}{\partial t} + \frac{\partial}{\partial x_j}(\rho E u_j) = -\frac{\partial}{\partial x_j}(P u_j) + \frac{\partial (u_i \tau_{ij})}{\partial x_j} + \frac{\partial}{\partial x_j}\left(k_c \frac{\partial T}{\partial x_j}\right) \tag{1.3}$$

where u_j are the components of velocity in x_j directions for $j = 1, 2, 3$. These equations are derived from the conservation of mass, momentum and energy in a control volume. Note that the variables ρ, u_j, E, T are instantaneous values of density, velocity vector, energy and temperature respectively.

Analytical solutions for Navier-Stokes equations exist, but they are limited to simple canonical cases, for example, laminar Couette flow. As the industrial needs correspond to high Reynolds number turbulent flows, there has been a lot of effort focusing on the numerical computation of these equations. Turbulent flows encompass eddies of varying time and

length scales. Proper resolution of Navier-Stokes equations provides the detailed solution of the flow-field in any situation. This is done in Direct Numerical Simulations (DNS). Another method is to resolve the larger eddies that are anisotropic, while the smallest eddies that have an isotropic nature are modeled. This method is known as the Large-Eddy Simulation (LES). With the increase in Reynolds number, the range of turbulent scales also increases which requires the use of a finer spatial and temporal grid. As a result, both LES and DNS are computationally expensive for the industrial flows. Even though the use of Hybrid RANS-LES is upcoming, the industries still rely on Reynolds Averaged Navier-Stokes (RANS) formulation.

1.1.2 Reynolds Averaged Navier-Stokes (RANS) equations

The time-varying and statistical nature of turbulence indicates that flow variables in turbulent flows can be simplified and decomposed into the sum of mean and fluctuating values. The flow variables (ϕ) are decomposed as,

$$\phi(x,t) = \overline{\phi}(x) + \phi'(x,t) \tag{1.4}$$

where the overbar (-) indicates the time-averaged value of the flow variables and the prime ($'$) denotes the difference between the flow variable and its time-averaged value. The time-averaged value is given as,

$$\overline{\phi}(x) = \lim_{T\to\infty} \frac{1}{T} \int_{t_0}^{t_0+T} \phi(x,t)\ dt \tag{1.5}$$

The time averaging is used in scenarios when the averaging is independent of t_0 and the flow is considered as steady. For unsteady flow conditions i.e. the flow variables change with the time, an ensemble averaging is used instead of the time-averaging.

Mean-flow equations

Averaging of incompressible Navier-Stokes equations leads to the following equations,

$$\frac{\partial \overline{u}_i}{\partial x_i} = 0 \tag{1.6}$$

$$\rho \frac{\partial \overline{u}_i}{\partial t} + \rho \frac{\partial}{\partial x_j}(\overline{u}_j \overline{u}_i) = -\frac{\partial \overline{P}}{\partial x_i} + \frac{\partial}{\partial x_j}(2\nu \overline{S}_{ij} - \rho \overline{u_i' u_j'}) \tag{1.7}$$

These equations are termed as Reynolds Averaged Navier-Stokes equations. They are similar to Navier-Stokes equations, however, new terms are introduced in the momentum equations due to the non-linearity. These terms account for the effect of momentum transfer by turbulent eddies and it can be termed as turbulent convective momentum flux.

Favre-Averaged mean flow equations

Reynolds averaging is inadequate for compressible flows as it leads to the presence of $\overline{\rho' u_j'}$ term whose closure form is difficult to be derived. The way to circumvent this issue is by decomposing flow variables using Favre-averaging (Eq. (1.8)).

$$\phi = \widetilde{\phi} + \phi'' \tag{1.8}$$

$$\widetilde{\phi}(x) = \frac{1}{\overline{\rho}} \lim_{T\to\infty} \frac{1}{T} \int_{t_0}^{t_0+T} \rho(x,\tau)\phi(x,\tau) d\tau \tag{1.9}$$

where ($''$) indicates the fluctuating component ($\phi - \widetilde{\phi}$). This averaging can also be expressed in the form of Reynolds-averaging as $\widetilde{\phi}\overline{\rho} = \overline{\rho\phi}$. The Favre-averaged equations are given as (Wilcox, 1994),

$$\frac{\partial \overline{\rho}}{\partial t} + \frac{\partial \overline{\rho}\widetilde{u}_i}{\partial x_i} = 0 \tag{1.10}$$

$$\frac{\partial \overline{\rho}\widetilde{u}_i}{\partial t} + \frac{\partial}{\partial x_j}(\overline{\rho}\widetilde{u}_j\widetilde{u}_i) = -\frac{\partial P}{\partial x_i} + \frac{\partial}{\partial x_j}(\overline{t}_{ij} + \tau_{ij}) \tag{1.11}$$

where $\overline{t}_{ij} = 2\mu\overline{S}_{ij} + \lambda\frac{\partial \overline{u}_k}{\partial x_k}\delta_{ij}$, $\overline{\rho}\tau_{ij} = -\overline{\rho u_i'' u_j''}$ and $P = \overline{\rho}R\widetilde{T}$. δ_{ij} is Kronecker delta function.

$$\frac{\partial \overline{\rho}E}{\partial t} + \frac{\partial}{\partial x_j}(\overline{\rho}\widetilde{u}_j H) = \frac{\partial}{\partial x_j}\Big(u_i(\overline{t}_{ij} + \tau_{ij})\Big) + \frac{\partial}{\partial x_j}\Big(- q_{l,j} - q_{t,j} + \overline{t_{ji}u_i''} - \overline{\rho u_j'' \frac{1}{2} u_i'' u_i''}\Big) \tag{1.12}$$

H and E are total enthalpy and total energy respectively. $q_{l,j}$ and $q_{t,j}$ are the laminar and turbulent heat flux vectors respectively. The magnitude of $\overline{t_{ji}u_i''}$ and $\overline{\rho u_j'' \frac{1}{2} u_i'' u_i''}$ indicates molecular diffusion and turbulence transport of kinetic energy respectively and can be ignored up to the supersonic flow regime. For convenience, Eqs. (1.10) - (1.12) are referred to as compressible RANS equations. In the further sections, the overbar and the tilde are removed from RANS equations.

Closure Problem

The solution of the incompressible Reynolds-averaged momentum equation requires the value of the turbulent stress tensor, while Reynolds averaging introduces six new variables for the turbulent stress tensor. Thus, there are 10 variables and only 4 equations to solve for it.

Derivation of additional equations for the stress tensor is as follows. (Wilcox, 1994) defined the Navier-Stokes operator ($N(u_i)$) as,

$$N(u_i) = \rho\frac{\partial u_i}{\partial t} + \rho\frac{\partial}{\partial x_j}(u_i u_j) + \frac{\partial P}{\partial x_i} - \frac{\partial}{\partial x_j}(2\nu S_{ij}) \tag{1.13}$$

$$\overline{u_i' N(u_j) + u_j' N(u_i)} = 0 \tag{1.14}$$

Following the procedure by Wilcox (1994), the transport equation for the turbulent stress tensor can be derived by using the transformation operation given in Eq. (1.14). This leads to the following equations,

$$\frac{\partial \tau_{ij}}{\partial t} + u_k\frac{\partial \tau_{ij}}{\partial x_k} = -\tau_{ik}\frac{\partial u_j}{\partial x_k} - \tau_{jk}\frac{\partial u_i}{\partial x_k} + \epsilon_{ij} - \Pi_{ij} + \frac{\partial}{\partial x_k}\left[\nu\frac{\partial \tau_{ij}}{\partial x_k} + C_{ijk}\right] \tag{1.15}$$

where $\Pi_{ij} = \overline{p'\left(\frac{\partial u_i'}{\partial x_j} + \frac{\partial u_j'}{\partial x_i}\right)}$, $\epsilon_{ij} = \overline{2\mu\frac{\partial u_i'}{\partial x_k}\frac{\partial u_j'}{\partial x_k}}$ and $C_{ijk} = \overline{\rho u_i' u_j' u_k'} + \overline{p' u_i'}\delta_{jk} + \overline{p' u_j'}\delta_{ik}$.

Eq. (1.15) is known as the Reynolds-stress equations. Even though the derivation leads to 6 additional equations, it introduces 22 additional unknown variables. Hence, deriving additional equations for the turbulence closure is futile. The non-linearity of Navier-Stokes equations leads to the deficit between the number of unknown variables and equations. This is termed as the closure problem.

Boussinesq Eddy-Viscosity hypothesis

The closure problem motivated the computation of the Reynolds stress tensor based on additional assumptions. Boussinesq hypothesis assumes that the convective turbulent momentum transport is similar to the molecular momentum transport. The molecular momentum transport leads to the shear stress in the flow and similarly the transport of momentum due to turbulence results in the turbulent shear stress. Using the hypothesis, the Reynolds stress tensor is expressed in terms of the local mean strain rate of the flow. This is known as the turbulent-viscosity hypothesis and is expressed as,

$$\tau_{ij} = -\rho\overline{u_i'' u_j''} = 2\mu_t\Big(S_{ij} - \frac{1}{3}\frac{\partial \widetilde{u}_k}{\partial x_k}\delta_{ij}\Big) - \frac{2}{3}\rho k\delta_{ij} \tag{1.16}$$

where μ_t is called turbulent viscosity. The problem is reduced to the modeling of μ_t. Boussinesq approximation assumes that the anisotropy Reynolds stress tensor ($\tau_{ij} + 2/3\rho k\delta_{ij}$) is aligned to the mean rate of strain. In highly swirling flows and flows with significant streamline curvature, the anisotropy increases and the assumption is violated. The present work focuses on the use of linear-eddy viscosity turbulence models, which are based on the Boussinesq approximation. The value of μ_t is determined from different turbulence models which are described in Chapter 2.

1.2 Background

Computational Fluid Dynamics has been increasingly used for the design and development process in several industries. The numerical resolution of Navier-Stokes equations is computationally expensive and industries often rely on the ensemble averaged solution of Navier-Stokes equations. This dimensional reduction of the problem is based on several assumptions. Accurate models must be devised to capture the relevant physics while maintaining reasonable computational costs. The computation of heat transfer is a requirement in several industries such as HVAC (Heating Ventilation and Air-Conditioning) design, electronic cooling, nuclear power plants and aerospace industries. In the aerospace industries, the need stems in the niche of several areas such as the design of the heat shield for space shuttles used during the hypersonic re-entry, the design of the lining material and the cooling system in gas turbines, the certification of aircraft in atmospheric icing conditions being just a few among the many applications.

Theoretically, no surface is perfectly smooth. Specialized manufacturing processes are used to produce surfaces such that the roughness is small enough not to cause any loss of aerodynamic performance. These surfaces are called as aerodynamically or hydraulically smooth surfaces. However, the issues lie in the fact that the surfaces in many applications evolve to become rough which complicates the computational modeling of flows over these surfaces. The surface during re-entry becomes rough due to the surface ablation and the wear at high Mach number. In gas turbines, the surface erosion and the deposition of fuel make the surfaces rough. During the ice accretion process on aircraft, the iced surfaces are also rough. In ice shape prediction and analysis simulations, the predicted ice shape and the resulting aerodynamic performance is sensitive to the roughness parameter input (Kontogiannis et al., 2018). The effect of roughness is fundamentally similar in all these applications i.e. it leads to an increase in the

heat transfer and friction drag.

1.3 Problem statement

Accurate simulation of flows over rough walls can be performed using different high fidelity approaches like DNS and wall-resolved LES. However, these approaches are too expensive for the industrial scenario. Industries require approaches with a lower computational cost and considerable accuracy. RANS solvers have been used for simulating flow in the industrial scenario for a smooth surface. The extension of RANS solvers for incorporating roughness effects is a very attractive solution. It involves an additional input known as the equivalent sand-grain roughness, which is used to quantify the effect of roughness on the increase in skin friction coefficient. RANS turbulence models often rely on the use of the assumption of Reynolds analogy for modeling heat transfer. A single roughness parameter is inadequate to model accurately the heat transfer over rough surfaces. This problem is severe for present RANS codes as it leads to inconsistency between the computed skin-friction coefficient and Stanton number over rough surfaces. This is because the Reynolds analogy fails in the presence of rough walls and it is not an accurate assumption for modeling flows as the physics of momentum and heat transfer scales differently in the presence of roughness. Therefore, robust RANS based approaches that accurately simulate both momentum and heat transfer for different roughness types is the need for present industrial CFD codes.

1.4 Objectives

The present work explores modern RANS approaches to improve the estimation of heat transfer over rough surfaces. The basic idea is to explore different strategies to remove the assumption of the Reynolds analogy and ensure consistency between the skin-friction coefficient and Stanton number. Both low and high (Wall functions) Reynolds number turbulence model approaches are compared for this purpose. The objectives of this study are as follows,

- Investigate different approaches to extend low-Reynolds number RANS turbulence models for accurate modeling of skin-friction and heat transfer over rough surfaces.
- Develop a robust state-of-the-art wall-function strategy capable of handling heat transfer on rough surfaces.

1.5 Plan of thesis

The thesis is structured to facilitate the understanding and the validation of the two approaches for simulating the effect of roughness on heat transfer. The thesis is divided into four chapters: Literature Review, Low-Reynolds Number Turbulence Model Approach, High-Reynolds Number Turbulence Model Approach and Conclusions.

Chapter 2 covers the literature review of the relevant topics required to develop a basic understanding of RANS turbulence modeling for smooth walls. Two approaches i.e. low and high-Reynolds number turbulence models are discussed. Experimental studies considering the physics of flow and heat transfer in the presence of roughness are also explored.

Chapter 3 discusses the low-Reynolds turbulence model approach to incorporate roughness effects. The theory behind the extensions, the numerical framework and the results validating the extensions are discussed. The improvement in the heat transfer results obtained using thermal correction by Aupoix is also analyzed.

Chapter 4 discusses the wall function or high-Reynolds number approach of modeling the effects of roughness. The theory behind wall functions, their implementation in the existing RANS code and extension for roughness effects are highlighted. The verification and validation of wall functions are also performed.

Chapter 5 concludes the discussion highlighting the advantages and disadvantages of the two approaches. Limitations of the proposed models and future directions to advance the research frontiers are mentioned.

CHAPTER 2 LITERATURE REVIEW

2.1 RANS turbulence models

The value of turbulent viscosity is calculated from several turbulence models such as Baldwin-Lomax, $k-\epsilon$, Spalart-Allmaras, $k-\omega$ SST, etc. As these turbulence models assume a linear relationship between Reynolds stress tensor and strain rate tensor, they are known as linear eddy-viscosity turbulence models. Our study is restricted to the latter two turbulence models, hence these two are discussed in some details.

2.1.1 Spalart-Allmaras (SA) turbulence model

The turbulence model proposed by Spalart and Allmaras (1992) has been widely used for aerospace applications. This model introduces the effect of turbulence by modeling μ_t based on the solution of the following equation,

$$\frac{\partial \tilde{\nu}}{\partial t} + u_j \frac{\partial \tilde{\nu}}{\partial x_j} = c_{b1}\tilde{S}\tilde{\nu} - c_{w1} f_w \left(\frac{\tilde{\nu}}{d}\right)^2 + \frac{1}{\sigma}\frac{\partial}{\partial x_k}\left[(\nu + \tilde{\nu})\frac{\partial \tilde{\nu}}{\partial x_k}\right] + \frac{c_{b2}}{\sigma}\frac{\partial \tilde{\nu}}{\partial x_k}\frac{\partial \tilde{\nu}}{\partial x_k} \tag{2.1}$$

Here, the closure coefficients used are as follows,

$$c_{b1} = 0.1355,\ c_{b2} = 0.622,\ c_{v1} = 7.2,\ \sigma = 2/3 \tag{2.2}$$

$$c_{w1} = \frac{c_{b1}}{\kappa^2} + \frac{1 + c_{b2}}{\sigma},\ c_{w2} = 0.3,\ c_{w3} = 2,\ \kappa = 0.41 \tag{2.3}$$

The other auxiliary relations are defined as follows,

$$f_{v1} = \frac{\chi^3}{\chi^3 + c_{v1}^3},\ f_{v2} = 1 - \frac{\chi}{\chi + \chi f_{v1}},\ f_w = \left[g\frac{1 + c_{w3}^6}{g^6 + c_{w3}^6}\right]^{1/6} \tag{2.4}$$

$$\chi = \frac{\tilde{\nu}}{\nu},\ g = r + c_{w2}(r^6 - r),\ r = \frac{\tilde{\nu}}{\tilde{S}\kappa^2 d^2} \tag{2.5}$$

$$\tilde{S} = S + \frac{\tilde{\nu}}{\kappa^2 d^2} f_{v2},\ S = \sqrt{2\Omega_{ij}\Omega_{ij}} \tag{2.6}$$

where $\Omega_{ij} = \frac{1}{2}(\partial U_i/\partial x_j - \partial U_i/\partial x_i)$ is the rotation tensor and d is the distance to the wall. Turbulent eddy viscosity is computed as,

$$\mu_t = \rho\tilde{\nu} f_{v1} \tag{2.7}$$

In these equations, $\tilde{\nu}$ is the variable introduced in the SA turbulence model. This variable is referred to as the Spalart-Allmaras (SA) variable in this thesis.

2.1.2 $k-\omega$ SST Turbulence model

The $k-\epsilon$ turbulence model (Launder and Spalding (1974), Chien (1982) and other variants) has been used for several industrial applications however the accuracy in the presence of walls is questionable. Wilcox (1988) formulated the $k-\omega$ turbulence model which proved to be more accurate in wall-bounded flows. Unfortunately, this model suffers from sensitivity to the free-stream turbulence value. This is not an issue in $k-\epsilon$ turbulence model. Keeping this in mind, Menter (1994) devised a turbulence model by expressing ϵ in terms of ω and adding a blending term to switch between the two turbulence models. This allows the model to follow the near-wall behavior of $k-\omega$ turbulence model and far-field behavior of $k-\epsilon$ turbulence model. He also added a limiter to restrict the evolution of turbulent viscosity near the edge of the boundary layer. It significantly improves the prediction in the presence of a pressure gradient. He named this model as the $k-\omega$ SST turbulence model ((Menter, 1994)). The turbulence model solves the following two equations to determine the value of the eddy viscosity.

$$\frac{\partial \rho k}{\partial t} + \frac{\partial \rho u_j k}{\partial x_j} = P - \beta^* \rho\omega k + \frac{\partial}{\partial x_j}\Big[(\mu + \sigma_k \mu_t)\frac{\partial k}{\partial x_j}\Big] \tag{2.8}$$

$$\frac{\partial \rho \omega}{\partial t} + \frac{\partial \rho u_j \omega}{\partial x_j} = \frac{\gamma}{\nu_t} P - \beta\rho\omega^2 + \frac{\partial}{\partial x_j}\Big[(\mu + \sigma_\omega \mu_t)\frac{\partial \omega}{\partial x_j}\Big] + 2(1-F_1)\frac{\rho\sigma_{\omega 2}}{\omega}\frac{\partial k}{\partial x_j}\frac{\partial \omega}{\partial x_j} \tag{2.9}$$

where

$$\tau_{ij} = \mu_t\Big(2S_{ij} - \frac{2}{3}\frac{\partial u_k}{\partial x_k}\delta_{ij}\Big) - \frac{2}{3}\rho k\delta_{ij}, \quad P = \tau_{ij}\frac{\partial u_i}{\partial x_j}, \quad S_{ij} = \frac{1}{2}\Big(\frac{\partial u_i}{\partial x_j} + \frac{\partial u_j}{\partial x_i}\Big) \tag{2.10}$$

The turbulent eddy viscosity is given as,

$$\mu_t = \frac{\rho a_1 k}{\max(a_1\omega, \Omega F_2)} \tag{2.11}$$

The constants ($\phi = \{\sigma_k,\ \sigma_\omega,\ \beta,\ \gamma\}$) in these equations are obtained by using a blending

function which suitably interpolates the corresponding value of constants in $k-\omega$ and $k-\epsilon$ models. These constants are expressed as,

$$\phi = F_1\phi_1 + (1-F_1)\phi_2 \tag{2.12}$$

where

$$F_1 = \tanh(\arg_1^4), \quad \arg_1 = \min\Big[\max\Big(\frac{\sqrt{k}}{\beta^*\omega d}, \frac{500\nu}{d^2\omega}\Big), \frac{4\rho\sigma_{\omega 2}k}{CD_{k\omega}d^2}\Big] \tag{2.13}$$

$$F_2 = \tanh(\arg_2^2), \quad \arg_2 = \max\Big(2\frac{\sqrt{k}}{\beta^*\omega d}, \frac{500\nu}{\omega d^2}\Big) \tag{2.14}$$

$$CD_{kw} = \max\Big(2\rho\sigma_{\omega 2}\frac{1}{\omega}\frac{\partial k}{\partial x_j}\frac{\partial \omega}{\partial x_j}, 10^{-20}\Big) \tag{2.15}$$

The value of constants are given as,

$$\gamma_1 = \frac{\beta_1}{\beta^*} - \frac{\sigma_{\omega 1}\kappa^2}{\sqrt{\beta^*}}, \quad \gamma_2 = \frac{\beta_2}{\beta^*} - \frac{\sigma_{\omega 2}\kappa^2}{\sqrt{\beta^*}}, \tag{2.16}$$

$$\sigma_{k1} = 0.85, \quad \sigma_{k2} = 1.0, \quad \beta_1 = 0.075, \quad \beta_2 = 0.0828, \quad \sigma_{\omega 1} = 0.50, \quad \sigma_{\omega 2} = 0.856 \tag{2.17}$$

$$\beta^* = 0.09, \quad \kappa = 0.41 \quad a_1 = 0.31 \tag{2.18}$$

The k and ω variables in the turbulence model are known as turbulent kinetic energy and specific dissipation respectively.

2.2 Modeling of thermal diffusivity

The mean flow energy equation (Eq. (1.12)) also contains unknown vector terms which account for the heat transfer through the turbulent eddies. The form of mean momentum and heat transfer equations are similar. It can be argued that momentum and scalar transport follows similar physics and the Boussinesq hypothesis can be extended to mean energy equation as well. Therefore, the turbulent convective heat transfer is written as,

$$q_{t,j} = \overline{\rho u_j'' h''} = -k_c\frac{\partial T}{\partial x_j} \tag{2.19}$$

where $k_c = \alpha_t \rho c_p$ and α_t is termed as the turbulent thermal diffusivity. With the temperature gradient vector available from the mean flow solution, the effect of turbulence can be determined by modeling α_t. Similar to the eddy viscosity, several thermal turbulence models are available for computing the turbulent thermal diffusivity. Comparison of these models was well summarized by Yoder (2016). He showed that the use of two-equations models does not significantly improve the performance and the algebraic models give the best combination of accuracy and computational cost. Most of the RANS solvers model the thermal diffusivity as follows,

$$\alpha_t = \frac{\nu_t}{Pr_t} \tag{2.20}$$

where Pr_t is called turbulent Prandtl number. The value of turbulent Prandtl number varies within the boundary layer reaching more than one in the viscous sublayer. A very plausible assumption is $Pr_t = 0.9$ which is the value in the logarithmic region. This assumption is termed as the Reynolds Analogy ($Pr_t \approx 1$) and gives good results for wall-bounded flows. It is used in most commercial and in-house CFD codes. The use of this assumption has been questioned in the presence of a pressure gradient, high free-stream turbulence and rough walls (Bons, 2005).

2.3 Near-wall behavior of turbulent flows

2.3.1 Non-dimensional variables

A scaling is introduced to generalize the behavior of various variables near the wall. The non-dimensional velocity, temperature and turbulence variables are as follows,

$$u^+ = \frac{u}{u_\tau},\ y^+ = \frac{y u_\tau}{\nu},\ T^+ = \frac{T}{T_\tau},$$
$$\tilde{\nu}^+ = \frac{\tilde{\nu}}{\nu},\ \nu_t^+ = \frac{\nu_t}{\nu},\ k^+ = \frac{k}{u_\tau^2},\ \omega^+ = \frac{\omega \nu}{u_\tau^2}$$

where u_τ ($= \sqrt{\tau_w/\rho}$) and T_τ ($= q_w/\rho u_\tau c_p$) are called friction velocity and friction temperature respectively.

2.3.2 Law of the wall

In the near-wall region for an attached flow, the magnitude of the stream-wise gradients for velocity is minimal in comparison to normal to the wall gradients. Taking that into account, for incompressible steady flows, the RANS momentum equation near the wall can be reduced to the form given in Eq. (2.21).

$$\frac{d}{dy}\left((\mu+\mu_t)\frac{du}{dy}\right)=\frac{dp}{dx} \tag{2.21}$$

Assuming a zero-pressure gradient, this equation further reduces to,

$$\frac{d}{dy}\left((\mu+\mu_t)\frac{du}{dy}\right)=0 \tag{2.22}$$

$$(\mu+\mu_t)\frac{du}{dy}=\tau_w \tag{2.23}$$

where τ_w is the shear stress at the wall. This equation can be expressed in terms of non-dimensional variables.

$$(1+\nu_t^+)\frac{du^+}{dy^+}=1 \tag{2.24}$$

This behavior is universal at sufficiently high Reynolds numbers and is depicted in Figure 2.1. An attached boundary layer is composed of two regions that are commonly called as the inner ($y < 0.2\delta$) and the outer region ($y > 0.2\delta$). For equilibrium flow conditions, the behavior of flow variables in the inner region can be considered independent to the outer region. This results in the universal behavior of the near wall region. Furthermore, the inner region can be further subdivided into 3 layers.

- Viscous sublayer ($y^+ < 5$): The viscosity dominates this layer and the turbulence effects are relatively weak.
- Buffer layer ($5 \leq y^+ < 30$): Both the viscous and turbulence momentum exchanges are of similar magnitude in this region.
- Logarithmic layer ($y^+ \geq 30$): The turbulence dominates this layer and the viscosity has a minute effect.

In the viscous sublayer, the effect of turbulence is negligible ($\nu_t^+ << 1$) and Eq. (2.24) reduces

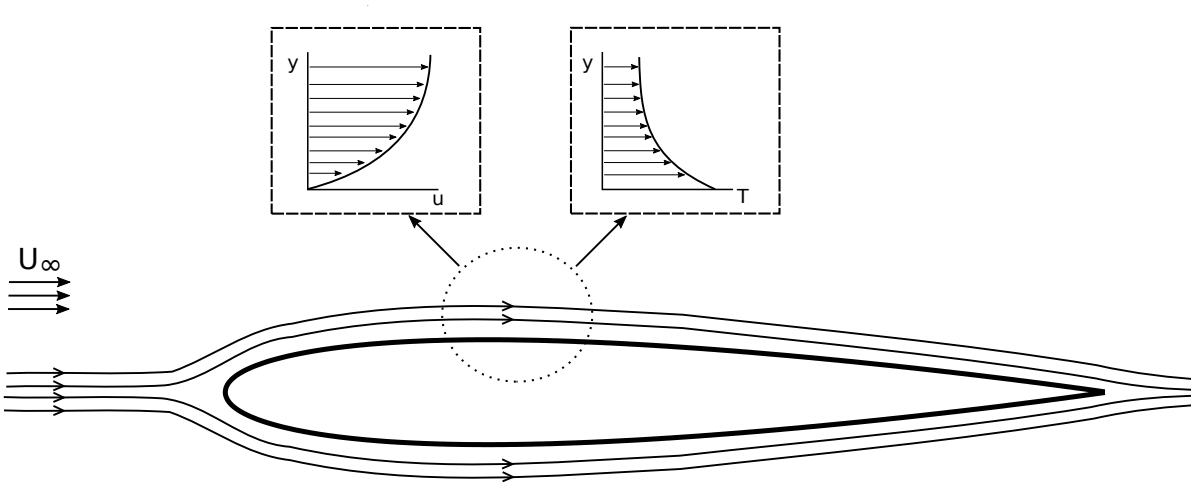

Figure 2.1 Velocity and temperature profiles in the boundary layer over an airfoil

to,

$$\frac{du^+}{dy^+} = 1 \tag{2.25}$$

For the logarithmic layer, the turbulence viscosity dominates ($\nu_t^+ >> 1$), simplifying Eq. (2.24) to the following form,

$$\frac{du^+}{dy^+} = \nu_t^+ \tag{2.26}$$

The variation of eddy viscosity in the logarithmic layer satisfies the relation $\nu_t^+ = \kappa y^+$, where, κ (≈ 0.41) is the Von-Karman constant. Integrating Eqs. 2.25 and 2.26 leads to the semi-analytic solution of velocity in the viscous sublayer and the logarithmic layer.

$$u^+ = \begin{cases} y^+, & y^+ < 5 \\ \frac{1}{\kappa}\ln(y^+) + C & y^+ > 30 \end{cases} \tag{2.27}$$

where $C = 5.0 - 5.5$ has been experimentally determined. The exact value of these constants have been debated and can vary between different turbulence models. The velocity profile is commonly reflected in the semi-log plot as shown in Figure 2.2. Note that this is the velocity profile for the Spalart-Allmaras turbulence model. The profile for other turbulence models might be slightly different especially in the buffer layer.

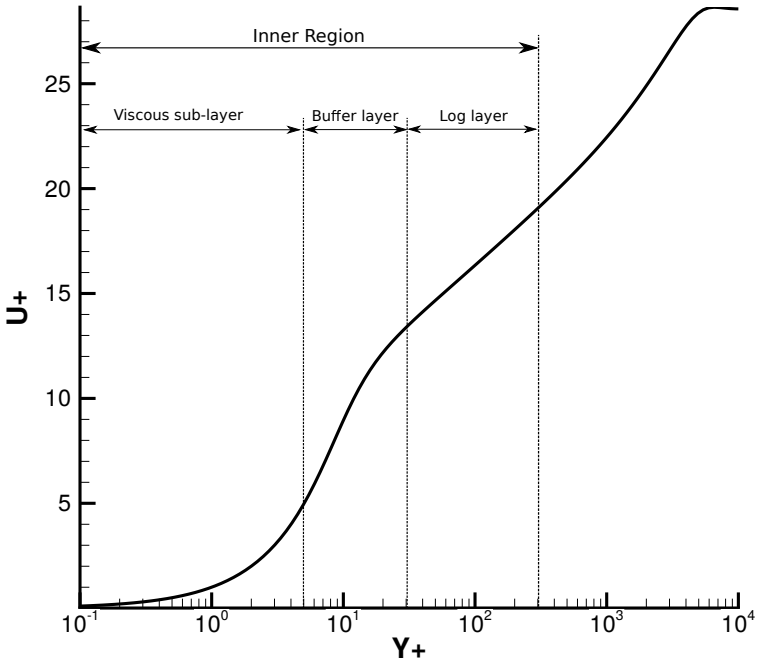

Figure 2.2 Different layers in inner region of boundary layer

Based on similar assumptions as those used for derivation of the velocity wall function, the temperature wall function can also be derived. The energy equation reduces to the following form,

$$\frac{d}{dy}\Big[\Big(\frac{\mu}{Pr}+\frac{\mu_t}{Pr_t}\Big)\frac{dT}{dy}\Big]=0 \tag{2.28}$$

Integrating this equation and converting it into non-dimensional quantities, the following form is obtained,

$$\Big(\frac{1}{Pr}+\frac{\nu_t^+}{Pr_t}\Big)\frac{dT^+}{dy^+}=1 \tag{2.29}$$

From Eq. (2.29), it is observed that for a low Prandtl number fluid (i.e. liquid metals), the first term on the left-hand side cannot be neglected in the inner region. However, for air ($Pr=0.71$), the integration of this equation leads to the following form,

$$T^+=\begin{cases} Pry^+, & y^+<5 \\ \frac{Pr_t}{\kappa_T}\ln(y^+)+C_T & y^+>30 \end{cases} \tag{2.30}$$

It has been found that the value of k_T and C_T can be slightly different from its velocity counterpart. $k_T = 0.48$ and $C_T = 3.9$ is found in Kader and Yaglom (1972). In the logarithmic region, Eqs. (2.27) and (2.30) are commonly known as the law of the wall for velocity and temperature respectively.

2.4 Near-wall treatment approaches

There are two near-wall treatment approaches that are commonly used with both Spalart-Allmaras and $k-\omega$ SST turbulence models.

2.4.1 Low-Re turbulence model or Wall Integration approach

At a high local Reynolds number, mean flow gradients are steep near the wall. For accurate modeling, the RANS turbulence models can be solved to the wall to resolve the gradients. This approach is termed as the Low-Reynolds (Low-Re) turbulence model approach. The requirement of a fine mesh leading to a high computational cost is a major drawback of this approach. The boundary conditions for the turbulence variables for smooth walls is prescribed as follows.

Spalart-Allmaras turbulence model

The boundary condition for the modified eddy viscosity in the case of smooth walls is given as,

$$\tilde{\nu}_w = 0 \tag{2.31}$$

$k-\omega$ SST turbulence model

The boundary condition for the equation of k on a smooth wall is quite straightforward as the turbulent kinetic energy goes to zero at the wall. However, ω (defined as ϵ/k) exhibits a singular behavior at the wall. Boundary condition for the k and ω by Menter (1994) is often used.

$$k_w = 0,\ \omega_w = \frac{60\nu}{\beta^* y^2} \tag{2.32}$$

where y is the wall distance.

2.4.2 High-Re turbulence model or Wall Function approach

The requirement of using a fine mesh to resolve the gradients in the viscous sublayer leads to high demand for computational power. A way to overcome this issue is to use the semi-analytical solution near the wall (i.e. law of the wall) that is derived in Section 2.3.2. These velocity and temperature profiles are commonly called wall functions.

Velocity wall functions

Several wall functions exist in the literature. The simplest form (Eq. (2.27)) is commonly known as the standard wall function. The interactions between viscosity and turbulent scales make it harder to analytically determine the behavior in the buffer region. Nevertheless, several researchers have come up with wall-laws based on experimental results and interpolation of the viscous sublayer and the logarithmic region profiles. These wall functions are often called universal wall functions, as they model the behavior in the entire inner region.

Spalding (1961)

$$y^+ = u^+ + e^{-\kappa B}(1 - e^{\kappa u^+} - \frac{(\kappa u^+)}{1!} - \frac{(\kappa u^+)^2}{2!} - \frac{(\kappa u^+)^3}{3!} - ..) \tag{2.33}$$

Reichardt (1951)

$$u^+ = \frac{\ln(1+\kappa y^+)}{\kappa} + 7.8\left(1 - e^{-\frac{y^+}{11}} - \frac{y^+}{11}e^{-\frac{y^+}{3}}\right) \tag{2.34}$$

Knopp et al. (2006)

For Spalart-Allmaras:

$$F_{SA,a} = (1-\phi_{SA})F_{Sp,5} + \phi_{SA}F_{Rei,m}, \quad \phi_{SA} = \tanh\left[\left(\frac{y^+}{24}\right)^3\right] \tag{2.35}$$

For k-ω SST:

$$F_{kw,a} = (1-\phi_{kw})F_{Sp,3} + \phi_{kw}F_{Rei,m}, \quad \phi_{kw} = \tanh\left[\left(\frac{y^+}{50}\right)^2\right] \tag{2.36}$$

$$F_{Rei,m} = (1-\phi_{b1})F_{Rei} + \phi_{b1}F_{log} \tag{2.37}$$

where $\phi_{b1} = \tanh[(y^+/27)^4]$.

Here, $F_{Sp,5}$ and $F_{Sp,3}$ implies the Spalding equation truncated to 5 and 3 terms respectively. F_{Rei} and F_{log} are the Reichardt and Standard-log profiles respectively.

Allmaras et al. (2012)

$$u^+ = \bar{B} + c_1 \ln((y^+ + a_1)^2 + b_1^2) \\ - c_2 \ln((y^+ + a_2)^2 + b_2^2) - c_3 \text{atan2}(b_1, y^+ + a_1) - c_4 \text{atan2}(b_2, y^+ + a_2) \quad (2.38)$$

The value of the constants can be found in the respective papers. The latter one is based on the near wall analytic solution of the Spalart-Allmaras turbulence model.

Other wall functions

There have been several attempts to generalize wall functions by removing the underlying assumptions. This leads to minimal differences in the result of various wall functions for simple flows like Couette flow. Their performance improves in specific flow situations like the presence of a pressure gradient or flows at a high Mach number. Craft et al. (2002) proposed a wall function to simulate buoyant flows by analytically integrating a more general form of Eq. (2.24) that includes the convective transfer of momentum and pressure gradient. As a result, it is called Analytical Wall Function (AWF). The analytical integration is made possible by assuming a relation between turbulent viscosity and wall normal distance. Gant (2002) proposed a wall function formed by numerical integration of the parabolized transport equation on a 1-D sub-grid. The solution of the sub-grid is interpolated to the first wall cell. Popovac and Hanjalic (2007) remarked that these two wall functions involved complex expressions and were hard to incorporate into a general purpose commercial CFD code. He followed a similar strategy as Craft et al. (2002) but used a simpler expression for the turbulent viscosity. This simplification resulted in a wall function with a similar form as the log law. The form is given in Eq. (2.39).

$$u^+ = \frac{1}{\psi\kappa} \ln(y^+) + C \quad (2.39)$$

where ψ introduces the effect of non-equilibrium flow conditions. For equilibrium flows, the value of ψ is 1 and Eq. (2.39) reduces to standard log-law. This wall function was named as the generalized wall function. He further combined the generalized wall function with the blending function proposed by Kader (1981) to extend the validity over the entire inner region. Kalitzin et al. (2005) proposed a wall function based on the look-up table which was constructed from a well-resolved Couette flow simulation. The use of non-dimensional values of velocity, temperature and turbulence variable profiles from the look-up table ensured that

the wall function is consistent with the outer flow solution. The idea of the turbulent model consistent wall functions was emphasized by Knopp et al. (2006) and they showed that the reduction of this inconsistency leads to reduced grid dependence.

Temperature wall functions

The temperature profile derived in Eq. (2.30) is referred to as the standard temperature wall function. Like the velocity counterpart, its application in the buffer region is limited because of complex non-linear interactions of the viscous and turbulence scales. Nevertheless, several universal temperature wall functions also exist. These log-law based wall functions account for the entire inner region, and are as follows,

Kader (1981)

$$\theta^+ = Pry^+e^{-\tau} + 2.12\ln\Big[(1+y^+) + \beta(Pr)\Big]e^{-\frac{1}{\tau}} \tag{2.40}$$

where,

$$\tau = \frac{10^{-2}(Pry^+)^4}{1+5Pr^3y^+}, \quad \beta = (3.85Pr^{1/3} - 1.3)^2 + 2.12\ln Pr \tag{2.41}$$

Jayatillaka (1969)

$$T^+ = Pr_t(u^+ + P_f) \tag{2.42}$$

where P_f is given as,

$$P_f = 0.24\Big[\Big(\frac{Pr}{Pr_t}\Big)^{3/4} - 1\Big]\Big[1 + 0.28\exp\Big(-0.007\frac{Pr_t}{Pr}\Big)\Big] \tag{2.43}$$

Arpaci and Larsen (1984)

$$T^+ = \begin{cases} Pry^+ & y^+ < y_1^+ \\ a_2 - \frac{Pr_t}{2a_1(y^+)^2} & y_1^+ \le y^+ \le y_2^+ \\ \frac{Pr_t}{\kappa}\ln(y^+) + \beta & y_2^+ \le y^+ \end{cases} \tag{2.44}$$

where,

$$y_1^+ = \frac{10}{Pr^{2/3}}, \quad y_2^+ = \left(\frac{\kappa}{a_1}\right)^{1/2}, \quad a_1 = 10^{-3} Pr_t, \tag{2.45}$$

$$a_2 = 15 Pr^{2/3}, \quad \beta = a_2 - \frac{Pr_t}{2\kappa}\left[1 + \ln\left(\frac{\kappa}{a_1}\right)\right] \tag{2.46}$$

The wall functions by Craft et al. (2002) and Popovac and Hanjalic (2007) also account for the heat transfer. The look-up table approach can also be used for isothermal walls by precomputing and storing variation of T^+ with y^+. These were also extended to incorporate the effect of a pressure gradient by Lacombe et al. (2019).

2.5 Roughness

Roughness can occur naturally in the form of deposited ice on an airfoil or as a result of combustion deposits on turbine blades. Coating processes such as painting and galvanizing introduce roughness in pipes which initiated several studies for improving the understanding of pressure and heat loss through pipes. These studies were later extended to other canonical cases such as channel flows and flat plates.

Roughness can be classified broadly into d-type and k-type roughness (Perry et al., 1969). The former type comprises grooves in the smooth surface, whereas the latter consists of protrusions on the smooth surface. The roughness function (Δu^+) which quantifies the effect of roughness is different for these two types. The work in this thesis is concerned with the k-type roughness and further discussion on roughness is restricted to this type.

2.5.1 Effect on momentum transfer

Rough walls lead to the additional form drag from individual roughness elements that add to viscous shearing stress. The form drag can be a significant component of the total shearing drag force on the surface especially in the presence of separation of flow from individual roughness elements (Rotta, 1962). The experiments by Nikuradse (1933) on sand roughened pipes were the first well-detailed study on the effect of roughness. He showed that roughness leads to the translation of the logarithmic region in the profile as shown in Figure 2.3. The velocity profile can be expressed as follows,

$$u^+ = \frac{1}{\kappa}\ln(y^+) + C - \Delta u^+ \tag{2.47}$$

where Δu^+ is called the roughness function which depends on the height of the roughness

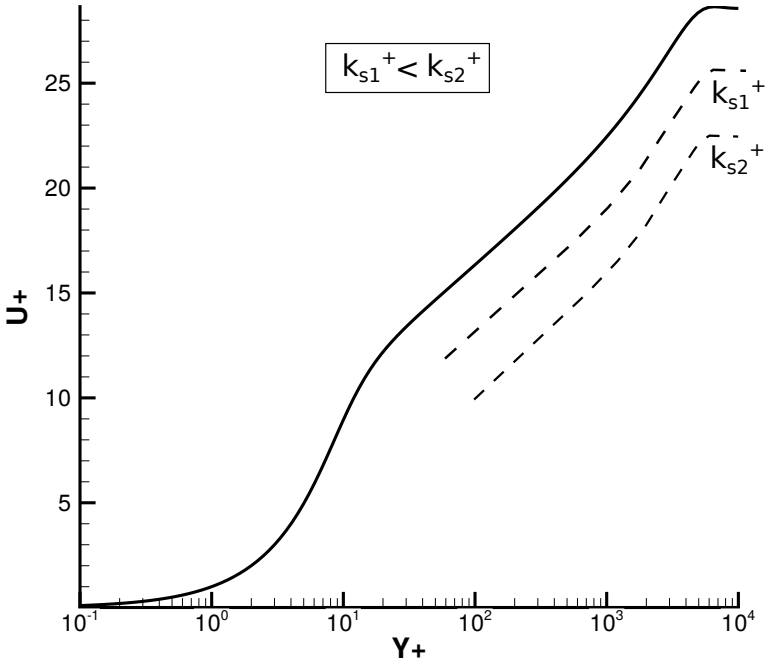

Figure 2.3 Shift of velocity profile due to roughness

elements. He further classified the effect of roughness on the basis of the non-dimensional roughness height.

Schlichting (1936) suggested that a single parameter such as the roughness height (denoted by h) is not sufficient to generalize the effect of different roughness elements. He highlighted the role played by roughness spacings in determining the roughness effect and pointed out that Nikuradse's experiments comprised of the roughness at constant (near the maximum) density. He coined the term equivalent sand-grain roughness (k_s) which is defined as the size of sand grain roughness that leads to the same shift of velocity profile as the investigated roughness. The work also encompassed the experimental extraction of α ($= h/k_s$) for different roughness element types and spacings.

Several researchers have derived expressions for a roughness scaling that relates the roughness parameters to the equivalent sand-grain roughness. Bettermann (1965) derived the roughness function for the fully rough surface as a function of roughness spacing parameter. Dvorak (1969) extended it for other roughness types and derived an expression to use it for cases with a pressure gradient. Dirling (1973) also considered the inclination of the roughness elements and derived the following expression.

$$\lambda = \frac{D}{k}\left(\frac{A_P}{A_S}\right)^{-\frac{4}{3}} \tag{2.48}$$

$$\frac{k_s}{k} = \begin{cases} 0.0164\lambda^{3.78}, \lambda < 4.93 \\ 139\lambda^{-1.9}, \lambda > 4.93 \end{cases} \tag{2.49}$$

where k is the mean roughness height, A_P is the projection of roughness element area along the normal to the flow and A_S is the wetted area of the roughness element along the flow direction. Waigh and Kind (1998) remarked that the inability of λ to distinguish between the roughness regimes at $\lambda \approx 5$. They proposed a different definition of λ as follows,

$$\Lambda = \frac{\text{Total volume over surface}}{\text{Effective volume of roughness elements}} = \lambda\frac{k}{s_m} \tag{2.50}$$

where k/s_m is the streamwise aspect ratio. They further classified roughness based on the Λ as dense ($\Lambda < 6$) and sparse ($\Lambda > 6$).

Flack and Schultz (2010) reviewed several other roughness scalings available in the literature. They highlighted the weakness of these scalings in case of the natural occurring roughness which is non-uniform in both height and spacing. They proposed a scaling based on rms roughness height and the skewness of the probability distribution function of the surface elevation. In the present thesis, most of the validation cases comprise of a regular roughness distribution (hence referred to as academic roughness cases). The k_s highlighted by the authors presenting the validation cases is used for an effective comparison.

The effect of the roughness on the skin-friction coefficient can be classified into the following categories on the basis of k_s (Nikuradse, 1933),

- Hydraulically smooth ($k_s^+ < 5$): The roughness has no effect on the skin friction and the surfaces can be assumed to be smooth. As the roughness elements lie within the viscous sublayer, the viscosity damps the instability induced by them.
  The limits of the hydraulically smooth flow are dependent on the roughness parameters. This is important to be identified as it can interfere with the experimentation for smooth walls. At high Reynolds number, the value of k_s^+ can exceed the critical roughness height. Bradshaw (2000) discusses on the limit of critical Reynolds number which marks the onset of the effect of roughness.

- Transitionally rough ($5 \leq k_s^+ \leq 70$): The thickness of the viscous sublayer decreases and the skin-friction coefficient increases with increasing value of k_s^+.

The effect of roughness in the transitionally rough regime has been debated as it is sensitive to the shape, size and the distribution of the roughness. The experimental data from Nikuradse (1933) showed an inflection point in the transitionally rough regime. However, Colebrook and White (1937) argued that data from Nikuradse was not representative of the common industrial roughness. They studied different roughness distribution patterns and highlighted that the variation of the skin friction coefficient in the transitionally rough regime is governed by the non-uniformness of roughness distribution. The onset of the regime is governed by the larger roughness and the completeness of the smooth to fully rough transition is determined by the smaller roughness. They concluded that a gradual transition is the characteristic of a non-uniform roughness distribution and pertains to industrial pipes. The most commonly used Moody Chart (Moody, 1944) is based on the experimental results by Colebrook. Recent experimental results on rough surfaces performed in the Superpipe showed that the industrial roughness follows the rough profile by Nikuradse in the transitionally rough regime (Allen et al., 2007).

- Fully rough ($k_s^+ > 70$): The skin-friction coefficient is independent of viscous forces as the viscous sublayer is completely destroyed. The skin friction coefficient depends on the k/R where R is the radius of the pipe which is constant. Therefore, the skin-friction becomes independent of the Reynolds number of the flow. For flat plate, the skin friction depends on k/δ where δ is the thickness of the boundary layer which is increasing downstream. This is the fundamental difference between the fully rough regime in pipe flow and a flat plate case.

  The interesting thing to note is that even though the effect of roughness on friction drag shows different behaviors at lower roughness heights, the behavior in the fully rough regime is well-defined. The experimental results from Nikuradse (1933) and Colebrook and White (1937) are proximate in this regime. The well-defined behavior has motivated several researchers to model the effect of the fully rough surface.

2.5.2 Effect on heat transfer

The physics of momentum and heat transfer in the presence of roughness is not similar. Therefore, the Reynolds analogy assumption does not hold for rough surfaces. For a k-type roughness, the increase in roughness height increases the skin friction coefficient. However, the increase in Stanton number is not proportional to the increase in the skin friction coefficient. In most situations, the increase in Stanton number is less than the increase in skin friction coefficient.

Nunner (1956) derived a semi-empirical model based on his experimentation of pipes with threads as roughness elements. This can be considered as a case of 2-D roughness and consists of a unique relationship between the heat transfer coefficient and skin friction coefficient. Dipprey and Sabersky (1963) remarked that the existence of a unique relationship is fundamentally wrong and it should depend on the type of roughness. Taking this into account and with the idea of extending Nikuradse's sand roughened pipe experiments for heat transfer, Dipprey and Sabersky (1963) conducted detailed experiments. They selected similar close-packed sand grain roughness, however, they restricted their study to fully rough regime. They observed that in the fully rough regime, unlike the skin friction coefficient, the heat transfer coefficient decreases monotonically with the Reynolds number. This also indicates different physics of heat and momentum transfer in the presence of roughness. According to them, cavity Stanton number accounts for the heat transfer through the conduction sublayer, which unlike viscous sublayer, exists even for the fully rough regime. Next to the conduction sublayer in roughness cavities, there exist cavity vortices which leads to convective transfer of heat away from the conduction sublayer. Outside the cavity, the Reynolds analogy is assumed to be valid. Accounting for the presence of a vortex in roughness cavities or so-called cavity vortex hypothesis, they derived a semi-analytic equation for the cavity Stanton number which accounts for effects of 3-D roughness elements on heat transfer. One of the most important observations from their experimentation is that a certain combination of Reynolds number and Prandtl number leads to no increase in Stanton number with the increase in k_s, even though skin friction coefficient increases.

Owen and Thomson (1963) performed an independent study on this problem. They reported that the presence of a conduction sublayer indicates that the heat transfer through the wall is always limited by conduction even when the flow through the roughness elements is separated. This leads to different physics of heat and momentum transfer in the presence of rough walls. Additionally, they associated the scouring action of the horseshoe eddies formed as a result of 3-D roughness elements to the convective mechanism of heat transfer in the presence of roughness. According to them, the model developed by Dipprey and Sabersky (1963) assumes a 2-D cavity flow and the one by them is based on 3-D cavity flow replicating the actual physics to a greater extent for 3-D roughness elements.

2.6 Modeling of heat transfer over rough surfaces

The previous section discusses the effect of roughness on the skin friction coefficient and Stanton number. These effects can be simulated accurately by performing DNS as well as wall-resolved LES simulations. It involves appropriate meshing of the roughness elements.

These methods are only used for fundamental research in understanding the dynamics of turbulent structures in the presence of roughness elements (Jiménez, 2004). As a research tool, it is very useful and can be used for improving the correlations for roughness effects over randomly distributed rough surfaces. These simulations involve a huge computational overhead and are not practical for industrial flows especially at a high Reynolds number.

Another approach to model roughness is to use Discrete Element Method (DEM). DEM has been used for modeling of multiphase flows. As Reynolds analogy does not hold for rough surface, DEM can be used to treat the momentum and the heat flux independently. The standard form for DEM for application to rough flows was developed for academic roughness elements (Coleman et al. (1983), Taylor et al. (1985)) and later extended to randomly distributed rough surfaces by McClain et al. (2004). This method incorporates the effect of roughness by introducing modifications in the RANS equations. These modifications are mostly in the form of source terms that replicate the added momentum and heat transfer in the presence of roughness elements. This method is not used in most of the industrial codes because it involves significant modifications to existing RANS solver.

Present industrial scenario enforces the use of RANS turbulence models to incorporate roughness effects. These models do not require any modifications if the mesh conforms well with the roughness geometry. However, the high computational cost and issues with mesh generation prohibit it. Another way to use RANS turbulence models in the presence of roughness is by introducing modifications to turbulence models based on the equivalent sand-grain roughness and replicate the shift in the velocity and temperature profile. The increased momentum and heat transfer are determined by accurately modeling the value of turbulent viscosity at the wall. It enables the use of a mesh similar to the one used for smooth walls simulations, thereby, not significantly affecting the computational cost. This approach is well suited for the present problem statement and extending the in-house CFD solver for roughness effects. There are two ways to extend turbulence models for roughness: 1) Wall Integration/ Low-Reynolds number turbulence model, 2) Wall Function/ High-Reynolds number turbulence model. These methods are discussed individually in the next two chapters. It is well-known that the high Reynolds number turbulence model approach has a higher convergence rate than the low Reynolds number counterpart (Carlson et al., 2015), however, the present study does not compare the convergence rate of the two approaches.

CHAPTER 3 LOW-RE TURBULENCE MODEL APPROACH

The low-Reynolds (Low-Re) turbulence model approach requires the use of a fine mesh. The RANS turbulence models assume the proportionality between the transport of turbulent convective momentum and the mean rate of strain. Therefore, the mesh is required to be fine enough for accurately computing the near-wall gradients. This chapter is oriented towards presenting the methodology and validating results for roughness extensions of the low-Re turbulence model approach. Firstly, the numerical framework for simulations is discussed. Then, different roughness extensions for two turbulence models are mentioned and the correction term to overcome the Reynolds analogy assumption for rough walls is discussed. Roughness extensions are first validated for friction drag predictions. Then, the validation of the thermal correction by comparison with heat transfer measurements is carried out. The effect of roughness on the friction drag is assessed by comparing with a semi-empirical relation as it allows several values of k_s to be tested. Results are then validated with experiments containing different roughness distributions over a flat plate. For the validation of the thermal correction, the comparison with friction drag and heat transfer measurements for two experimental cases is made.

3.1 Numerical framework

The study uses NSCODE which is a finite-volume multi-block structured compressible RANS solver. The details about the solver can be found in Pigeon et al. (2014). The RANS equations are discretized with the central scheme in space with scalar (Jameson et al., 1981) and matrix dissipation schemes (Swanson and Turkel, 1997). The simulations in the thesis are performed with the latter. For the present computations, 3 levels of multigrid (W-cycle), residual smoothing and 5 stage Runge-Kutta is used as the pseudo-temporal scheme. Meshes are generated by an in-house package named NSGRID (Hasanzadeh et al., 2016). Spalart-Allmaras and $k-\omega$ SST turbulence models are available in NSCODE. Spalart-Allmaras turbulence model was already extended for roughness effects and has been used for ice shape prediction using the in-house ice-shape prediction code called NSCODE-ICE (Bourgault-Cote and Laurendeau, 2015). The Stanton number in NSCODE is computed as follows,

$$St = \frac{q_w}{\rho u c_p (T_w - T_{ref})} \tag{3.1}$$

where T_w is the wall temperature and T_{ref} is the reference temperature. T_{ref} depends on the

flow conditions and choice of the experimental researchers while taking heat transfer measurements. It is often taken as T_{rec} (recovery temperature or adiabatic wall temperature) or T_∞ (free-stream temperature). St definitions obtained using these temperatures are referred to as St-def1 and St-def2 respectively. St-def1 is commonly used in aerodynamic applications and Lavoie (2017) points out that St-def2 is only valid in situations involving negligible viscous dissipation. He also mentions that the St-def1 resembles more closely with the heat transfer coefficient computation method by Montreuil et al. (2009) which uses two RANS computations. Therefore, this definition is used for most of the cases, unless the comparison is made to the experimental results obtained using other definition.

3.2 Extensions of turbulence models for roughness effects

The behavior of the flow in the inner region in the presence of roughness is marked by the downward shift of the logarithmic region. Townsend (1976) indicated that the nature of roughness has relatively less importance at large distances from the wall. Therefore, the behavior of the flow in the outer region is similar to the smooth wall and is solely affected by the change in the shear stress at the wall. Townsend's hypothesis can be written in an equation form as follows (Aupoix, 2007),

$$\Delta u^+ = u^+_{e,s} - u^+_{e,r} \tag{3.2}$$

where $u^+_{e,s} = \sqrt{2/C_{f,s}}$ and $u^+_{e,r} = \sqrt{2/C_{f,r}}$. The subscript 'e' indicates the edge of boundary layer. Eq. (3.2) indicates the skin-friction coefficient over the rough surface, and it is determined from the shift of the logarithmic region. This translation of the profile can be reproduced by introducing a shift in the wall (y_0, given by Eq. (3.3)). The virtual shift on the wall is based on the roughness height as suggested by Rotta (1962).

$$\Delta u^+ = u^+_s(y^+_0) \tag{3.3}$$

$$\frac{du^+_r}{dy^+}(y^+) = \frac{du^+_s}{dy^+}(y^+ + y^+_0) \tag{3.4}$$

Eq. (3.4) is used to express the connection between smooth and rough wall solutions. Considering Eq. (2.24), the effect of roughness is substituted to the shift of the profile of turbulent viscosity which is given by Eq. (3.5).

$$\mu_{t,r}(y^+) = \mu_{t,s}(y^+ + y^+_0) \tag{3.5}$$

Simulation of flow over rough surfaces requires the modification to the turbulence model equations, especially the boundary conditions are changed to replicate the turbulent viscosity profile given by Eq. (3.5). This is described for the Spalart-Allmaras and $k-\omega$ SST turbulence model as follows.

3.2.1 Spalart-Allmaras turbulence model

Aupoix and Spalart (2003) suggested two methods for incorporating the effect of roughness called BOEING and ONERA method. The fundamental difference between these two methods is that the ONERA method enforces a non-zero Dirichlet boundary condition for modified eddy viscosity at the wall whereas the BOEING method enforces a Neumann boundary condition. Convergence issues while using the ONERA method for airfoils was reported by Medida et al. (2014). Aupoix and Spalart (2003) showed that the difference in results between BOEING and ONERA corrections are minimal. Therefore, the ONERA correction is not further explored and the BOEING correction is discussed. The BOEING correction involves the shift of the wall given as,

$$d = y + y_0 \tag{3.6}$$

where d is the modified wall distance, y is the physical wall distance and $y_0 (= 0.03k_s)$ is the shift of the wall distance introduced due to roughness. This shift can be derived using Eq. (3.3) and the roughness function by Nikuradse (1933) while considering $\kappa = 0.41$. The damping function in the turbulence model is also modified (Eq. (3.7)) to ensure that the roughness function is also accurate in the transitionally rough regime.

$$\chi = \frac{\tilde{\nu}}{\nu} + c_{R1}\frac{k_s}{d} \tag{3.7}$$

Here, $c_{R1} = 0.5$. Neumann boundary condition is imposed and is given by,

$$\frac{\partial \tilde{\nu}}{\partial n} = \frac{\tilde{\nu}}{d} \tag{3.8}$$

where n is normal to the wall co-ordinate direction.

3.2.2 $k-\omega$ SST turbulence model

Several roughness extensions for $k-\omega$ SST turbulence model have been suggested over the years. One of the first suggestion was by Wilcox (1988) for $k-\omega$ turbulence model. As this

turbulence model does not involve a damping function, only a change of boundary conditions for turbulence variables is sufficient. The boundary condition for ω is modified as follows,

$$\omega = \frac{u_\tau^2}{\nu} S_R \tag{3.9}$$

$$S_R = \begin{cases} \left(\frac{50}{k_s^+}\right)^2 & , k_s^+ < 25 \\ \frac{100}{k_s^+} & , k_s^+ > 25 \end{cases} \tag{3.10}$$

The value of S_R was later revised in Wilcox (2008) to improve the estimation at low values of k_s^+. The roughness extension when applied to $k-\omega$ SST turbulence model leads to an underestimation of skin friction coefficient at higher values of k_s^+. Hellsten et al. (1997) reported that this behavior was the result of the activation of SST limiter. They suggested the following modification of the limiter to overcome this issue,

$$\mu_t = \frac{a_1 \rho k}{\max(a_1 \omega, |\Omega| F_2 F_3)} \tag{3.11}$$

$$F_3 = 1 - \tanh\left[\left(\frac{150\nu}{\omega d^2}\right)^4\right] \tag{3.12}$$

This modification delays the activation of the limiter. However, it is prone to numerical stability issues at higher values of k_s^+ (Knopp et al., 2009). Knopp et al. (2009) suggested a different correction that involves the modification of boundary conditions for both k and ω based on the approach devised by Aupoix (2007).

$$\begin{gathered} k_w = \phi_{r1} k_{rough}, \quad k_{rough} = \frac{u_\tau^2}{\beta_k^{1/2}} \\ \omega_w = \min\left(\frac{u_\tau}{\beta_k^{1/2} \kappa \tilde{d_0}}, \frac{60\nu}{\beta_\omega d_1}\right), \quad \tilde{d_0} = \phi_{r2} 0.03 k_r \\ \phi_{r1} = \min\left(1, \frac{k_r^+}{90}\right), \quad \phi_{r2} = \min\left[1, \left(\frac{k_r^+}{30}\right)^{2/3}\right] \min\left[1, \left(\frac{k_r^+}{45}\right)^{1/4}\right] \min\left[1, \left(\frac{k_r^+}{60}\right)^{1/4}\right] \end{gathered} \tag{3.13}$$

Note that β_k is the same as β^* in the turbulence model formulation. Aupoix (2014) remarked that the roughness extension by Knopp does not give good predictions in the transitionally rough regime. Overcoming this shortcoming, he suggested two corrections based on roughness functions by Nikuradse (1933) (Eq. (3.14)) and by Grigson (1992) that is based on data by

Colebrook and White (1937) (Eq. (3.15)).

$$k_w^+ = \max(0, k_0^+), \quad k_0^+ = \frac{1}{\sqrt{\beta^*}}\tanh\left[\left(\frac{\ln(k_s^+/30)}{\ln 8} + 0.5\Big[1 - \tanh\frac{k_s^+}{100}\Big]\tanh\Big(\frac{k_s^+}{75}\Big)\right)\right]$$
$$\omega_w^+ = \frac{400,000}{k_s^{+4}}\Big(\tanh\frac{10,000}{3k_s^{+3}}\Big)^{-1} + \frac{70}{k_s^+}\Big[1 - \exp\Big(-\frac{k_s^+}{300}\Big)\Big] \tag{3.14}$$

$$k_w^+ = \max(0, k_0^+), \quad k_0^+ = \frac{1}{\sqrt{\beta^*}}\tanh\left[\left(\frac{\ln(k_s^+/30)}{\ln 10} + 1 - \tanh\frac{k_s^+}{125}\right)\tanh\Big(\frac{k_s^+}{125}\Big)\right]$$
$$\omega_w^+ = \frac{300}{k_s^{+2}}\Big(\tanh\frac{15}{4k_s^+}\Big)^{-1} + \frac{191}{k_s^+}\Big[1 - \exp\Big(-\frac{k_s^+}{250}\Big)\Big] \tag{3.15}$$

The latter three boundary conditions are compared in Figure 3.1.

Fuhrman et al. (2010) suggested that in $k-\omega$ model type equations, roughness effects can be introduced by the modification of boundary condition for ω equation only. While implementing these boundary conditions, it is observed that modification of boundary conditions for k equation leads to convergence issues at higher values of k_s. This behavior was not reported by Knopp et al. (2009) or Aupoix (2014) and might be related to the solution method for turbulence models used in the solver which unfortunately is not highlighted in most of the literature. Fuhrman et al. (2010) explored the use of $dk/dy = 0$ i.e. the zero-Neumann boundary condition for rough walls and demonstrated that it gave similar results. For fully rough surfaces, it is physically true and therefore similar results are expected. However, it must be mentioned that the zero-Neumann boundary condition is not physically valid in the transitionally rough regime due to the presence of a buffer region. Both these boundary conditions are tested and the zero-Neumann boundary condition is found to be more stable at higher values of k_s. Even with the zero-Neumann boundary condition for k, convergence issues are observed for Aupoix-Cole BC and Aupoix-Niku BC at a high k_s when a fine mesh ($y^+ \approx 0.02$) is used. The use of Knopp BC is also accompanied by similar but less significant convergence issues. To overcome it, a mesh with slightly higher values of y^+ is used to reduce the stiffness of the k and ω equations. The variation of C_f for different wall spacing obtained using the low-Re turbulence model approach with Aupoix-Niku BC for $k_s = 1\text{x}10^{-3}$ is shown in Figure 3.2. The results for different meshes overlap indicating that the results are not affected by tested values of near-wall spacing. Therefore, all the simulations are carried out with $y^+ \approx 0.3$. Dirichlet boundary condition leads to stability issues even with the use

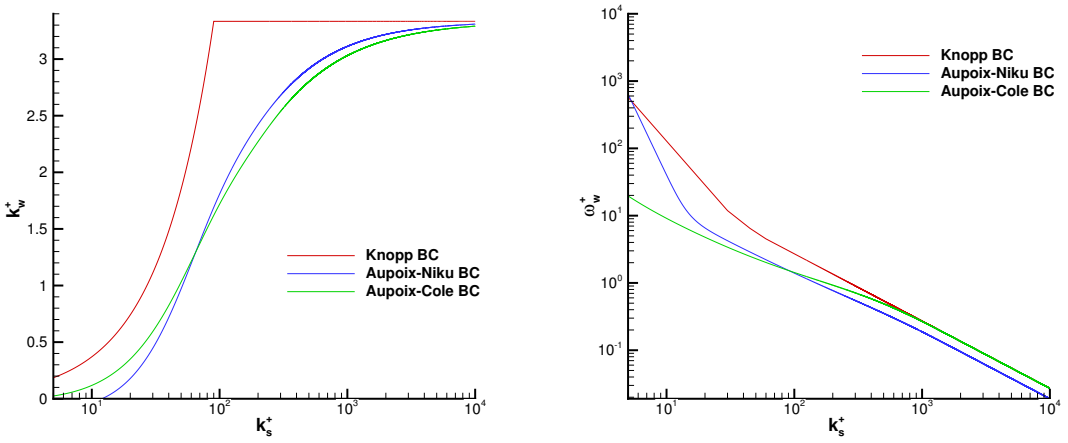

(a) (b)

Figure 3.1 a) k^+ and b) ω^+ as a function of k_s^+ for the three roughness corrections

of a coarse mesh. Therefore, the zero-Neumann is used instead of the Dirichlet boundary condition.

As a part of the study, the roughness extensions by Wilcox (1988), Knopp et al. (2009) and Aupoix (2014) are implemented in NSCODE. These boundary conditions are referred to as Wilcox BC, Knopp BC, Aupoix-Niku BC and Aupoix-Cole BC respectively. Modification of Wilcox extension by Hellsten et al. (1997) is not discussed due to convergence issues at high values of k_s^+.

3.3 Heat transfer treatment

The Reynolds analogy assumption is used to model the heat transfer for a smooth surface and it gives reasonably accurate predictions limited by the performance of the turbulence model used. The roughness extensions discussed in the previous section takes into consideration the roughness effects by setting a nonzero eddy viscosity at the wall. If the Reynolds analogy is used for rough surfaces, the roughness affects both momentum and heat transfer predictions equally. However, experimental evidence shows that the k_s determined using the skin friction or velocity profile shift measurement leads to an overprediction of heat transfer. This owes to the violation of the Reynolds analogy on rough surfaces (Aupoix and Spalart, 2003).

Aupoix (2015) introduced a model that was calibrated using DEM on different roughness elements types which were placed at several spacing ratios. This method accounts for thermal effects of roughness by modifying the turbulent Prandtl number, thereby, correcting the heat

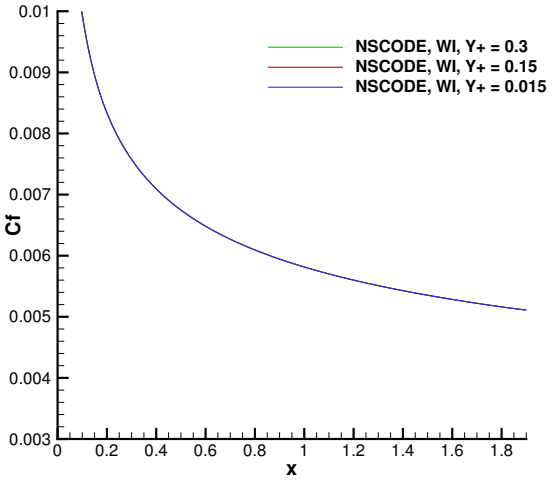

Figure 3.2 C_f variation for different wall spacing (y^+) using Aupoix-Niku BC at $k_s = 1\text{x}10^{-3}$

transfer in the near-wall region. The model modifies the turbulent Prandtl number in the following manner,

$$Pr_{t,r} = Pr_{t,s} + \Delta Pr_t \tag{3.16}$$

$$\Delta Pr_t = F(k_s^+, S_{corr})\ \mathrm{e}^{-y/h} \tag{3.17}$$

$$F(k_s^+, S_{corr}) = A\Delta u^{+2} + B\Delta u^+ \tag{3.18}$$

$$A = (0.0155 - 0.0035 S_{corr})\{1 - \exp[-12(S_{corr} - 1)]\} \tag{3.19}$$

$$B = -0.08 + 0.25\exp[-10(S_{corr} - 1)] \tag{3.20}$$

Heat transfer on rough surfaces is affected by turbulent diffusion and wetted surface effects: the first is related to the equivalent sand-grain roughness k_s and the roughness height h and the second to the corrected wetted surface ratio S_{corr}. S_{corr} and h are the new roughness measures introduced only for the heat transfer modeling. The method to determine the value of S_{corr} for a rough surface was mentioned by Danvin et al. (2017).

The model proposed by Aupoix is considered as an additional correction term that works along with the Spalart-Allmaras and $k - \omega$ SST turbulence model which are extended for roughness effects. Even though the model was originally developed for a roughness extension based on ONERA's strategy (Aupoix, 2007), it is used with the BOEING extension for the Spalart-Allmaras turbulence model.

3.4 Results and validation

The roughness extensions for the two turbulence models are validated in this section. In the legend, "WI" is used to refer to wall integration or low-Reynolds number turbulence model simulations. This is done so as to distinguish the wall function approach which is discussed in the next chapter. In some figures where the text in the legend seems to be too large, the text "NSCODE WI" is omitted. However, it still implies low-Re turbulence model simulations from NSCODE are used for those results. Due to a lack of experimental C_f and St distribution over airfoils, the validation is performed for rough flat plate cases. As the roughness extension is based on the shift of the logarithmic profile, it is justified to use a flat plate case for validation. This procedure for validation has been followed by several researchers (Aupoix and Spalart, 2003, Knopp et al. 2009) . Similar meshes are used for all cases. The domain of the flat plate is the same as the one used for flat plate validation in NASA Turbulence Modeling Resource (Center, 2018), however, with a farfield located at 20 m height. Inflow and outflow boundary conditions are used at the inlet and the outlet respectively. The mesh is divided into 8 blocks in streamwise and 1 in wall normal direction. The length of the plate and the Reynolds number varies with the validation cases. The mesh with 257 points in both streamwise and wall-normal directions is used as it gives mesh-independent results. The experimental and simulation data from other authors are extracted from figures using WebPlotDigitizer (Rohatgi, 2018) unless the tabulated data is provided. The density and turbulence variable residuals of 10^{-6} are ensured for all the simulations.

Test case: Semi-analytic relation by Mills and Hang (1983)

The results obtained with the roughness extensions for both turbulence models are compared to the relation by Mills and Hang (1983). They included the wake profile in the outer region of the boundary layer to the logarithmic velocity profile for rough walls and numerically integrated it to find the variation of skin friction coefficient for rough walls. The relation is given in Eq. (3.21).

$$C_f = \left[3.476 + 0.707\ln\left(\frac{x}{k_s}\right)\right]^{-2.46} \tag{3.21}$$

Note that Eq. (3.21) is based on the assumption of the fully rough regime from roughness function by Nikuradse (1933). However, $\kappa = 0.41$ was taken by Mills and Hang instead of $\kappa = 0.4$ obtained from the experiments by Nikuradse. The different values of equivalent sand-grain roughness that are tested are shown in Table 3.1. For this case, a Reynolds number of 1x10^7 is taken for a flat plate of a length of 2 m. In the figure, "HM" is used to refer to

solutions obtained using Eq. (3.21).

The results for the Spalart-Allmaras turbulence model are presented in Figure 3.3. The roughness extension implemented in NSCODE gives good predictions of C_f in comparison to those obtained from Eq. (3.21).

For $k-\omega$ SST turbulence model, the results obtained using different roughness extensions are shown in Figure 3.4. For the highest values of k_s, the Knopp BC gives predictions that are very close to those by Aupoix-Cole BC. The behavior can also be observed from ω^+ distribution shown in Figure 3.1. This is consistent with observations of Fuhrman et al. (2010). However, as the k_s decreases, Knopp BC increasingly underestimates the C_f. This behavior of Knopp BC is well-known in the transitional regime (Aupoix, 2014) and the results indicate that it continues until $k_s^+ \approx 150$. The predictions by Aupoix-Cole BC match closely with those obtained from the semi-analytic expression by Mills and Hang (1983). The Aupoix-Niku slightly overestimates the C_f in the spectrum of investigated k_s values. Aupoix-Niku roughness extension is based on Nikuradse profile with $\kappa = 0.4$, whereas the empirical relation by Mills and Hang uses $\kappa = 0.41$. This leads to the difference in results, especially at high k_s^+. The Wilcox BC massively underestimates the C_f because of the action of SST limiter as explained by Hellsten et al. (1997).

Test case: Experiments by Acharya et al. (1986)

Experiments were conducted by Acharya et al. (1986) on realistic roughness distributions that replicated the newly-finished blade surface of a water pump. Measurements of boundary layer parameters and skin friction coefficients were obtained for two surface types named as SRS1 and SRS2. These surfaces were tested at a velocity of 19 m/s and a zero pressure gradient. The detailed account of the surface statistics was provided by Tarada (1987). Using this data along with correlation of Grabow and White (1975), Aupoix (2007) obtained the value of equivalent sand-grain roughness for SRS1 and SRS2 as 0.524 mm and 1.064 mm respectively.

Figure 3.5 compares the results obtained from the Spalart-Allmaras turbulence model along with Boeing extension results from Aupoix and Spalart (2003) and the experimental results. SRS1 surface leads to $k_s^+ \approx 25$ which lies in the transitionally rough regime whereas SRS2 has

Table 3.1 k_s^+ values for different equivalent sand grain roughness heights

k_s (m)	5 x 10^{-3}	2 x 10^{-3}	1 x 10^{-3}	7 x 10^{-4}	5 x 10^{-4}
k_s^+	1450	530	250	170	120

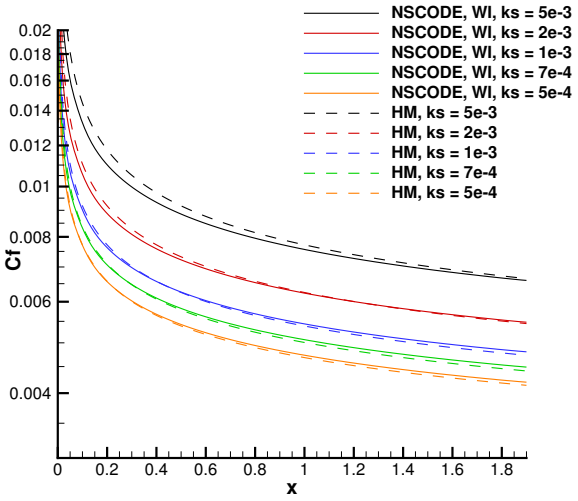

Figure 3.3 C_f distribution along the flat plate for different roughness heights with Spalart-Allmaras turbulence model

$k_s^+ \approx 60$ which is on the verge of the fully rough regime. It is observed that for both types of surfaces, the C_f is in good agreement with the experimental results. The C_f values obtained are higher than the ones obtained by Aupoix. For the smooth wall with the same input parameters, NSCODE also overestimates the C_f. This justifies the difference between the results for rough walls as well. The discrepancy in results might be due to the difference in the solver and the boundary conditions. Aupoix and Spalart (2003) used a boundary layer code whereas NSCODE is RANS solver. Note that the difference between NSCODE and Aupoix rough wall results is almost the same as the difference between the smooth wall results, implying a similar effect of roughness correction. Comparison of velocity profile could have provided a better validation of the roughness extension. Unfortunately, the velocity profile from the simulations by Aupoix and Spalart is not available.

The results for $k-\omega$ SST turbulence model are shown in Figure 3.6. It is observed that Knopp BC provide the closest estimation to experimental results. The C_f is again higher in comparison to the results obtained by Aupoix (2014) using the different roughness corrections and even for the smooth surface computation. The behavior is similar to the results obtained for the Spalart-Allmaras turbulence model and is subject to the same reasoning. Note that the use of zero-Neumann boundary condition for k might be the reason for this. As the present case lies in the transitionally rough regime in which this boundary condition is not physically valid, the use of it for this test case is questionable. Also, unexpected behavior was observed in the results by Aupoix using Knopp BC. Even though the behavior resembles a laminar-turbulent transition, the reason for this behavior was not explained by the author.

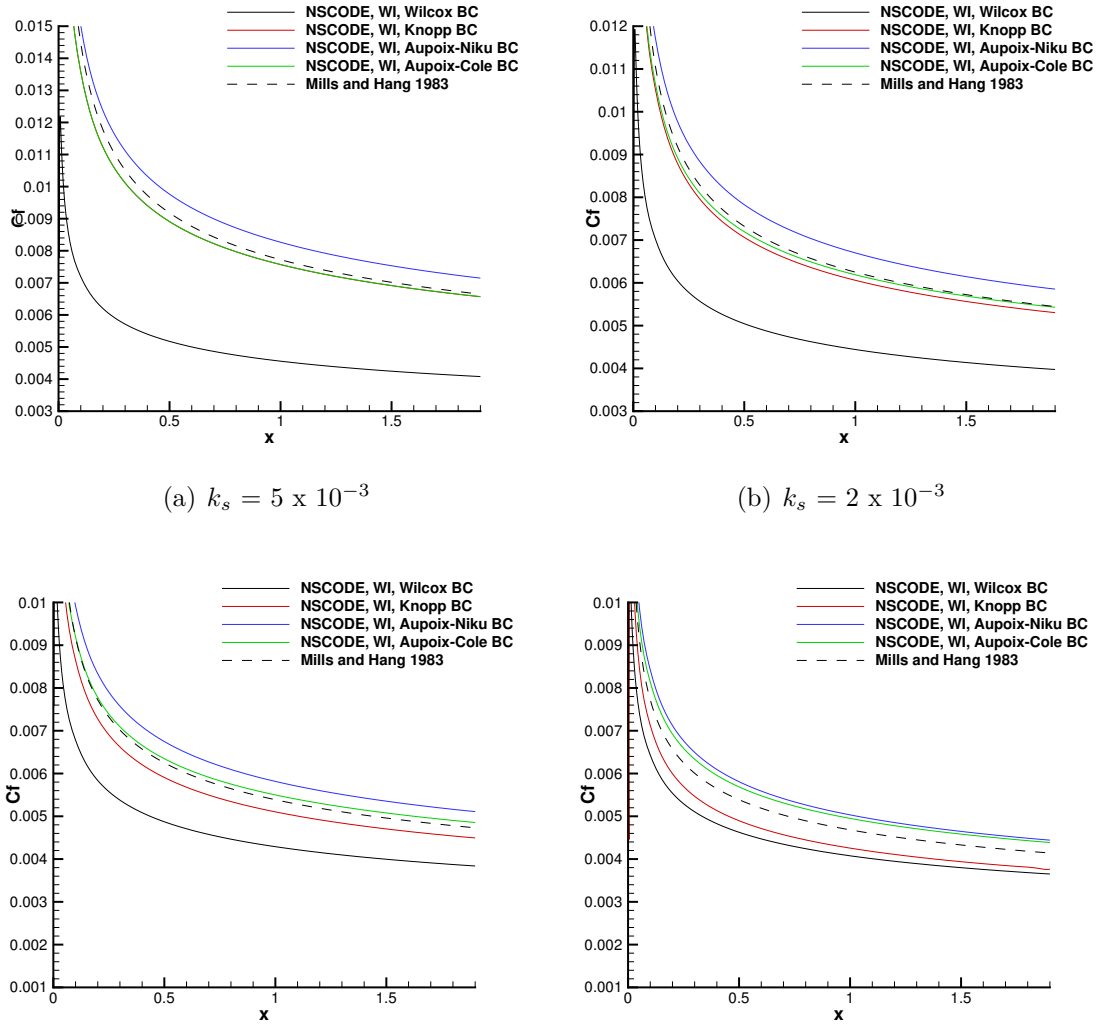

(a) $k_s = 5$ x 10^{-3}

(b) $k_s = 2$ x 10^{-3}

(c) $k_s = 1$ x 10^{-3}

(d) $k_s = 5$ x 10^{-4}

Figure 3.4 C_f distribution along the flat plate for different roughness heights with $k-\omega$ SST turbulence model using various roughness extensions

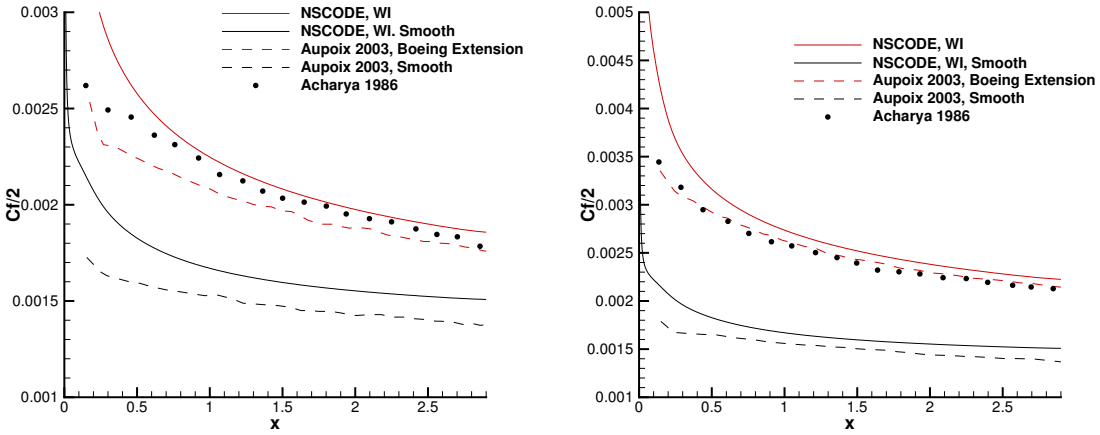

(a) (b)

Figure 3.5 Variation of C_f along the flat plate for the surfaces, a) SRS1 and b) SRS2 obtained using Spalart-Allmaras turbulence model

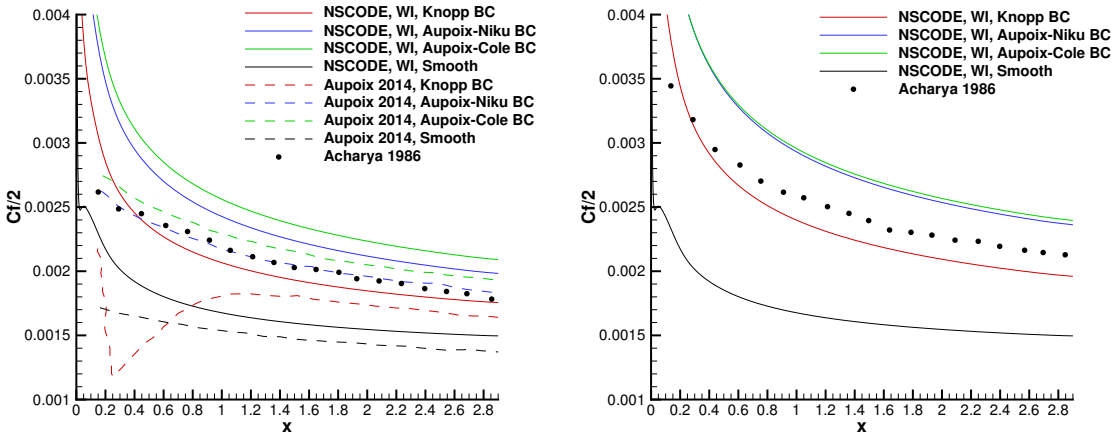

(a) (b)

Figure 3.6 Variation of C_f along the flat plate for the surfaces, a) SRS1 and b) SRS2 obtained using $k-\omega$ SST turbulence model

Test case: Experiments by Healzer et al. (1974)

Healzer et al. (1974) conducted experiments on flows over rough surfaces at several flow velocities. The surface was covered with closely packed spherical roughness elements of 0.635mm diameter. The equivalent sand-grain roughness was taken to be 1.25 times the diameter of the roughness element (Aupoix, 2015). As measurements of both C_f and St were given, this case is well suited for validating the thermal correction by Aupoix (2015).

From Figure 3.7, it is observed that the Spalart-Allmaras turbulence model gives a good prediction for C_f. However, the use of the Reynolds analogy overestimates St. When the thermal correction by Aupoix (2015) is incorporated, the St prediction is significantly improved. For $k-\omega$ SST turbulence model, the results are shown in Figure 3.8. It is observed that Knopp BC underestimates while Aupoix-Niku BC and Aupoix-Cole BC gives a good prediction of C_f. Similar behavior is also observed for the estimation of St. Overall, Aupoix-Cole BC gives the best prediction of both C_f and St. This implies that the thermal correction overcomes the limitations of using the Reynolds analogy for estimating the heat transfer and provides consistent predictions of both the skin-friction coefficient and Stanton number.

Test case: Experiments by Hosni et al. (1991)

Experiments conducted by Hosni et al. (1991) at Mississippi State University provides a good database of C_f and St variations over rough surfaces at several velocities. The experiments were based on hemispherical roughness elements with a height of 0.635mm. He tested different spacings between rows of roughness elements (l/d) of 2, 4 and 10. Here, l is the spacing between elements and d is the diameter of the roughness element. For the validation, the experimental results at a velocity of 58 m/s with roughness spacing of $l/d = 2$ are considered. More details about the experiments and detailed results can be found in the thesis of Hosni (1989). The equivalent sand-grain roughness is determined to be $k_s = 1.09$ mm using the correlation by Dirling (1973) (also used by Aupoix and Spalart (2003) and Knopp et al. (2009)). The values of h and S_{corr} are taken as 0.635 mm and 1.17 respectively (Chedevergne, 2018). Even though data for other velocities are available, $u = 58$ m/s is used because the same condition was tested by other researchers for the validation of their roughness correction (Aupoix and Spalart, 2003) (Knopp et al., 2009). Note that the Boeing extension results from Aupoix and Spalart (2003) are used for comparison.

For the Spalart-Allmaras turbulence model, the results are given in Figure 3.9. The C_f distribution matches closely with that of experimental results by Hosni et al. (1991) and simulation results by Aupoix and Spalart (2003). The Stanton number results are obtained

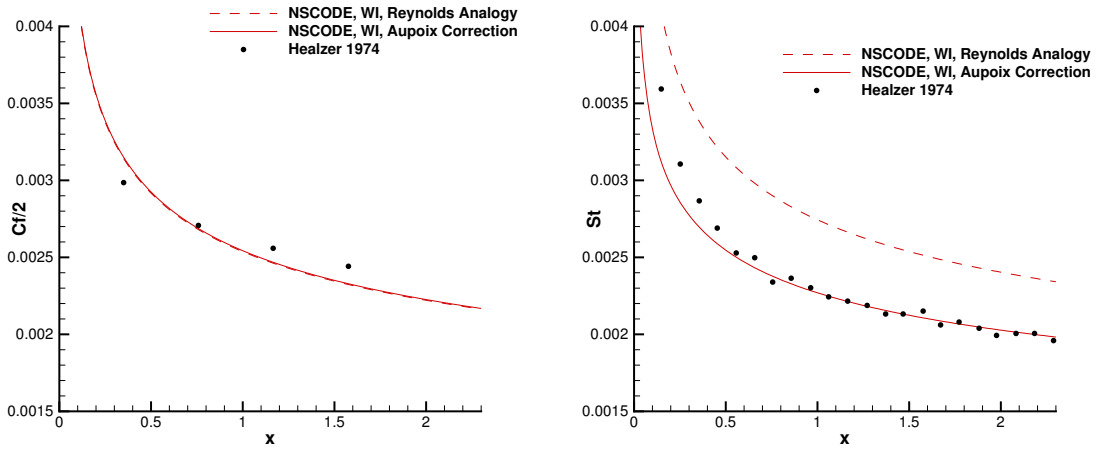

(a) (b)

Figure 3.7 a) C_f and b) St variation along the flat plate using Spalart-Allmaras turbulence model for the Healzer test case

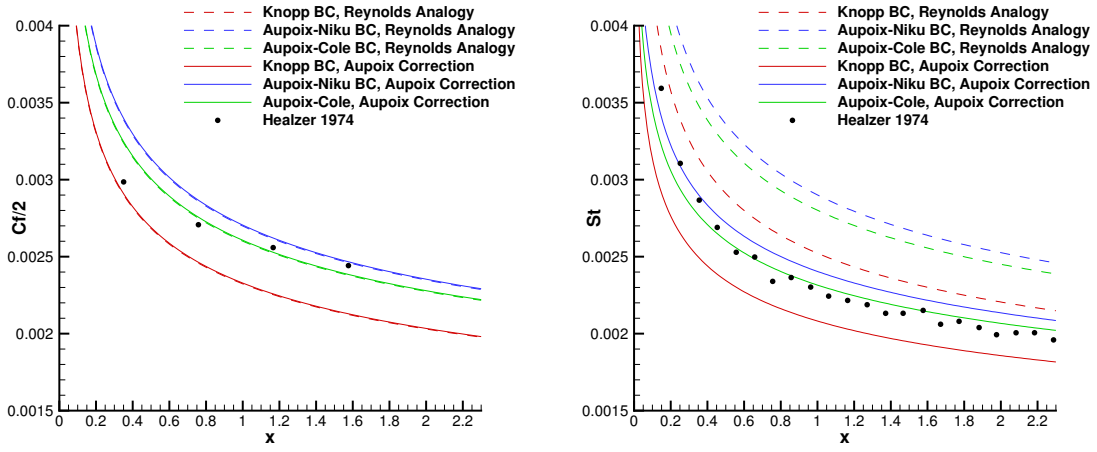

(a) (b)

Figure 3.8 a) C_f and b) St variation along the flat plate using $k-\omega$ SST turbulence model for the Healzer test case

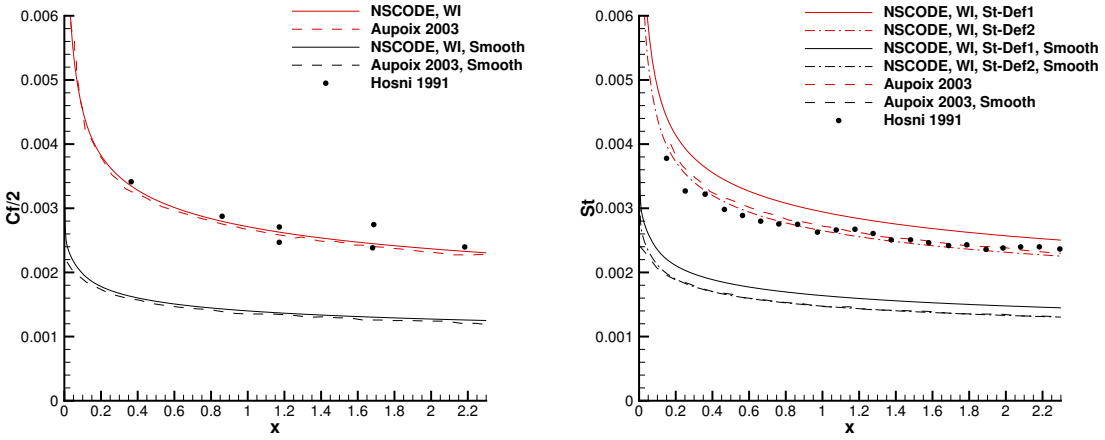

(a) (b)

Figure 3.9 a) C_f and b) St variation along the flat plate for $l/d = 2$ using Spalart-Allmaras turbulence model

using St-def1 and found to be higher than the one presented by Aupoix and Spalart. As the C_f distributions are matching with the results of Aupoix and both NSCODE and CLIC2 (code used by Aupoix and Spalart for their simulations) use the Reynolds analogy, the St results are also expected to match. Also, as the Reynolds Analogy is used to solve for energy equation, a good agreement for both C_f and St predictions with experimental results is not expected. The difference in results might be due to the use of different definitions for St. Unfortunately, Aupoix and Spalart (2003) did not mention the definition of St used for the computation. To assess the effect of this definition on St predictions, the results obtained using both St definitions (i.e. St-def1 and St-def2) are compared in Figure 3.9(b). The use of St-def2 leads to the St predictions that match well with the predictions by Aupoix and Spalart (2003) for both smooth and rough walls. Therefore, the definition used by them might be St-def2. Hosni et al. used total temperature (T_0) while computing experimental Stanton number. For the velocity case tested here, $T_{rec} \approx T_0$ and thus T_{rec} serves as a better reference temperature than T_∞.

Figure 3.10 shows the effect of the thermal correction by Aupoix (2015) on St predictions. The use of thermal correction significantly improves predictions. The results for $k - \omega$ SST turbulence model are presented in Figure 3.11. The experimental C_f results are scattered and therefore the three roughness corrections seem to provide good enough predictions. The C_f results are in good agreement with those presented by Aupoix (2014). Using the thermal correction by Aupoix (2015), Aupoix-Niku BC and Aupoix-Cole BC provide a good prediction of St whereas the Knopp BC underestimates it. The results for $l/d = 4$ shows a similar level

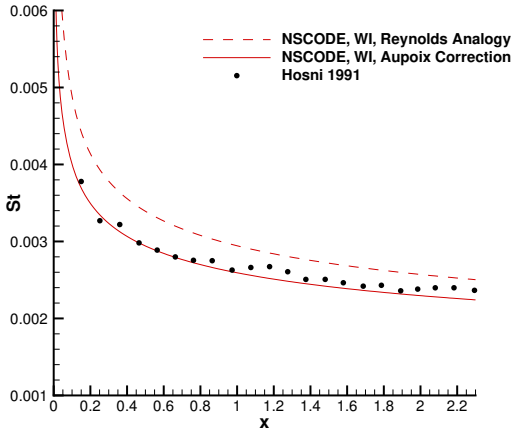

Figure 3.10 St variation along the flat plate for the experimental case of Hosni (1989) using Spalart-Allmaras turbulence model

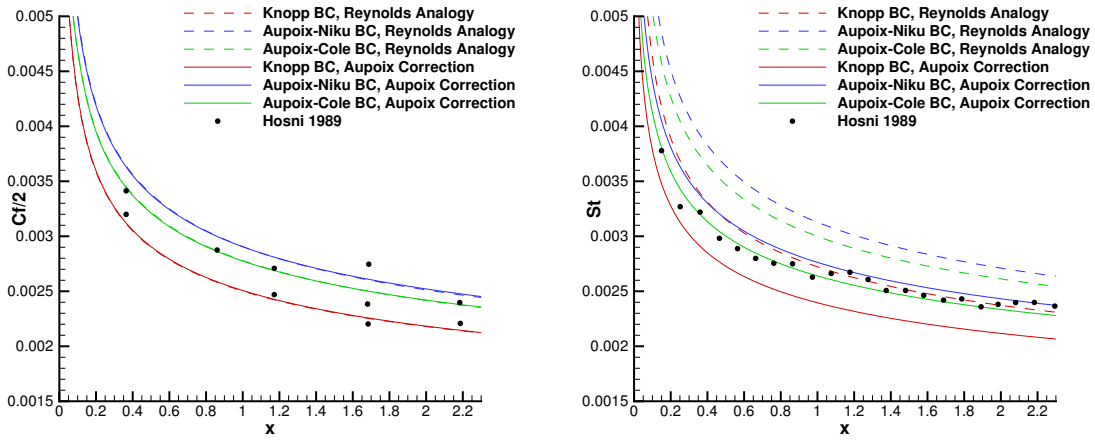

(a) (b)

Figure 3.11 a) C_f and b) St variation along the flat plate for $l/d = 2$ using $k - \omega$ SST turbulence model

of agreement, however, as the value of S_{corr} is not available in the literature, the results are not presented.

The comparison of various roughness extensions for $k - \omega$ SST turbulence model against different experimental results showed that Aupoix-Cole outperforms the other extensions and therefore, it is used in the next chapter to validate the wall function implementation.

CHAPTER 4 HIGH-RE TURBULENCE MODEL APPROACH

The roughness extensions discussed in the previous chapter give good predictions, however, at the cost of higher computational overhead. Wall functions are an effective approach to circumvent this issue. The derivation of standard wall functions for smooth walls is listed in Chapter 2. This chapter discusses the extension of log-law based wall functions for roughness effects. The idea of consistency between the roughness extension of wall functions and low-Re turbulence models is introduced to reduce the near-wall spacing dependency. The implementation of the smooth wall function approach and its roughness extension are then discussed. Lastly, the verification and validation of the wall function approach are performed. This is carried out in two steps. In the first step, the wall function approach is verified for smooth surfaces by considering a 2-D zero pressure gradient flat-plate case. The performance of wall functions in the presence of a curved profile and a pressure gradient is then tested by validating with the NACA 0012 airfoil results at 0° and 10° AoA. Both the skin-friction coefficient and Stanton number distributions are compared with the results. In the second step, the roughness extension of wall functions is validated. The near-wall spacing dependence of the proposed roughness extension is analyzed and the importance of consistent roughness extension is highlighted. This analysis also allows the selection of a y^+ value for performing the rest of the validation. Then, the friction drag obtained using the roughness extension is compared with a semi-empirical relation for a flat-plate case. Later, the validity of the roughness extension for different flow case is assessed by comparing both skin-friction coefficient and Stanton number distributions with low-Re turbulence model simulation results for the NACA 0012 airfoil. The roughness extension is further validated with two experimental cases. In the first case, three thermal corrections are analyzed for their capability to account for wetted surface area effects. The second case comprises of experimental Stanton number data over several iced-roughness distributions. Validation against this case shows the robustness of wall functions over a vast range of roughness parameters. The results presented in this chapter for the Spalart-Allmaras turbulence model are also a part of the publication by Prakash and Laurendeau (2019).

4.1 Wall function for smooth surfaces

With a plethora of wall functions available in the literature, the log-law and the look-up table based wall functions are implemented and tested. Analytical wall functions by Craft et al. (2002) are an attractive alternative as a considerable amount of work has been done

to extend it for rough surfaces. However, the complexity of the formulation which leads to a different implementation as compared to standard wall law, difficulty in the extension to unstructured 3-D RANS solvers and the restricted application to $k-\epsilon$ and $k-\omega$ turbulence models are the drawbacks which motivated the use of log-law based wall functions. The following wall function profiles are analyzed,

- Standard wall function (Eq. (2.27))
- Spalding wall function (Spalding, 1961, Eq. (2.33))
- Reichardt wall function (Reichardt, 1951, Eq. (2.34))
- Knopp wall function (Knopp et al., 2006, Eq. (2.35) or Eq. (2.36))
- Spalart-Allmaras wall model (Allmaras et al., 2012, Eq. (2.38))
- Look-up table (Kalitzin et al., 2005)

The comparison of these velocity wall function profiles is given in Appendix A. No significant difference in results is observed. The wall function profile by Spalding (1961) (Eq. (2.33)) is selected as the result is close to those obtained from low-Re turbulence model simulations.

To simulate heat transfer over the surface, the following wall function formulations are implemented.

- Kader wall function (Kader, 1981, Eq. (2.40))
- Jayatillaka wall function (Jayatillaka, 1969, Eq. (2.42))
- Arpaci wall function (Arpaci and Larsen, 1984, Eq. (2.44))
- Look-up table approach (Kalitzin et al., 2005)

The comparison of these temperature wall function profiles is discussed in Appendix A. The wall function used in the present study is based on the model by Jayatillaka (1969) given in Eq. (2.42) as the results are closer to the low-Re turbulence model results.

4.2 Extension to incorporate roughness

Wall functions are also used to model the effect of roughness. Suga et al. (2006) extended the AWF by Craft et al. (2002) by making the distribution of eddy viscosity a function of k_s. Apsley (2007) remarked the largely empirical nature of this function and improved it by performing the logarithmic expansion of the log-law velocity profile, thereby deriving a more physical expression. These wall functions were constructed keeping in mind the use of two-equation turbulence models. Goldberg and Batten (2017) highlighted the issue of lack of availability of rough wall function with heat transfer for the Spalart-Allmaras turbulence model and formulated a model to fill this research gap. The standard approach followed by commercial codes is also not consistent with the roughness extension of the low-Re turbulence models and does not ensure the near-wall spacing independence for a large range of k_s^+/y^+. There is a lack of literature discussing the near-wall spacing characteristics of rough wall functions. Except for the formulation by Suga, the mesh dependence characteristics of wall function were not discussed by the respective authors. For smooth walls, the inconsistency between the velocity profile and turbulence variables increases near-wall spacing dependence of wall functions and leads to errors (Durbin, 2009). The same reasoning applies to the treatment of turbulence variables in most rough wall function formulations. This section presents a strategy to ensure consistency of roughness extensions for wall functions and overcome most of these restrictions. The density and turbulence variable residuals of 10^{-6} are ensured for all the simulations.

4.2.1 Velocity wall function

Nikuradse (1933) showed that the roughness leads to a shift in the logarithmic region of the velocity profile as shown in Figure 2.3. This shift is quantified as a function of roughness Reynolds number (k_s^+) (given in Eq. (4.1))

$$\Delta u^+ = \frac{1}{\kappa}\ln k_s^+ + C - B \tag{4.1}$$

$$B = \begin{cases} 5.5 + \frac{1}{\kappa}\ln k_s^+ & 1 < k_s^+ \leq 3.5 \\ 6.59 + 1.52\ln k_s^+ & 3.5 < k_s^+ \leq 7 \\ 9.58 & 7 < k_s^+ \leq 14 \\ 11.5 - 0.7\ln k_s^+ & 14 < k_s^+ \leq 68 \\ 8.48 & 68 < k_s^+ \end{cases} \tag{4.2}$$

where $\kappa = 0.4$, $C = 5.5$ and B is given by Eq. (4.2). Aupoix (2014) pointed out the inconsistency resulting from the difference in the value of κ between the roughness correction and the chosen velocity profile. The difference in results is evident at higher values of k_s^+. In order to ensure consistency with the underlying turbulence model, $\kappa = 0.41$ is taken as it corresponds to the value in both Spalart-Allmaras and $k-\omega$ SST turbulence models. Nevertheless, the value of $\kappa = 0.4$ can also be used and it gives results closer to the Nikuradse roughness extension by Aupoix (2014) for $k-\omega$ SST turbulence model.

Colebrook and White (1937) also presented similar behavior in the presence of rough walls and their data was expressed in the form of relation by Grigson (1992) (Eq. (4.3)).

$$\Delta u^+ = \frac{1}{\kappa}\ln\left(1 + \frac{k_s^+}{e^{3.25\kappa}}\right) \tag{4.3}$$

These roughness functions are graphically represented in Figure 4.1. Other researchers also proposed roughness functions, for instance, the function by Ligrani and Moffat (1986). The present work is restricted to the above two roughness functions. Note that the use of other roughness functions would involve a similar strategy without considerable changes.

As shown in Chapter 3, in the presence of a rough wall, the velocity profile can be expressed in terms of a smooth velocity profile by introducing a shift in the wall. Chedevergne (2018) derived Eq. (4.5) by integrating the formulation behind the low-Reynolds number turbulence model extension for roughness by Aupoix (2007) (given in Eq. (4.4)).

$$\frac{du_r^+}{dy^+}(y^+) = \frac{du_s^+}{dy^+}(y^+ + y_0^+) \tag{4.4}$$

$$u_r^+(y^+) = u_s^+(y^+ + y_0^+) - u_s^+(y_0^+) \tag{4.5}$$

$$\Delta u^+ = u_s^+(y_0^+) \tag{4.6}$$

where y_0^+ is the shift at the virtual wall and subscripts r and s indicate rough and smooth wall respectively. From Eq. (4.6), the value of y_0^+ can be found for both Nikuradse and Colebrook-Grigson relations. The underlying assumption is based on the presence of a fully rough regime ($k_s^+ > 68$) where the viscous sublayer vanishes. Therefore, even the use of y_0^+ that models the transitionally rough regime is questionable to the accuracy of the model in the regime. On a side note, there is no general treatment for the transitionally rough regime as the results vary significantly with the roughness element shape and distribution.

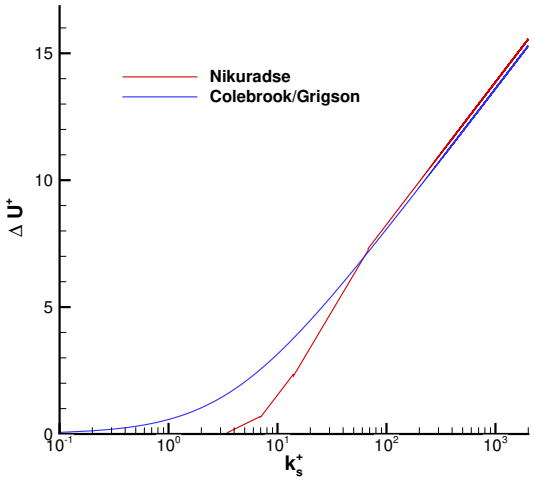

Figure 4.1 Comparison of Nikuradse and Colebrook-Grigson roughness functions

This is evident by comparing experimental results by Nikuradse (1933) and Colebrook and White (1937). It hinders the derivation of a single model that gives good predictions in the transitionally rough regime for any general roughness.

4.2.2 Temperature wall function

The strategy adopted for the temperature profile is similar to that for the velocity wall function. Eq. (4.7) is integrated to obtain Eq. (4.8). In this case, the limits of integration are different as compared to the velocity profile case. The presence of the conduction sublayer in the fully rough regime leads to a positive T^+ value at the shifted wall (MacDonald et al., 2019). Therefore, the limits of integration are different as compared to the velocity profile.

$$\frac{dT_r^+}{dy^+}(y^+) = \frac{dT_s^+}{dy^+}(y^+ + y_0^+) \tag{4.7}$$

$$T_r^+(y^+) = T_s^+(y^+ + y_0^+) - \Delta T^+ \tag{4.8}$$

$$\Delta T^+ = T_s^+(y_0^+) - T_0^+ \tag{4.9}$$

$$T_0^+ = \frac{1}{St_k} = \frac{1}{C} Re_k^m Pr^n \tag{4.10}$$

This general form is useful for extending any temperature profile over the rough wall. Note that the temperature profile by Kays and Crawford (1993) or the one by Radenac et al. (2018) could also be interpreted in this form. This form is important when using the look-up table approach with rough walls. The Reynolds analogy for modeling the heat transfer is represented in the wall-function form as follows,

$$\Delta T^+ = T_s^+(y_0^+) \tag{4.11}$$

This leads to an inconsistency between C_f and St estimates. The use of Reynolds analogy for wall-functions is a good verification against the low-Re turbulence models especially for complex geometries or in situations where there is a lack of experimental data. In this thesis, it is used to compare the results for heat transfer over a rough NACA 0012 airfoil.

In Eq. (4.9), T_0^+ is the additional correction term to overcome the Reynolds analogy assumption for the temperature profile over a rough surface. This term arises to take into account the conductive heat transfer for semi-stagnant fluid in roughness cavities (Kays and Crawford, 1993). It was determined and correlated from the experimental data by Dipprey and Sabersky (1963) and is given by Eq. (4.10). The value of m and n are 0.2 and 0.44 respectively, where $C = 0.8$ based on experiments over spherical roughness elements (Pimenta et al., 1975). Owen and Thomson (1963) considered a 3-D flow across the cavities and determined the coefficients m and n to be 0.45 and 0.8 respectively. The value of C is taken as 1.92 for an arbitrarily shaped roughness case.

Recently, Aupoix (2015) suggested another way to remove the inconsistency between C_f and St by including two additional parameters of roughness metrics. The use of Eq. (4.10) performs a similar role, however, the expression described above does not incorporate the role of corrected surface area (wetted area) which is an important physical parameter to accurately predict the heat transfer. Chedevergne (2018) suggested a modification of the turbulent viscosity variation in the roughness extension by Suga et al. (2006) and incorporated the effect of the corrected surface area. Being an extension of AWF, it suffers from similar limitations as the base model. Radenac et al. (2018) formulated an equivalent expression for T_0^+ by incorporating the model of Aupoix (2015) in the Integral Boundary Layer (IBL) method. This expression is given as,

$$T_0^+ = \frac{F(k_s^+, S_{corr})}{\kappa} e^{y_0^+/k^+} \Big[Ei\Big(-\frac{y^+ + y_0^+}{h^+} \Big) - Ei\Big(-\frac{y_0^+}{h^+} \Big) \Big] \tag{4.12}$$

where $h^+ = hu_\tau/\nu$ and h is the roughness height. $Ei(x)$ is the exponential integral function

which is numerically evaluated using the algorithm specified by Press et al. (1992), or it is obtained from a database of the values. The latter is found to be slightly faster than the former and hence, it is used in the study. This formulation is exported to the wall function framework. With the value of T_0^+ derived in Eq. (4.12), this novel wall function approach greatly improves the capability to accurately predict heat transfer over rough surfaces. The advantage of using this formulation is that it has a more physical basis and is easily extensible to any general purpose CFD code. The implementation by Chedevergne (2018) is restricted to $k-\omega$ type turbulence models. The proposed wall function approach does not pose this restriction and is applicable for any turbulence model when used with suitable wall function boundary condition. In the present thesis, the formulation is validated for the Spalart-Allmaras and $k-\omega$ SST turbulence model.

4.3 Implementation of wall functions

The numerical implementation of wall functions involves the steps shown in Figure 4.2.

4.3.1 Smooth walls

Computation of wall parallel velocity

The velocity component parallel to the wall ($\bar{V_t}$) is determined as $\bar{V_t} = \bar{V} - (\bar{V}.\hat{n})\hat{n}$ where $\bar{V}$ is the velocity vector, $\hat{n}$ is the normal vector to the surface. For convenience, $\bar{V_t}$ is represented as u which is the velocity of the assumed Couette flow close to the wall.

Relaxation of wall function equation

Wall functions can be written in the form given in Eq. (4.13).

$$f(y^+) = y^+u^+(y^+) = \frac{yu}{\nu} = Re_y \tag{4.13}$$

where Re_y can be referred to as the wall normal Reynolds number. For log-law based wall functions, $f(y^+)$ is a non-linear equation which is relaxed using the Newton-Raphson method to obtain the value of y^+ and u^+. The algorithm used for the Newton-Raphson method is given in Algorithm 1. tol is the tolerance which is selected to be 10^{-4}. For the look-up table approach, this step is replaced by a search algorithm to read the value of tabulated y^+ and u^+ corresponding to a given Re_y.

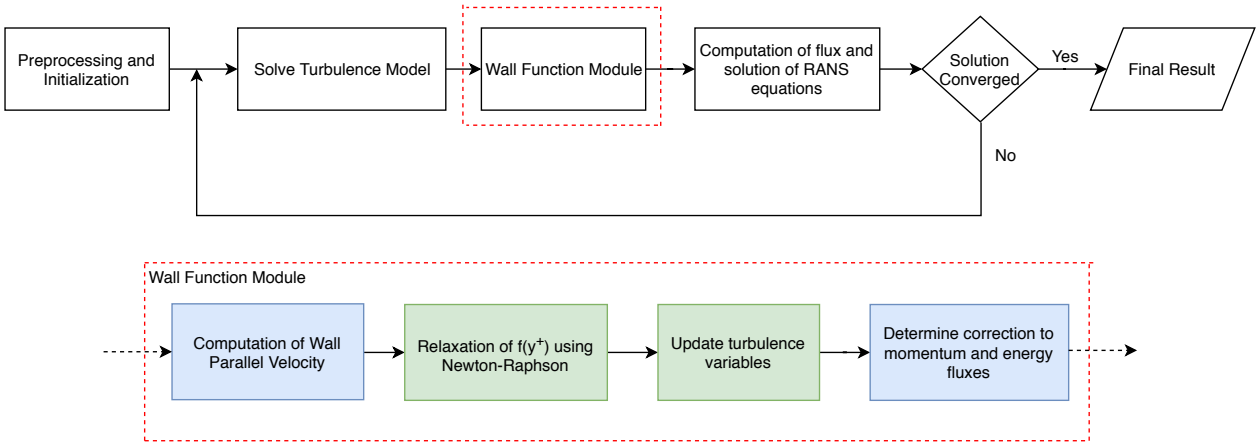

Figure 4.2 Flow chart of RANS computation with wall function

Table 4.1 Functions for Newton-Raphson for the smooth walls

x	$F(x)$	$F'(x)$
u^+	$u^+\left[u^+ + e^{-\kappa B}\left(1 - e^{\kappa u^+} - \frac{(u^+)}{1!}...\right)\right] - Re_y$	$2u^+ + e^{-\kappa B}\left(e^{\kappa u^+}(1+\kappa u^+) - 1...\right)$
$\tilde{\nu}^+$	$\tilde{\nu}^4/(\tilde{\nu}^3 + c_{v1}^3) - \nu_t$	$\tilde{\nu}^6 + 4\tilde{\nu}^3 c_{v1}^3/(\tilde{\nu}^3 + c_{v1}^3)^2$

Algorithm 1: Algorithm for Newton-Raphson

Result: Determine x for $F(x) = 0$

Initialize x;

while $\frac{x - x_o}{x_o} < tol$ **do**

  $x_o = x$;

  $x = x_o$ - $\frac{F(x)}{F'(x)}$;

end

The value of y^+ obtained from relaxation of $f(y^+)$ is used along with Eq. (2.42) to obtain T^+.

Update turbulence variables

The turbulence model is solved over a coarse mesh which involves the use of incorrect gradients of flow and turbulence variables near the wall. Appropriate boundary conditions must be provided along with the update of the value of computed turbulent viscosity. For smooth walls, the boundary conditions can be defined two ways,

- Production term in the turbulence model is modified and the boundary conditions are used similar to the low-Re turbulence model.

- The value of the turbulence variables are defined on the wall cells and off-the-wall boundary condition (Kalitzin et al., 2005) is used.

Both are tested and gave similar results for smooth walls, however, the first exhibited stability and accuracy issues at high values of k_s when applied to the rough wall function formulation. Therefore, the second approach is finally used. The turbulent viscosity at the wall cells is specified by using Eq. (2.24). The value of du^+/dy^+ can be analytically derived from the wall function profile. The value for the Spalding (1961) profile is given in Eq. (4.14).

$$\frac{dy^+}{du^+} = \frac{1}{du^+/dy^+} = 1 + ke^{-kB}\left(e^{ku^+} - 1 - ku^+ - \frac{1}{2}(ku^+)^2 - ...\right) \tag{4.14}$$

The boundary conditions for the turbulence variables are defined as follows,

Spalart-Allmaras turbulence model: Relaxing Eq. (4.15) using Newton Raphson gives the value of $\tilde{\nu}$ in the wall cells. Eq. (4.15) is obtained by using Eq. (2.7) and substituting the value of f_{v1}. For solving Eq. (4.15) using Newton-Raphson, the value of $F(x)$ and $F'(x)$ when $x = \tilde{\nu}$ is shown in Table 4.1.

$$(\tilde{\nu}^+)^4 = \nu_t^+\left((\tilde{\nu}^+)^3 + C_{v1}^3\right) \tag{4.15}$$

Imposing a Dirichlet boundary condition ($\tilde{\nu}_w = 0$) is also tested and leads to no difference in the results for higher values of y^+. However, it is preferable to use the Dirichlet boundary condition when the first cell is in the viscous sublayer.

$k-\omega$ **SST turbulence model**: Setting of boundary conditions for this turbulence model is more complicated than for Spalart-Allmaras turbulence model, as unlike the latter model, the analytical expressions of k and ω are not available for the entire inner region. The expressions for viscous sublayer (Eq. (4.16)) and logarithmic region (Eq. (4.17)) are as follows,

For the viscous sublayer,

$$k^+ = 0, \quad \omega^+ = \frac{6}{\beta_1(y^+)^2} \tag{4.16}$$

For the logarithmic layer,

$$k^+ = \frac{1}{\sqrt{C_\mu}}, \quad \omega^+ = \frac{1}{\kappa\sqrt{C_\mu}y^+} \tag{4.17}$$

In these equations, c_μ is the same as β^* in the turbulence model formulation. In the buffer region, the value is estimated by interpolating from the corresponding values in viscous sublayer and logarithmic region. Menter et al. (2003) introduced "automatic wall treatment"

which involved the interpolation or blending formula given in Eq. (4.18).

$$\omega^+ = \sqrt{(\omega^+_{visc})^2 + (\omega^+_{log})^2} \tag{4.18}$$

Here, ω^+_{visc} and ω^+_{log} are the values of ω^+ given in Eq. (4.16) and Eq. (4.17) respectively. They also used a no-flux boundary condition for k^+. While this boundary condition for k holds for viscous sublayer and logarithmic region, it is not true in the buffer layer. Therefore, Kalitzin et al. (2005) suggests the determination of k^+ from Eq. (4.19).

$$k^+ = \nu^+_t \omega^+ = \Big(\frac{du^+}{dy^+} - 1\Big)\omega^+ \tag{4.19}$$

Other interpolation formula for the buffer also exists (Knopp et al., 2006)(Popovac and Hanjalic, 2007). These three blending formulations are tested, and they gave close results. The blending formulation by Menter et al. (2003) with the boundary condition of k by Kalitzin et al. (2005) is used for the simulations. For the look-up table approach, the boundary conditions described above can be used or the tabulated values of $\tilde{\nu}^+$, k^+, ω^+ and μ^+_t can be read. Both lead to similar results. For the wall cell center in the viscous sublayer, a Dirichlet boundary condition for k is preferable.

Correction of wall fluxes

Velocity and temperature gradients are used along with the value of turbulent viscosity to estimate the turbulent momentum and heat transfer fluxes. The use of a coarse mesh with wall functions leads to incorrect computation of the gradients and the fluxes. Therefore, the gradients at wall cells must be replaced by the correct value. y^+, u^+ and T^+ obtained in the second step in the wall function module provide values of u_τ and T_τ which are used to obtain the wall shear stress (τ_w) and wall heat flux (q_w) respectively. An effective eddy viscosity can be used to substitute the effect of these corrected fluxes. Nichols and Nelson (2004) reported that determining the effective wall eddy viscosity leads to errors in the energy equation calculation. Hence, the coordinate transformation approach by Sondak (1992) is used to transform the shear stress tensor and the heat transfer vector into the computational domain.

4.3.2 Rough walls

The use of wall functions for simulating flows over rough walls involves only minute implementation changes. These modifications are incorporated into the two steps marked green in

the flowchart. The other two steps remain the exact same.

Relaxation of wall functions

Roughness function is introduced in the equation (Eq. (4.20)). This results in the following form,

$$f(y^+) = Re_y = u_r^+ y^+ \tag{4.20}$$

where u_r is given by Eq. (4.5) with Δu^+ taken from Nikuradse (Eq. (4.1)) or Colebrook-Grigson (Eq. (4.3)) roughness functions. With Spalding profile taken as u_s^+, Eq. (4.6) is used to obtain y_0^+. There are analytical expressions for y_0^+ available in the literature. Chedevergne and Aupoix (2017) derived the expression for y_0^+ considering the velocity profile by Reichardt (1951). The value of y_0^+ is obtained from the wall function profile as it maintains the consistency with the implementation and reduces the near-wall spacing dependence of wall function approach.

For the temperature wall function, Eq. (4.8) is used along with the values of y_0^+ and y^+ obtained by solving for the rough velocity wall function. The solution for the Reynolds analogy assumption is obtained by setting $T_0^+ = 0$.

Update of turbulence variables

The shift of the wall introduced for the rough walls requires the modification of the boundary condition of turbulence variables. The value of turbulence viscosity at the first cell ($\mu_{t,r}$) and at the wall ($\mu_{tw,r}$) are obtained from Eq. (4.21).

$$\mu_{t,r}(y^+) = \mu_{t,s}(y^+ + y_0^+), \quad \mu_{tw,r} = \mu_{t,s}(y_0^+) \tag{4.21}$$

The boundary conditions for the turbulence model can be described as,

Spalart-Allmaras turbulence model: The value of $\tilde{\nu}$ at the wall cell is found from Eq. (4.22).

$$\tilde{\nu}_r^+(y^+) = \tilde{\nu}_s^+(y^+ + y_0^+) \tag{4.22}$$

$$\tilde{\nu}_{r,w}^+ = \tilde{\nu}_{s,w}^+(y_0^+) \tag{4.23}$$

Off-wall boundary condition is imposed with the value of $\tilde{\nu}$ obtained by relaxing Eq. (4.22) using the Newton-Raphson method. For low values of y^+, a Dirichlet boundary condition (Eq. (4.23)) gives slightly better predictions. In order to reduce the near-wall spacing dependence of wall function formulations, it is also important to incorporate the modifications to the turbulence model that ensures consistency between the low-Re and high-Re turbulence model roughness extensions. Therefore, the value of y_0 used to modify wall distance in the low-Re turbulence model formulation must be set as per the y_0 obtained from the wall function formulation. The modification introduces a non-local parameter in the turbulence model as the y_0 for each cell in space must be linked to a wall cell. However, it is important to improve the results at low y^+. At a large y^+, the results are not significantly affected by this modification. As the y_0 also takes into account the transitionally rough regime, the modification introduced in the damping function for the low-Re turbulence model approach (Eq. (3.7)) is not needed. Therefore, c_{R1} must be set to 0.

$k-\omega$ **SST turbulence model**: Setting of the boundary condition for $k-\omega$ SST turbulence model is primarily based on the assumption of the fully rough regime. Therefore, the expressions for k and ω is determined from its behavior in the logarithmic region. Off-wall boundary condition can be imposed in three ways.

- The first way is to find the value of k and ω at $y^+ + y_0^+$ from the expression given in Eq. (4.17). It is further referred to as Rough BC 1 and the values of turbulence variables are then defined as,

$$k^+ = \frac{1}{\sqrt{C_\mu}}, \quad \omega^+ = \frac{1}{\kappa\sqrt{C_\mu}(y^+ + y_0^+)} \tag{4.24}$$

- The other way is to define the value of k^+ from the Eq. (4.24) and determine ω^+ from Eq. (4.19). This is referred to as Rough BC 2.

$$k^+ = \frac{1}{\sqrt{C_\mu}}, \quad \omega^+ = \frac{k^+}{\nu_t^+(y^+ + y_0^+)} \tag{4.25}$$

- The third way is to impose the value of ω^+ based on Eq. (4.24) and determine k^+ from Eq. (4.19). This is referred to as Rough BC 3 and the value of turbulence variables are defined as,

$$k^+ = \omega^+\nu_t^+(y^+ + y_0^+), \quad \omega^+ = \frac{1}{\kappa\sqrt{C_\mu}(y^+ + y_0^+)} \tag{4.26}$$

The interpolation function for the buffer layer (Eq. (4.18)) is used to interpolate the value for the transitionally rough regime. The use of this interpolation function improves the near-wall spacing dependence at low y^+ values in the transitionally rough regime. The comparison of these three boundary conditions is given later in the chapter. Note that the second and the third type of boundary condition enforces consistency with k^+, ω^+ and ν_t^+.

4.4 Verification and validation

The wall function implementation is systematically verified and validated. This process first involves the comparison of results with canonical flow cases and then application case i.e. rough walls are considered. The validation is performed on two geometries: flat plate and airfoil. For the flat-plate cases with rough surfaces, the domain and boundary conditions are the same as those used in the previous chapter. For NACA 0012 airfoil cases, an 'O' grid mesh is used with 600-800 and 129 points in streamwise and wall-normal directions respectively. For flat plate cases, the mesh with 257 points in both streamwise and wall-normal directions is used. This distribution of points leads to mesh-independent results. The wall functions are first validated for smooth walls, followed by the validation for rough walls. For both smooth and rough walls, the results are compared with the empirical and experimental results for the case without heat transfer (adiabatic wall boundary condition) and with heat transfer (isothermal wall boundary condition). It is observed that the numerical scheme and the artificial dissipation deteriorated the wall function results. A discussion on this is presented in Appendix B. Based on it, the value of constant for fourth order dissipation term ($\kappa^{(4)}$) is taken to be $\frac{1}{1024}$. For airfoil case, it leads to stability issues so $\kappa^{(4)} = \frac{1}{128}$ is used.

4.4.1 Smooth walls

Cases with smooth walls serve as the first step in the validation and verification of the wall function module. Comparison of the results with a simple case i.e. 2D zero pressure gradient flat plate case provides the necessary verification of the implementation. The results are then compared to NACA 0012 airfoil at 0° and 10° angle of attack.

Test case: 2D zero pressure gradient flat plate

The 2D zero pressure gradient flat plate case from NASA Turbulence Modeling Resource (Center, 2018) is used to verify and validate the wall function implementation for smooth walls. The resource offers precise case parameters to carry out simulations in a compressible flow solver. In addition to the skin-friction coefficient distribution, the data for u^+ and ν_t^+

distribution in the wall normal direction is also available.

Table 4.2 Case parameters - Flat plate validation

Plate length (m)	**Reynolds Number**	**Mach Number**
2	1 E+07	0.2

Meshes with different first cell heights are used to check the validity of wall functions at different y^+ values. The designation of the meshes is mentioned in Table 4.3. Figure 4.3 shows the near-wall region of the different meshes used. It is clear from the figure that the number of mesh layers used to resolve the turbulent boundary layer drastically increases from Mesh 1 to Mesh 6. Mesh WI is the mesh used for low-Re turbulence model simulations.

Table 4.3 First cell height for different meshes and the corresponding y^+ for the flat plate case

Mesh Name	**First cell height (m)**	y^+
Mesh 1	2 x 10^{-3}	180
Mesh 2	1 x 10^{-3}	90
Mesh 3	5 x 10^{-4}	50
Mesh 4	1 x 10^{-4}	12
Mesh 5	1 x 10^{-5}	0.8
Mesh 6	1 x 10^{-6}	0.1
Mesh WI	1 x 10^{-7}	0.01

The wall function results are compared with those from the low-Re turbulence model and CFL3D simulations (obtained from Center, 2018). The case parameters for the simulations are shown in Table 4.2. From Figure 4.4, it is observed that the wall function results match well for the C_f distribution and velocity profile for all the mesh tested except Mesh 4. The

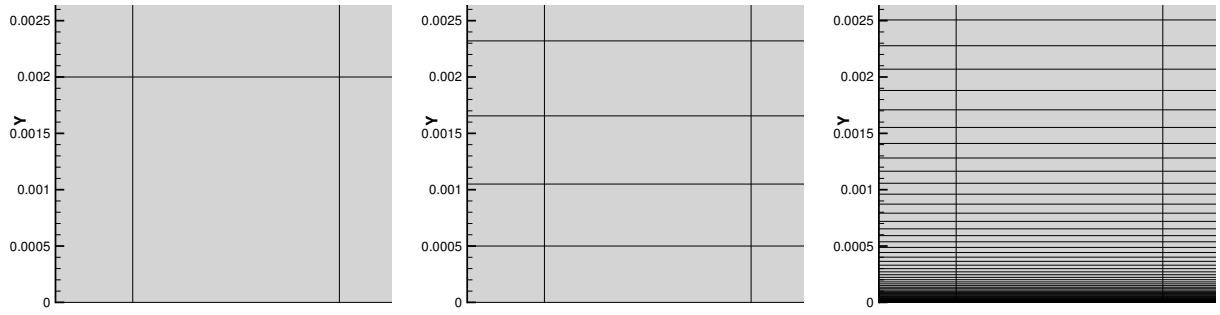

(a) Mesh 1 (b) Mesh 3 (c) Mesh 6

Figure 4.3 Meshes with different near-wall spacing

cell center in Mesh 4 case lies in the buffer layer and therefore a deviation from the low-Re turbulence model result is expected. Similar deviation in the buffer layer was also reported by Kalitzin et al. (2005). The non-linearity in the $\tilde{\nu}$ distribution in the buffer layer leads to significant errors in gradient computation in the second layer of cells near the wall. Kalitzin et al. (2005) suggested the correction of the viscous fluxes on the interface of the first and the second mesh layer to reduce these errors. The ν_t^+ distribution (Figure 4.4(e)) also compares well with the other results. Deviation in ν_t^+ for higher y^+ values is the result of low local Reynolds number in the starting region of the flat plate. Wall functions are based on the assumption of large separation of turbulent and viscous scales which is not present at low local Reynolds numbers. Therefore, the velocity profile at a low Reynolds number does not respect the logarithmic law. As the Reynolds number increases, the width of the log-region and hence the validity of wall functions increases to higher y^+ values. Figure 4.4(f) indicates that at a further downstream location (higher Reynolds number), the ν_t^+ profile matches well for the coarser mesh case. The same reasoning also applies to the higher C_f distribution for coarser meshes when compared to low-Re simulation results at the leading edge of the plate.

As NASA Turbulence Modeling Resource does not provide the data for the heat transfer, the St distribution from wall functions is compared to low-Re turbulence model simulations and the empirical correlation by Reynolds et al. (1958) (Eq. (4.27)). Figure 4.4(c) shows a good agreement between the St obtained from wall functions and other results. The St shows a slightly greater grid dependence as compared to C_f results i.e. the results are more spread out at high values of y^+. The reason for this is the different slopes of the assumed analytical temperature profile and the one obtained from low-Re turbulence model simulations. The comparison of temperature profiles with the semi-analytic solution is not ideal for compressible flows due to the action of the viscous dissipation term in the energy equation. This is further discussed in Appendix A. The important thing is that the temperature profiles obtained from wall function simulations are in good agreement with that from low-Re turbulence model simulations. Note that Figures 4.4 and 4.5 show the C_f distribution for an adiabatic wall case. The distribution for an isothermal wall differs slightly from the adiabatic wall.

$$St = 0.185(\log_{10} Re_x)^{-2.584} Pr^{-0.4} \tag{4.27}$$

Similar results are also obtained for the $k-\omega$ SST turbulence model. Figure 4.5 shows that the deviation in C_f and St distributions when the first cell center is in the buffer layer is not as much as the Spalart-Allmaras turbulence model. The corresponding velocity and temperature profiles also match better with the low-Re turbulence model profile.

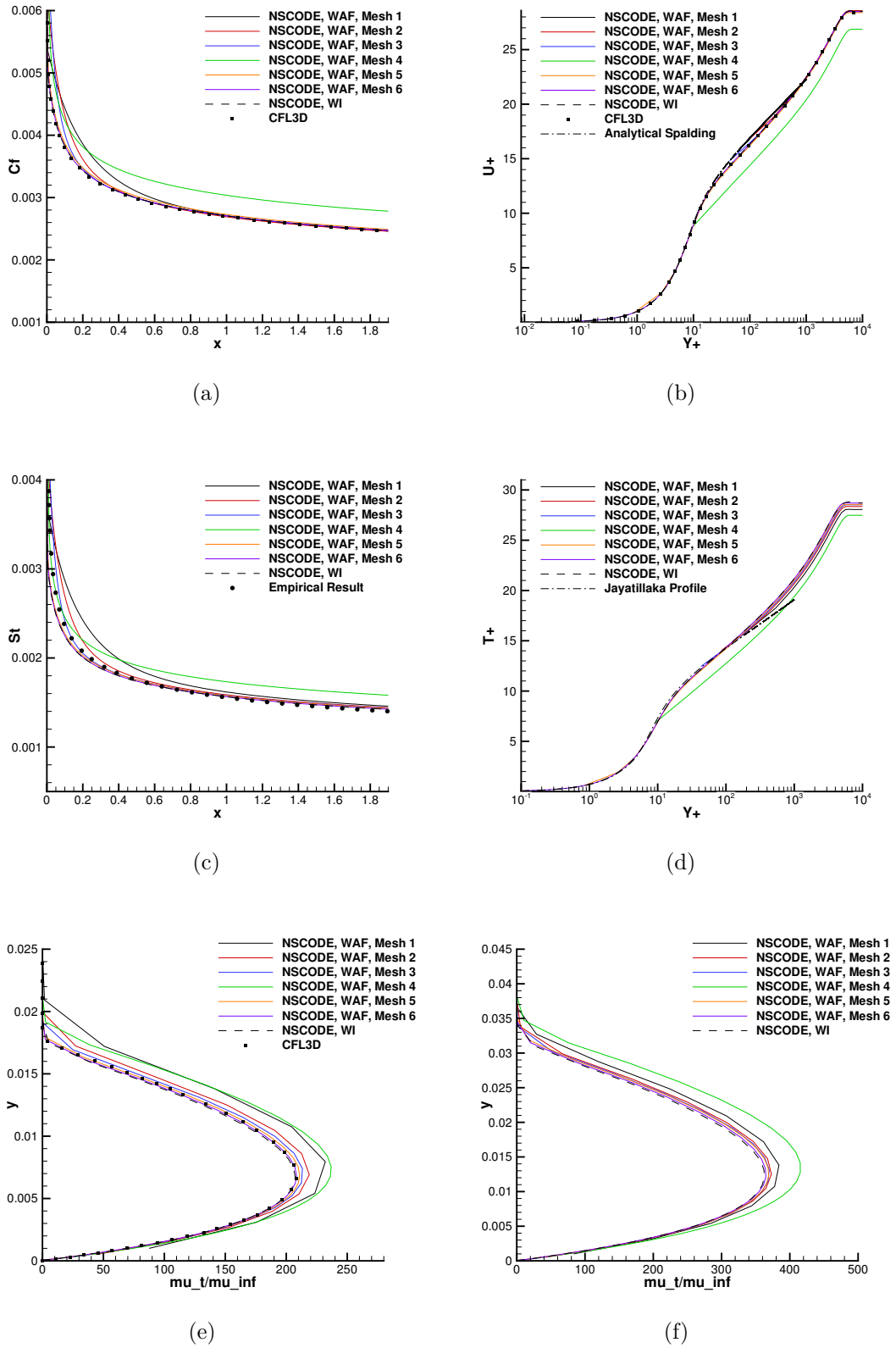

Figure 4.4 a) C_f distribution, b) velocity profile at $x = 1.9$ m, c) St distribution, d) temperature profile at $x = 1.9$ m. μ_t^+ distribution at e) $x = 0.97$ m and f) $x = 1.9$ m obtained using Spalart-Allmaras turbulence model

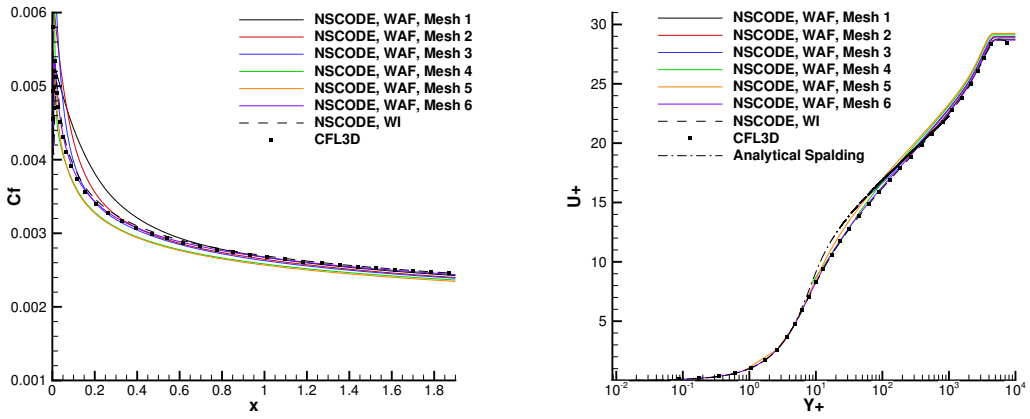

(a)

(b)

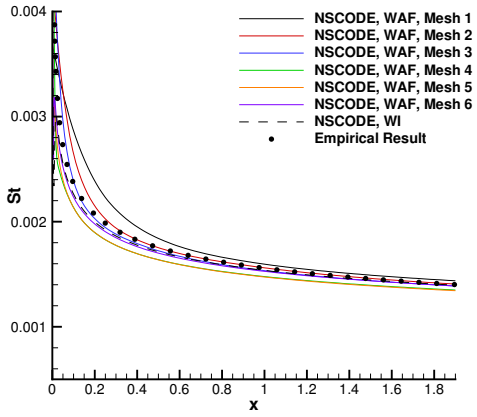

(c)

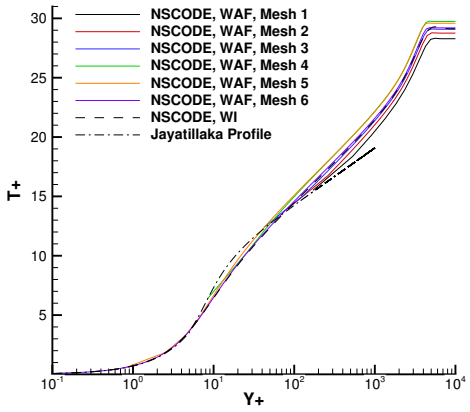

(d)

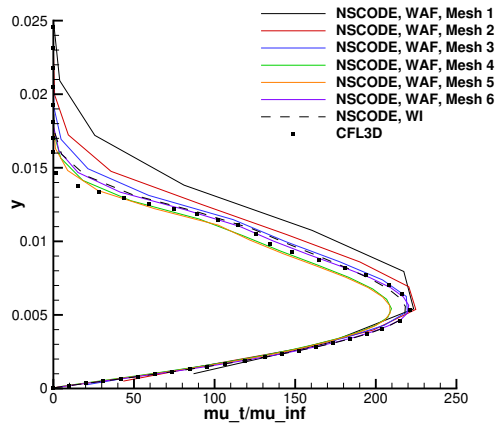

(e)

Figure 4.5 a) C_f distribution, b) velocity profile at $x = 1.9$ m, c) St distribution, d) temperature profile at $x = 1.9$ m, e) μ_t^+ distribution at $x = 0.97$ m obtained using $k - \omega$ SST turbulence model

Test case: NACA 0012 airfoil

Wall functions are tested with the NACA 0012 airfoil geometry and its validity in the presence of a curved profile and a pressure gradient is examined. Bradshaw and Huang (1995) remarked that the velocity law of the wall is less affected by a pressure gradient as compared to the temperature law of the wall. The array of meshes with different first cell heights that are tested is shown in Table 4.4. Unlike the case of a flat plate, the y^+ value changes considerably along the chord. The y^+ values at $x = 0.5$ m on the upper surface of the airfoil are used to distinguish between different wall spacing cases. The test case parameters are available from Center (2018) and shown in Table 4.5.

Table 4.4 First cell height for different meshes and the corresponding y^+ for NACA 0012 airfoil case

Mesh Name	**First cell height (m)**	y^+ at x = 0.5m
Mesh 1	1 x 10^{-3}	120
Mesh 2	8 x 10^{-4}	100
Mesh 3	5 x 10^{-4}	60
Mesh 4	1 x 10^{-4}	12
Mesh 5	1 x 10^{-5}	1
Mesh WI	1 x 10^{-7}	0.01

Table 4.5 Case parameters - NACA 0012 validation

Angle of Attack (°)	**Reynolds Number**	**Mach Number**
0°, 10°	6 E+06	0.15

The wall functions results are compared to that of low-Re turbulence model simulations and the CFL3D data available from Center (2018). For the Spalart-Allmaras turbulence model, Figure 4.6(a) and Figure 4.6(b) show that the C_f distribution is well predicted by wall functions for different meshes at both angles of attack. The prediction at the leading edge deviates from the low-Re turbulence model and CFL3D results because the assumption behind the wall function approach does not hold as a low local Reynolds number region exists at the leading edge of the airfoil. The prediction when the wall cell center is in the buffer layer shows similar behavior to a smooth flat plate result. Incidentally, the C_p distribution is unaffected by the first cell height and results are good at the leading edge as well. As the NASA Turbulence Modeling Resource does not provide the heat transfer data, the wall function heat transfer results are only compared to that from low-Re turbulence model simulations. From Figure 4.6(e) and Figure 4.6(f), it is observed that Stanton number predictions are also good for both angles of attack.

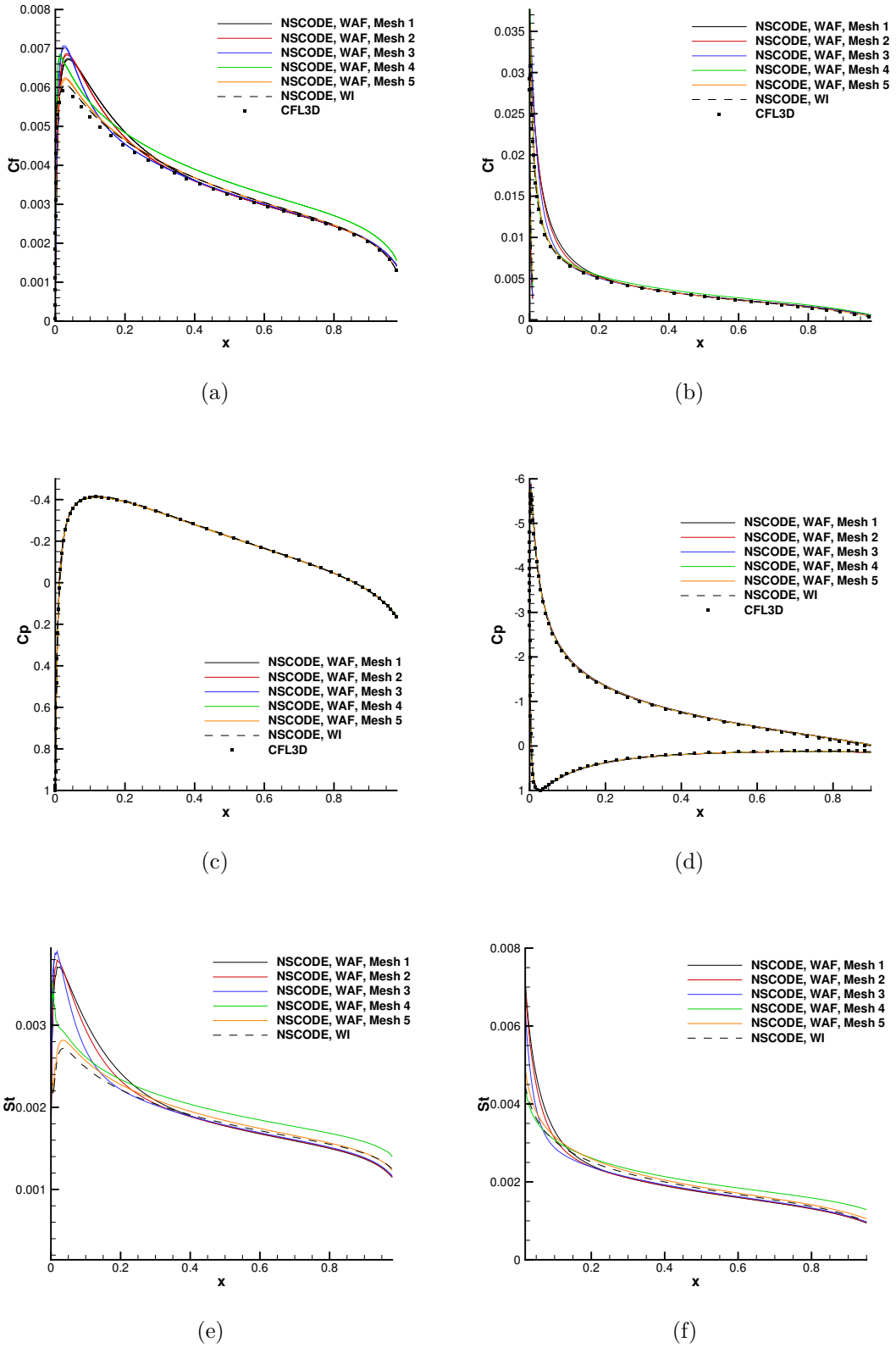

Figure 4.6 C_f distribution at AoA = a) 0° and b) 10°. C_p distribution at AoA = c) 0° and d) 10°. St distribution at AoA = e) 0° and f) 10° for Spalart-Allmaras turbulence model. The C_f and St results are for the upper surface of the airfoil

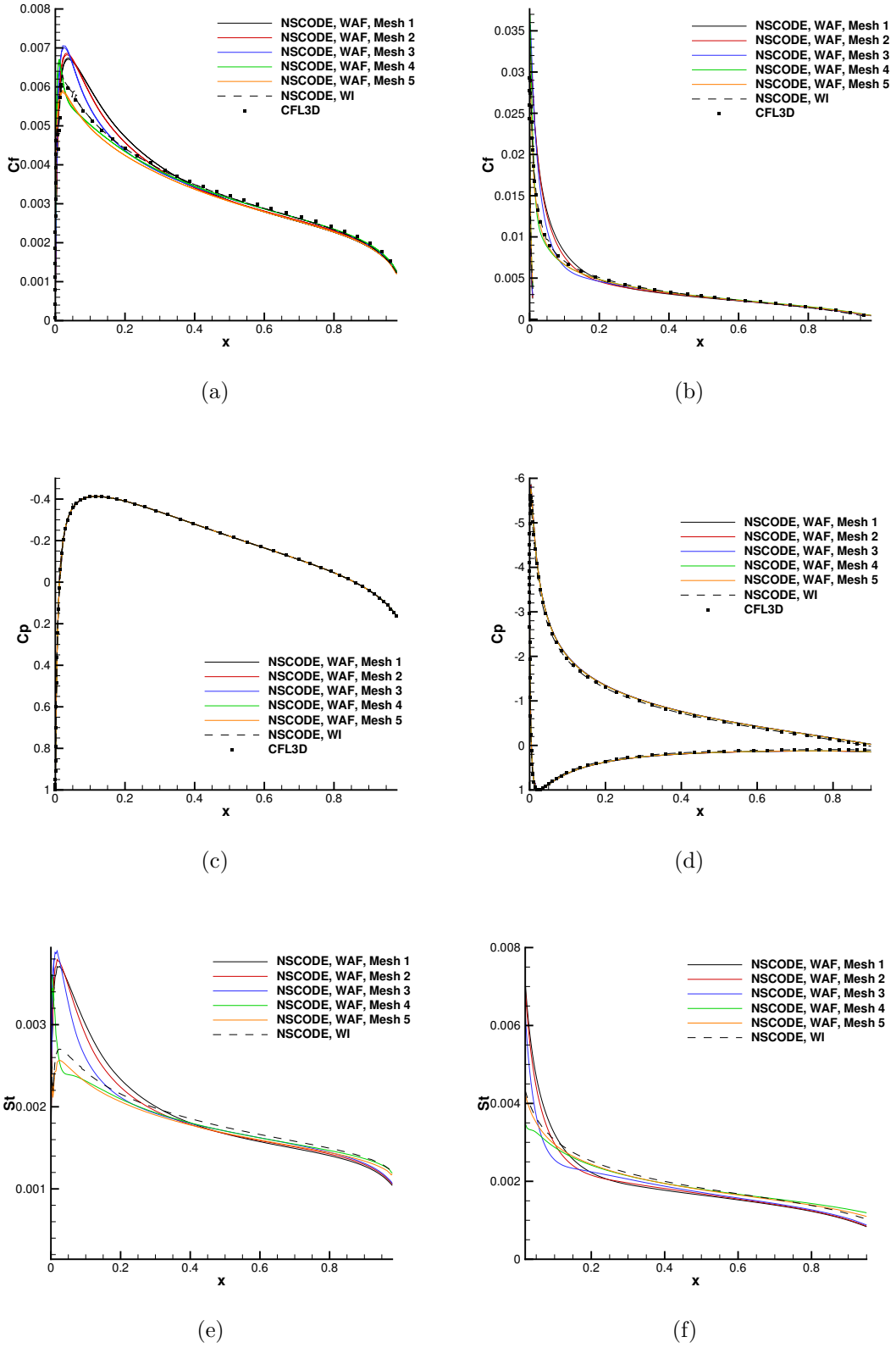

Figure 4.7 C_f distribution at AoA = a) 0°, b) 10°, C_p distribution at AoA = c) 0°, d) 10° and St distribution at AoA = e) 0°, f) 10° for k-ω SST turbulence model. The C_f and St results are for the upper surface of the airfoil

Similar results are also observed for $k-\omega$ SST turbulence model. Figure 4.7 indicates that the C_f and C_p distributions are in good agreement with those from the low-Re turbulence model simulation and CFL3D results. The Stanton number deviates more from the low-Re turbulence model result as compared to the results from the Spalart-Allmaras turbulence model. This pertains to the boundary conditions and the treatment of turbulence variables. Slightly better agreement is observed when the other boundary condition involving the modification of production term in the turbulence model is used. As described earlier, when extended for roughness effects, this boundary condition over-predicts the C_f and leads to stability issues at high values of k_s^+. Therefore, the boundary condition by Kalitzin et al. (2005) is used for all the simulations in the paper.

4.4.2 Rough walls

Wall functions are extended for application over rough surfaces. Extension of low-Re turbulence models for roughness is based on the assumption of the shift of the logarithmic region (Aupoix, 2007). This limits the application in the presence of a pressure gradient and in regions of a low local Reynolds number. Roughness extensions for the low-Reynolds number turbulence model approach are frequently validated within the assumption domain, however, they are used in industries for scenarios that are outside the assumption domain. The validation process for rough wall functions goes in hand with this approach. The low-Reynolds number $k-\omega$ SST turbulence model simulations on rough walls are carried out with the Aupoix-Cole roughness boundary condition.

Near-wall spacing dependence

Before the comparison with the semi-empirical and experimental results is made, it is important to quantify the dependence of rough wall functions on the near-wall spacing. As the inner region changes considerably in the presence of roughness, so does the near-wall characteristics of wall functions. To demonstrate this, the 2-D zero pressure gradient flat plate case with a domain similar to the one used for validation with the semi-empirical relation in Chapter 3 is taken. The values of k_s that are tested and the corresponding k_s^+ values are shown in Table 4.6. Rough BC 3 for $k-\omega$ SST turbulence model is used in the near-wall spacing dependence study.

Figure 4.8 depicts the near-wall spacing dependence of the wall function results for a rough wall case. Colebrook-Grigson roughness function is used for these simulations. Nikuradse roughness function gave similar but slightly offset results. The results show almost near-wall spacing independent behavior for the tested spectrum of y^+ in the fully rough regime.

Table 4.6 k_s^+ at $x = 1.5$ m for different values of k_s for the flat plate case

k_s (m)	2 x 10^{-3}	1 x 10^{-3}	5 x 10^{-4}	1 x 10^{-4}
k_s^+	535	250	115	20

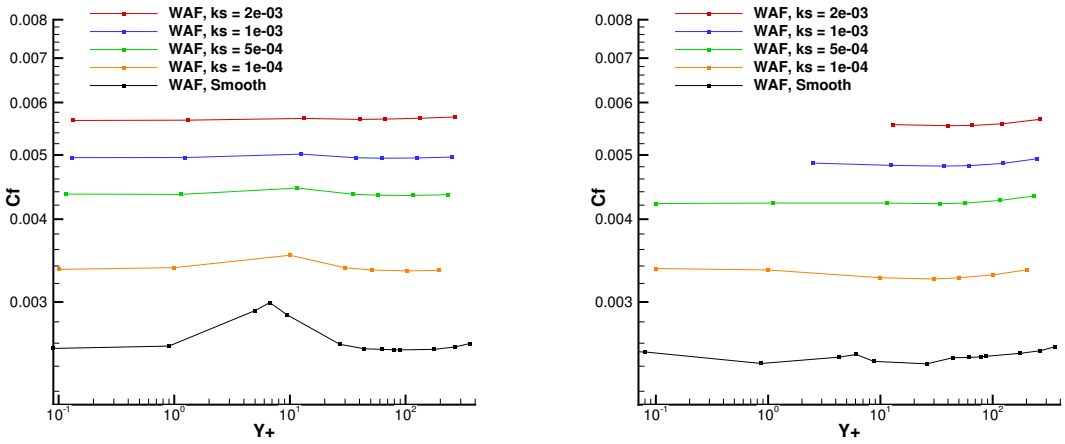

(a) (b)

Figure 4.8 C_f at $x = 1.5$ m for different values of y^+. a) Spalart-Allmaras and b) $k-\omega$ SST turbulence model

The restriction on the lower limit of y^+ for the implemented rough wall functions is more relaxed to the one posed by roughness extension proposed by Suga et al. (2006) for AWF. The numerical constraint on the lower limit of y^+ described by Suga is as follows,

$$y^+ \geq \frac{1}{2}\max\Big(0.06k_s^+, \min(k_s^+, y_v^+)\Big) \tag{4.28}$$

where $y_v^+ = 4.1$. The roughness implementation followed in this work does not pose such constraints, however, the use of lower values of y^+ at a high k_s^+ can cause convergence issues. Lack of detailed discussion on near-wall spacing dependence by Suga does not allow for an effective comparison between the models. Mesh dependence of wall functions was also tested by Eça and Hoekstra (2011). They used the roughness extension by Apsley (2007) and concluded that for $k_s^+ > 5$, the y^+ must be higher than the k_s^+ i.e. $k_s^+/y^+ < 1$ to avoid the under-prediction of C_f. Suga also recommended the use $k_s^+/y^+ < 1$ for accurate heat transfer results. The consistent nature of present wall functions overcomes these restrictions and provides accurate results for a much larger range of k_s^+/y^+. $k-\omega$ SST turbulence model shows more stability restrictions than the Spalart-Allmaras turbulence model. However, it is still better in comparison to those presented in the study by Eça and Hoekstra or the

one by Suga. For the Spalart-Allmaras turbulence model, the smooth result shows a peak which represents the wall function results in the buffer layer. The peak is smaller in $k-\omega$ SST turbulence model. In the transitionally rough regime ($k_s = 10^{-4}$), the size of the peak decreases. As the buffer layer still exists for this regime, this behavior is expected. The peak diminishes with the increase in k_s^+ and in the fully rough regime, it is almost non-existent. Thus, at high k_s, the results do not change considerably with the near-wall spacing. This also indicates that the implemented model behavior is physically sound. Having demonstrated the near-wall spacing behavior, mesh with $y^+ \approx 120$ is used for all further rough surface computations.

Test Case: Semi-empirical relation by Mills and Hang (1983)

The case parameters are same as the ones mentioned in Chapter 3. The k_s values tested are given in Table 4.6.

The C_f distributions obtained from the wall function approach are compared with that from low-Re turbulence model simulations and semi-empirical relation by Mills and Hang (1983). The results for the Spalart-Allmaras turbulence model are shown in Figure 4.9. The velocity profiles are also compared to those obtained from low-Re turbulence model simulations. It is observed that for the fully rough regime i.e. $k_s^+ > 70$, the C_f distribution and velocity profile for both the roughness functions are similar. The slopes of $k_s^+ - \Delta u^+$ curve for both the roughness functions are not the same. Therefore, at very high k_s^+ ($k_s^+ > 5000$), the results can be slightly different. Such high values of k_s^+ are not explored in this validation case. For a fully rough surface, C_f variation obtained from wall functions matches closely with that from the low-Re turbulence model approach and the semi-empirical relation by Mills and Hang. The lowest value of tested k_s^+ lies in the transitionally rough regime. Note that the result obtained from the relation by Mills and Hang (1983) for $k_s^+ = 20$ is shown only to maintain the completeness of the figure. As described earlier, the results from the semi-empirical relation are not true for the transitionally rough regime. The shift of the velocity profile in the transitionally rough regime estimated by the two roughness functions is different. This is reflected in the velocity profile as well. In this case, results from the Nikuradse roughness function match well with that of low-Re turbulence model results. The Boeing roughness extension is used in the low-Re turbulence model simulations. As the roughness function for the low-Re turbulence model extension is not exactly the same as the Nikuradse roughness function in the transitionally rough regime, the difference in results is expected. Another reason for this deviation is the underlying assumption behind the consistent wall-function approach. Therefore, the accuracy of the approach in the transitionally rough regime is

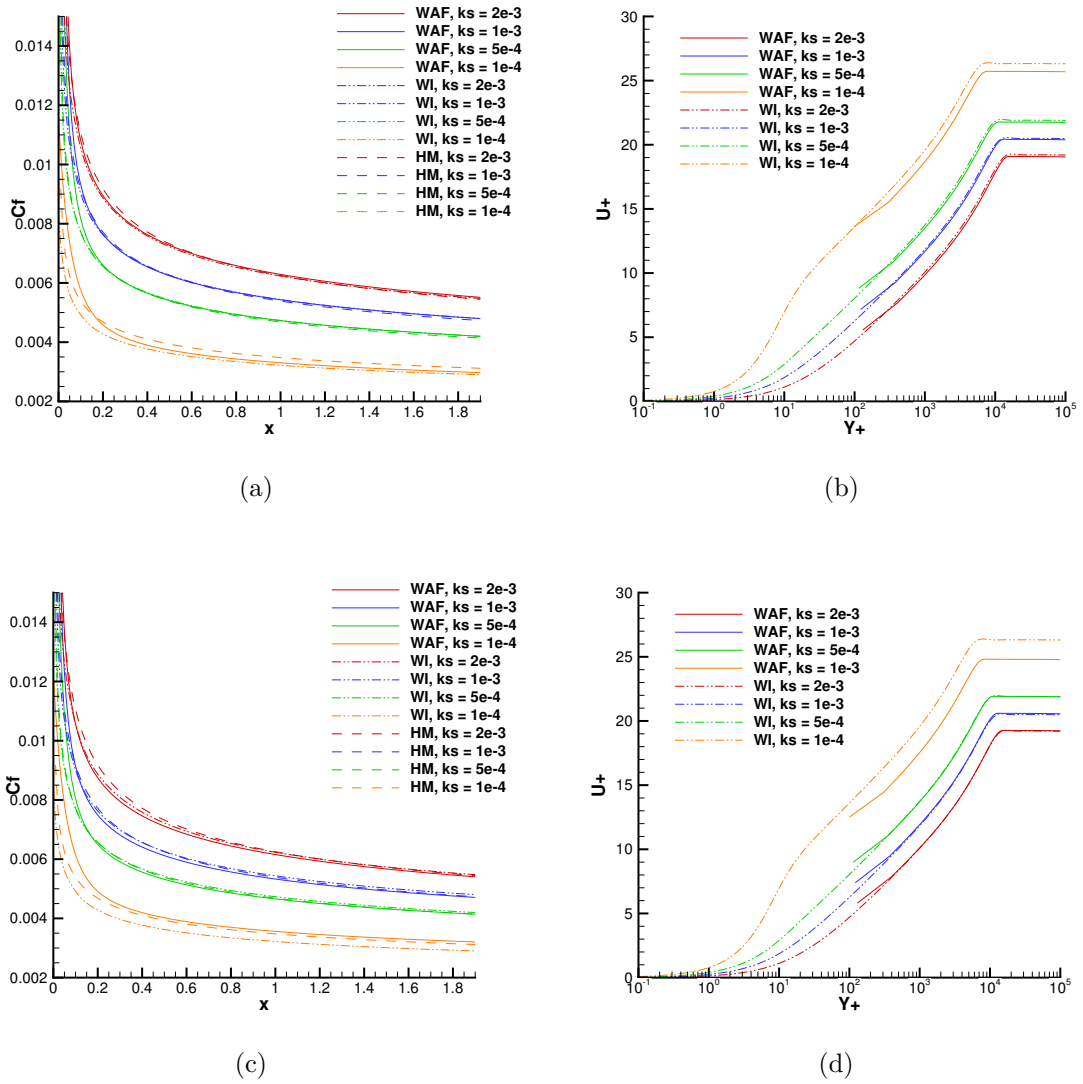

Figure 4.9 a) C_f variation and b) velocity profile for Nikuradse roughness function. c) C_f variation and d) velocity profile for Colebrook-Grigson roughness function

questionable.

As described earlier, the extension of wall functions for rough surfaces in the case of the $k-\omega$ SST turbulence model can be used with any of the three boundary conditions shown in Eq. (4.24) - Eq. (4.26). The results from the three boundary conditions for different values of k_s are shown in Figure 4.10 - Figure 4.12. From Figure 4.10, it is observed that for Rough BC 1 both the Nikuradse and Colebrook-Grigson roughness functions slightly underestimates C_f distributions. Nikuradse roughness function gives a slightly better agreement with those from the semi-empirical relation at high values of k_s^+ as compared to Colebrook-Grigson roughness function. The results remain close to semi-empirical results at lower values of k_s in comparison to low-Re turbulence model results. Figure 4.11 shows that Rough BC 2 with Nikuradse roughness function leads to little over-prediction of C_f at high values of k_s^+. On the other hand, Colebrook-Grigson roughness function gives good agreement at each k_s^+ value. Figure 4.12 shows that for Nikuradse roughness correction, the results match very well with that of semi-empirical relation at high values of k_s^+. For k_s^+ value in the transitionally rough regime, the results tend to those obtained using the Spalart-Allmaras turbulence model.

Rough BC 1 results are not significantly different from those obtained using Rough BC 2 and Rough BC 3, however, the latter two gives better predictions. The Rough BC 2 and Rough BC 3 leads to almost similar results with both of them better matching well with semi-empirical results for Colebrook-Grigson and Nikuradse roughness functions respectively. From the above discussion, it can be concluded that it is important to maintain consistency between ω^+, k^+ and ν_t^+ as it leads to better predictions. The decision of choosing between either of the two roughness function is subject to the type of roughness. The difference in results is significant only in the transitionally rough regime. As described earlier, the Nikuradse roughness function with $\kappa = 0.41$ should resemble the semi-empirical results. Therefore, Rough BC 3 is used for simulations carried out with $k-\omega$ SST turbulence model. When Nikuradse roughness function is used with $\kappa = 0.4$, it leads to results that are similar to those obtained from low-Re turbulence model simulations using the Aupoix-Niku extension. For brevity, these results are not shown here.

Test case: Low-Re turbulence model simulations, Rough NACA 0012

There is a lack of good quality data for the skin-friction coefficient distribution on an airfoil with rough surfaces. Most of the data is restricted to the effect of roughness on the coefficient of drag and lift. This data is useful for studying the aggregate effect of roughness. However, in many applications such as ice shape prediction, the local St distribution is important. Poinsatte et al. (1991) provides C_f and St distribution near the leading edge on the airfoil,

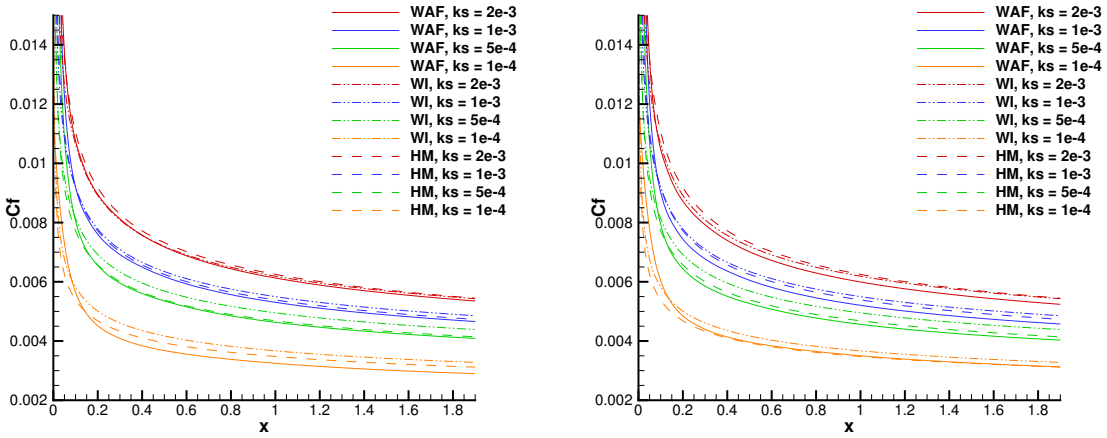

(a) (b)

Figure 4.10 C_f variation for a) Nikuradse and b) Colebrook-Grigson roughness function with Rough BC 1 for $k-\omega$ SST turbulence model

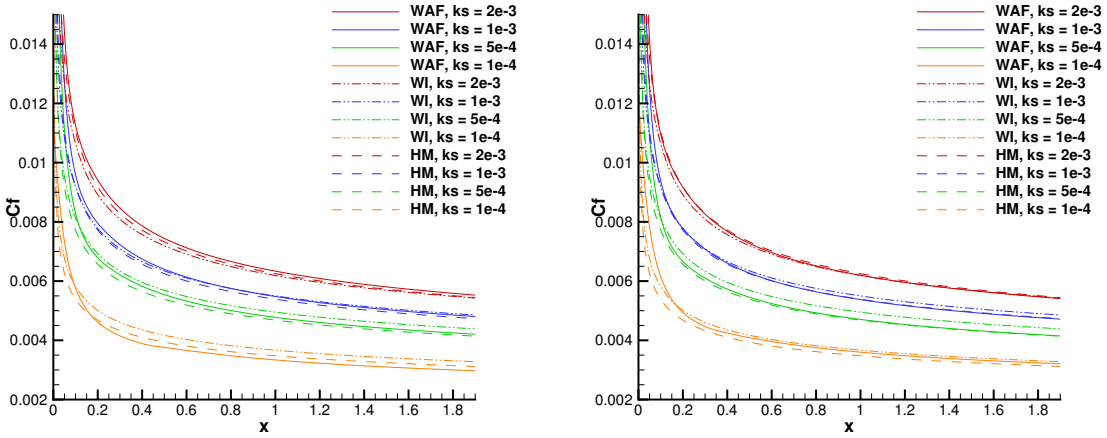

(a) (b)

Figure 4.11 C_f variation for a) Nikuradse and b) Colebrook-Grigson roughness function with Rough BC 2 for $k-\omega$ SST turbulence model

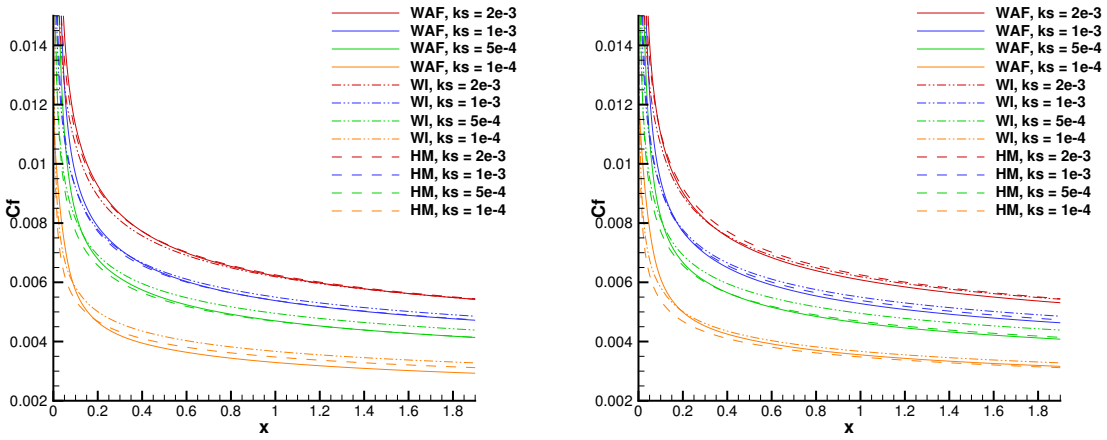

(a) (b)

Figure 4.12 C_f variation for a) Nikuradse and b) Colebrook-Grigson roughness function with Rough BC 3 for $k-\omega$ SST turbulence model

however, it is restricted to lower roughness heights and show some unexpected behavior which is hard to physically justify. With the dearth of data, data from low-Re turbulence model simulations are relied upon to validate the wall function approach for a rough surface over an airfoil. The St distribution is validated using the Reynolds analogy. NACA 0012 airfoil at a 0° angle of attack with case parameters same as the smooth wall case is considered for validation. The tested roughness values are highlighted in Table 4.7.

Table 4.7 k_s^+ at $x = 0.5$ m for different values of k_s for the NACA 0012 airfoil case

k_s (m)	0.005	0.002	0.001	0.0005
k_s^+	1910	700	330	155

The results for the Spalart-Allmaras turbulence model are shown in Figure 4.13. These roughness values lie in the fully rough regime. The C_f predictions by wall functions match closely with the low-Re turbulence model results except at the leading edge. Note that the leading edge prediction for a rough surface by the low-Re turbulence model approach cannot be said to be accurate because the roughness extension is based on the shift of the logarithmic velocity profile and the logarithmic velocity profile does not hold at the low local Reynolds number region at the leading edge. Also, the roughness extension does not account for the pressure gradient which is of considerable magnitude at the leading edge. These limitations were highlighted by Aupoix (2007). In this situation, it can be said that the wall function approach performs well for the NACA 0012 case as well. The St predictions by

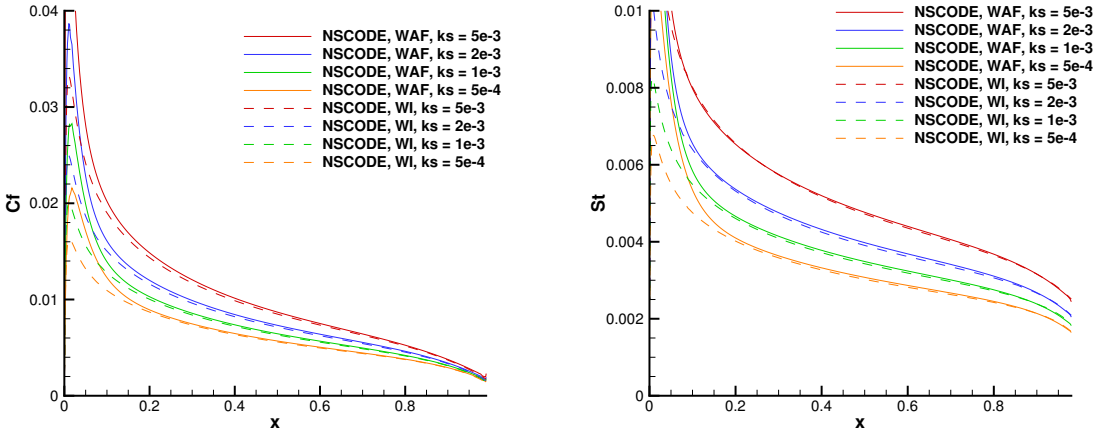

(a) (b)

Figure 4.13 a) C_f and b) St variation for rough NACA 0012 using Reynolds Analogy for Spalart-Allmaras turbulence model

wall functions are also in close agreement with the corresponding results obtained using the low-Re turbulence model approach for all the tested values of roughness.

Figure 4.14 shows the result for the $k-\omega$ SST turbulence model. It is observed that wall function results agree well with those from low-Re turbulence model simulations. The agreement in heat transfer results is not as good as the Spalart-Allmaras turbulence model results. This behavior is also observed for the smooth NACA 0012 case in Figure 4.7(e) and is linked to the selection of the boundary condition. Nevertheless, the result shows that wall functions can be effectively used to simulate the flow over rough surfaces.

Test Case: Experiments by Hosni et al. (1991)

The parameters used for simulating this experimental case by Hosni et al. (1991) are given in Chapter 3. The value of k_s in Chapter 3 is taken to be the same as the one used by Aupoix for validation for ensuring an effective comparison with the numerical results by Aupoix. The k_s used in this chapter is slightly different (shown in Table 4.8). This is the experimental value of k_s and it ensures a more consistent analysis. Nikuradse roughness function is used for this experimental case.

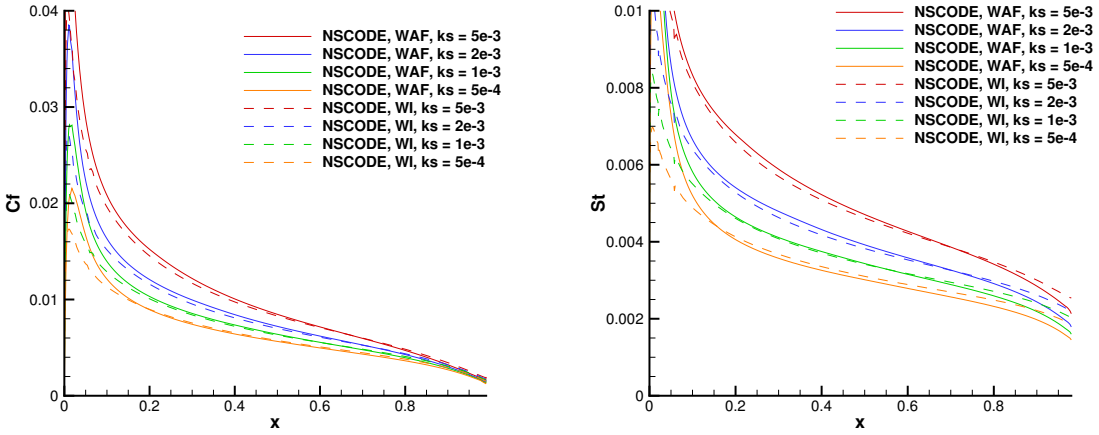

(a) (b)

Figure 4.14 a) C_f and b) St variation for rough NACA 0012 using Reynolds Analogy for $k-\omega$ SST turbulence model

Table 4.8 Roughness parameters for experiments by Hosni et al. (1993)

Element Type	k_s (mm)	h (mm)	S_{corr}
Cone	1.16	0.635	1.09
Hemisphere	1.16	0.635	1.17

The case with $l/d = 2$ leads to the fully rough regime with $k_s^+ \approx 200$. The results obtained using the Spalart-Allmaras turbulence model are shown in Figure 4.15. It is observed that C_f predictions using wall functions are in good agreement with the experimental results and the low-Re turbulence model results. The Stanton number predictions depend on the temperature correction term. It is observed that the use of Reynolds analogy leads to an overprediction in the Stanton number prediction for both wall function and low-Re turbulence model approaches. This was also highlighted by Aupoix and Spalart (2003). When the Reynolds analogy is used, the wall function results match with the low-Re turbulence model results. The use of the correction term by Aupoix (2015) gives the closest prediction to the experimental results. The result obtained using the correction term by Dipprey and Sabersky (1963) is close to that of the Aupoix correction term. The correction term by Owen and Thomson (1963) underpredicts the Stanton number. For the $k-\omega$ SST turbulence model, the results are shown in Figure 4.16. The results are very similar to those obtained for the Spalart-Allmaras turbulence model.

Hosni et al. (1993) obtained the Stanton number distribution for a flat plate covered with conical roughness elements. They selected a 40° half apex angle truncated cone as the

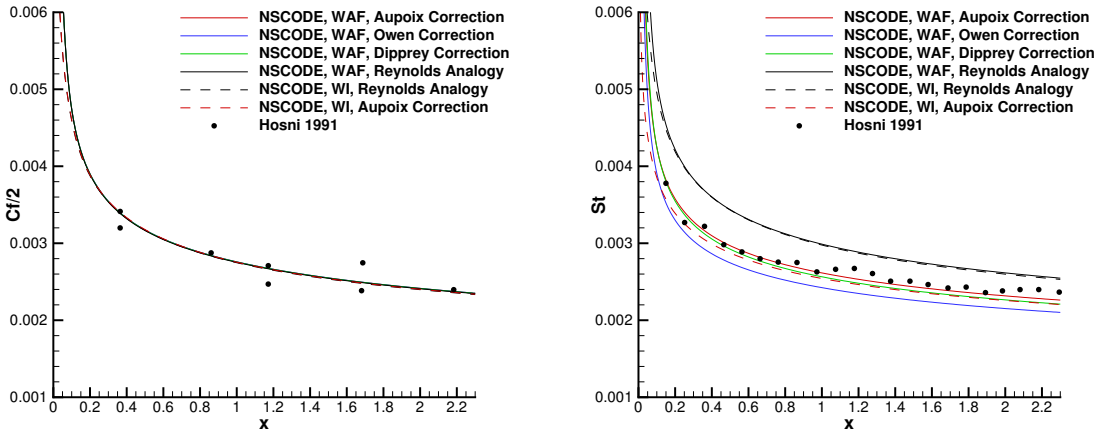

(a) (b)

Figure 4.15 a) C_f and b) St variation for hemispherical elements with spacing of $l/d = 2$ using Spalart-Allmaras turbulence model

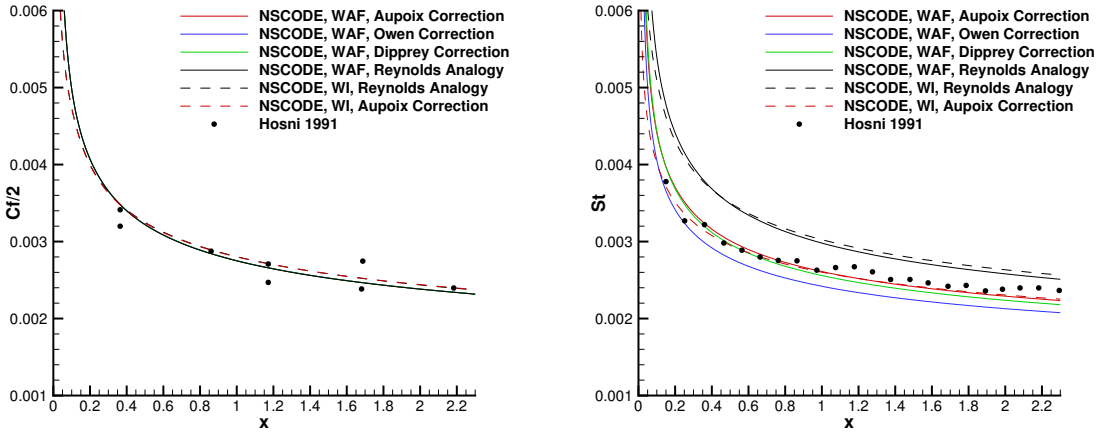

(a) (b)

Figure 4.16 a) C_f and b) St variation for hemispherical elements with spacing of $l/d = 2$ using $k - \omega$ SST turbulence model

roughness element shape. The cone shape was selected to give a similar value of skin-friction coefficient as the hemispherical elements. They observed that even though the C_f remains the same, the shape of the roughness element affects the Stanton number. The wall function and low-Re turbulence model approaches with different thermal corrections are validated with these experimental observations. The values of roughness parameters are given in Table 4.8. The value of h and S_{corr} are obtained from Chedevergne (2018). Chedevergne determined the k_s value from the relation by Waigh and Kind (1998). However, in order to be consistent with the experimental results, the value of k_s is selected to be the experimental value.

Figure 4.17 shows results for the two turbulence models, and these results are quite similar. The results obtained using wall function approach with Aupoix thermal correction agree well with corresponding low-Re turbulence model simulation results. The cause of the slight difference between the two results is discussed in the next validation case as it encompasses the complete range of h, S_{corr} and k_s. In general, the Aupoix correction improves the prediction and both wall function and low-Re turbulence model simulations are in good agreement with the experimental results. The correction term by Dipprey results in St variation that is close to the experimental hemispherical roughness results. On the other hand, the correction term by Owen leads to results that match well with the conical roughness elements.

Even though Owen and Dipprey corrections improve results in the presence of rough walls, these models cannot distinguish between the shape of roughness elements as they rely on a single roughness scale. Therefore, both corrections are insufficient to capture the physics behind the heat transfer in the presence of rough surfaces. The correction term by Aupoix uses an additional physical parameter S_{corr} to account for the shape of the element. This is an important observation as it demonstrates the inadequacy of a single roughness scale for modeling both the skin-friction coefficient and heat transfer.

Test case: Experiments by Dukhan et al. (1999)

Experimental Stanton number for the stochastically distributed ice-roughness was provided by Dukhan et al. (1999). Unfortunately, the study lacks the skin-friction coefficient measurements. However, it still provides useful insight into how the shape and distribution of ice shape affect the heat transfer over the surface. This information is particularly useful for ice-shape prediction codes. From the results obtained for 7 different types of ice surfaces, they determined the expression of St relating to a local Reynolds number and a parameter which determines the ice-shape roughness characteristics. Wall function and low-Re turbulence model approaches are tested for St distributions against the experimental results obtained at a velocity of 47.2 m/s. For the higher values of k_s (i.e. for Case 3 and 4),

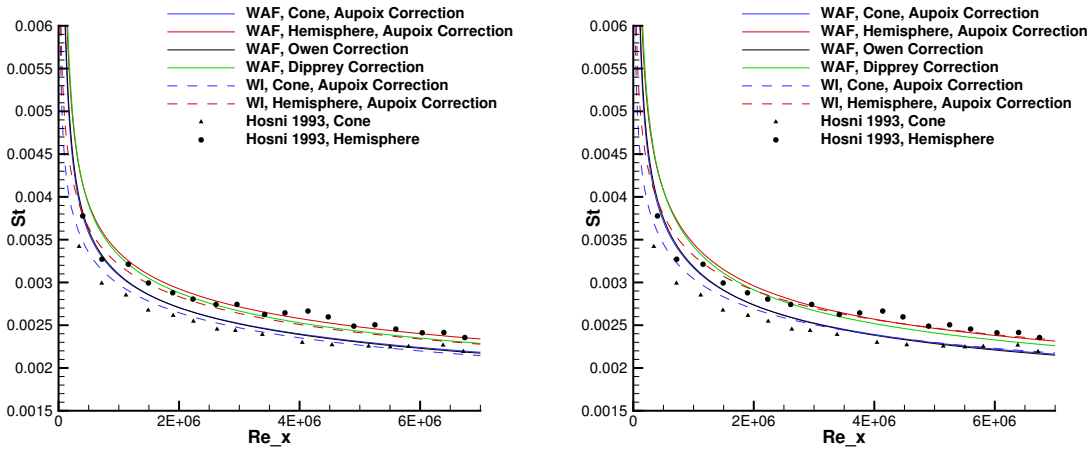

(a) (b)

Figure 4.17 a) Spalart-Allmaras and b) $k-\omega$ SST turbulent model results comparing the effect of roughness shape on St

Nikuradse roughness function when used with Spalding velocity profile shows problems with convergence. Therefore, Colebrook-Grigson roughness function is used instead. As shown earlier, the difference in results between the two roughness functions is minimal.

The roughness parameters for the different cases are shown in Table 4.9. All the cases are tested to demonstrate the effect of different thermal correction terms using the wall function approach. The results for the Spalart-Allmaras turbulence model is shown in Figures 4.18 - 4.24. The figures are similarly scaled to the results presented by Radenac et al. (2018) for facilitating the comparison. For most of the cases, the C_f prediction by wall function matches well with that from low-Re turbulence model simulations. The exception being Case 5 and Case 6, both of which are in transitionally rough regime. As the roughness extension relies on the assumption of the fully rough regime, the deviation in the transitionally rough

Table 4.9 Roughness parameters for test cases by Dukhan. (Reproduced from Radenac et al., 2018)

Case	Ice-shape type	k_s (mm)	S_{corr}	$\alpha' = k/k_s$	Roughness Regime
Case 1	Closely-spaced rough glaze	2.51	1.22	0.749	Fully rough
Case 2	Loosely-spaced rough glaze	2.94	1.18	0.946	Fully rough
Case 3	Intermediately-spaced rough glaze	15.63	1.22	0.1964	Fully rough
Case 4	Rime feathers	23.04	1.22	0.1875	Fully rough
Case 5	Closely-spaced smooth rime	0.14	1.13	3.428	Transitional
Case 6	Smooth glaze	0.04	1.06	10.25	Mixed smooth-transitional
Case 7	Smooth rime	2.25	1.08	0.4844	Fully rough

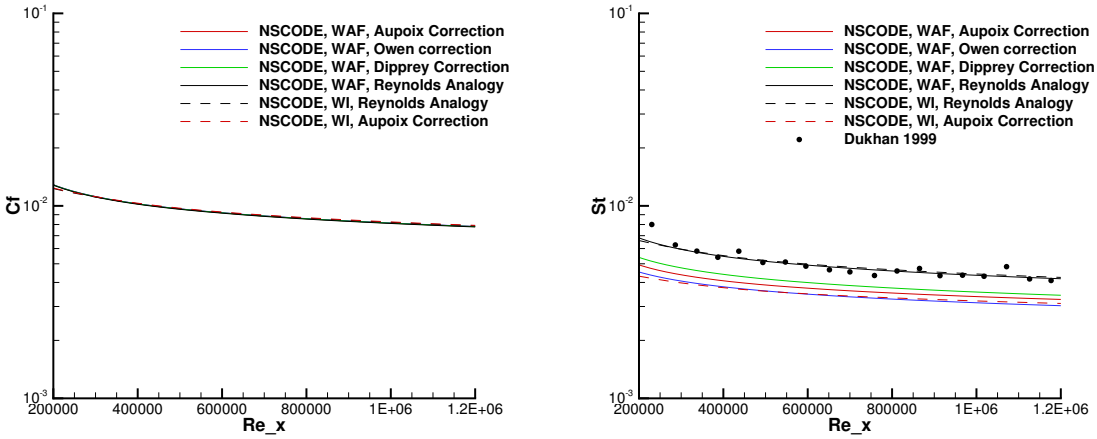

(a) (b)

Figure 4.18 a) C_f and b) St variation for Dukhan Case 1 using Spalart-Allmaras turbulence model

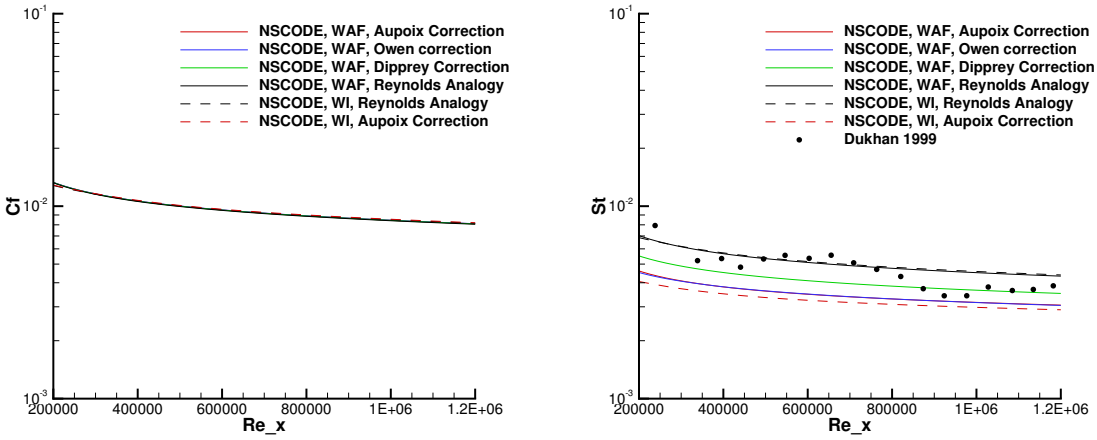

(a) (b)

Figure 4.19 a) C_f and b) St variation for Dukhan Case 2 using Spalart-Allmaras turbulence model

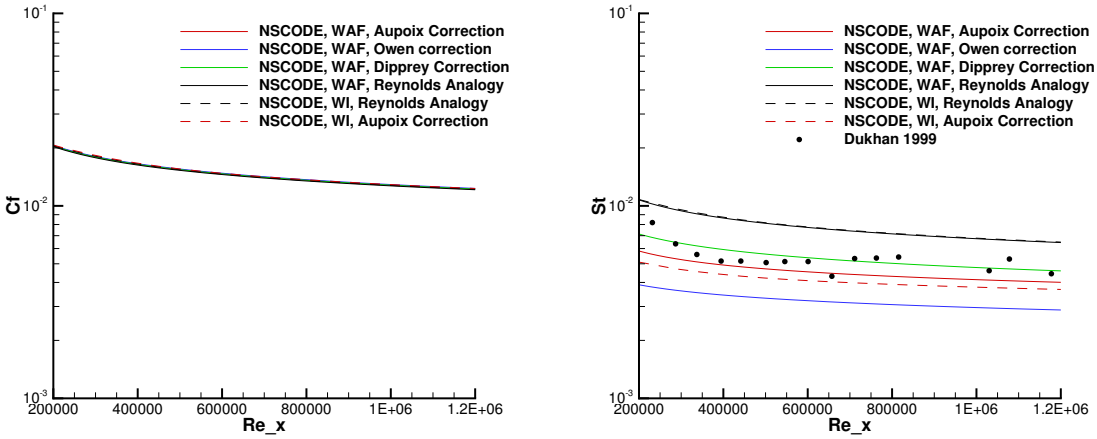

(a) (b)

Figure 4.20 a) C_f and b) St variation for Dukhan Case 3 using Spalart-Allmaras turbulence model

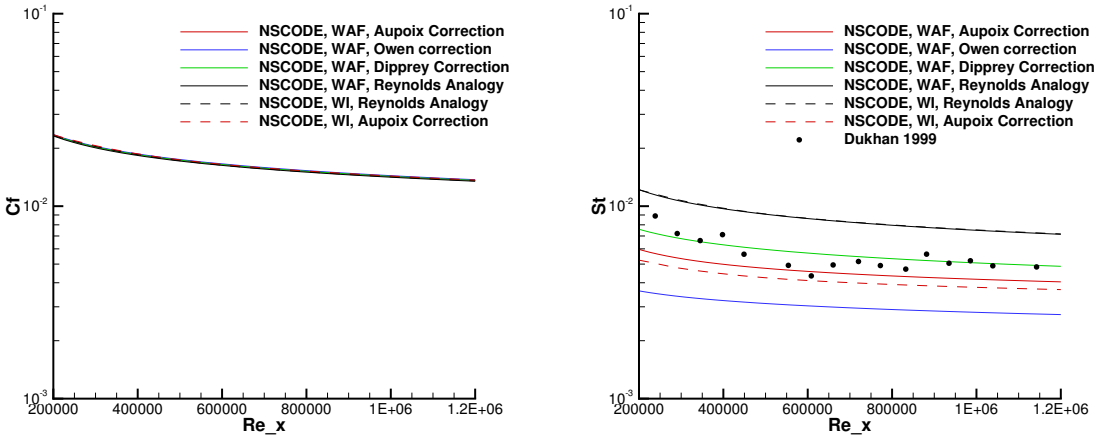

(a) (b)

Figure 4.21 a) C_f and b) St variation for Dukhan Case 4 using Spalart-Allmaras turbulence model

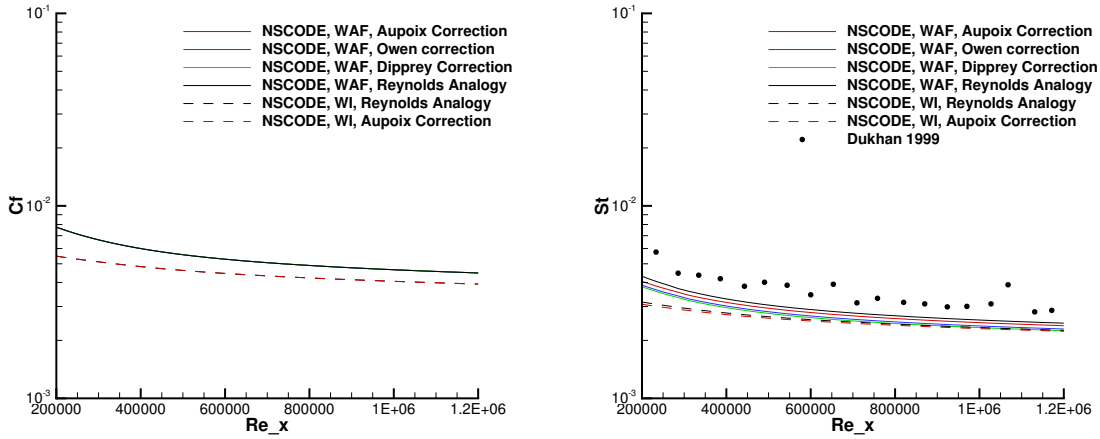

(a) (b)

Figure 4.22 a) C_f and b) St variation for Dukhan Case 5 using Spalart-Allmaras turbulence model

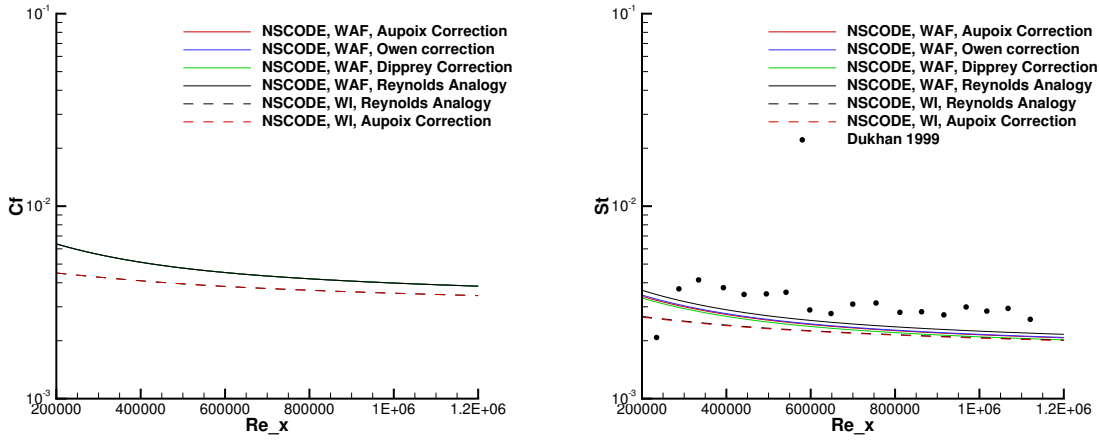

(a) (b)

Figure 4.23 a) C_f and b) St variation for Dukhan Case 6 using Spalart-Allmaras turbulence model

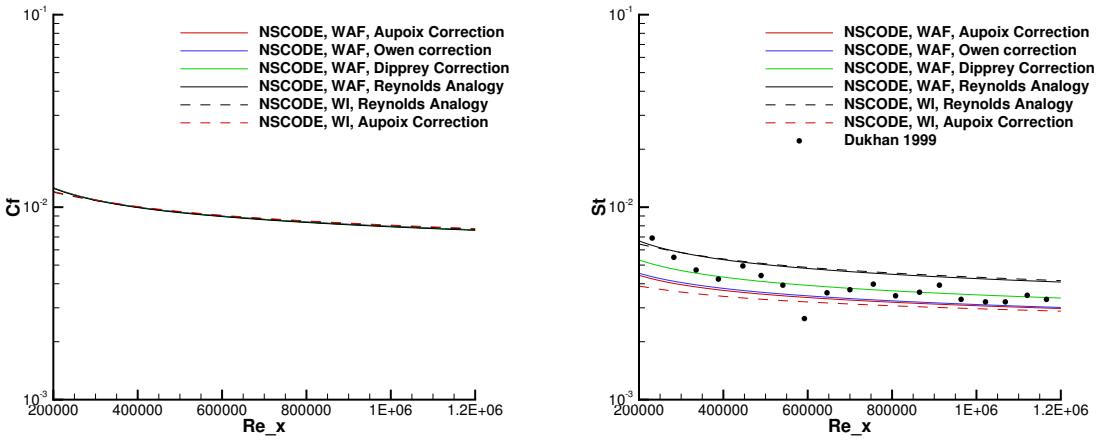

(a) (b)

Figure 4.24 a) C_f and b) St variation for Dukhan Case 7 using Spalart-Allmaras turbulence model

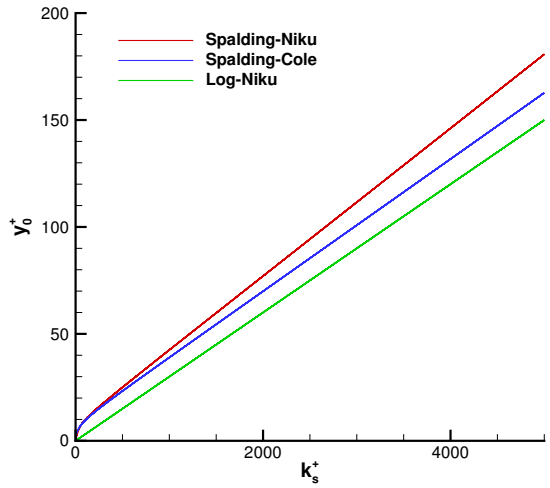

Figure 4.25 Comparison of different analytic expressions of y_0^+

regime is expected.

Note that the St variation obtained using the wall function approach with the Reynolds Analogy assumption matches well with that of the low-Re turbulence model approach for all the fully rough cases. At higher values of k_s an offset between the Aupoix correction results obtained with and without wall functions is observed. Similar behavior was also observed in the IBL simulations by Radenac et al. (2018). As the Aupoix correction in the wall function approach follows a similar formulation, the behavior is expected. It may be due to different treatments of y_0^+ in wall function and low-Re turbulence model approaches. This results in slightly different y_0^+ profiles as a function of k_s^+. The y_0^+ obtained using the Spalding profile with Nikuradse and Colebrook roughness functions are compared with $y_0^+ = 0.03k_s^+$ which is based on fully rough assumption. These are referred to as Spalding-Niku, Spalding-Cole and Log-Niku analytic functions respectively and shown in Figure 4.25. The difference between the profiles increase with the k_s^+ and can result in the difference between wall function and low-Re turbulence model results. This indicates the results are slightly sensitive to the selection of y_0^+. For the wall function approach, y_0^+ is determined from the Colebrook roughness function using Spalding profile to maintain consistency with the turbulence model and reduce the mesh dependence of the results. Nevertheless, the St distribution still lies within the experimental result envelope.

The St variation provides some exciting results. For Case 1, the St distribution is surprising as the Reynolds Analogy gives the best result. This might be due to the uncertainty in the estimation of k_s. In Cases 2, 3 and 4, the correction term by Dipprey provides the best agreement to the experimental heat transfer results. The correction by Aupoix slightly underpredicts St for these cases. Owen correction underestimates St to a large extent in Cases 3 and 4. For Cases 5 and 6, all three roughness corrections behave similarly and underpredict St. In Case 7, all three roughness corrections give descent predictions.

The results for $k - \omega$ SST model are shown in Figure 4.26 - Figure 4.32. No significant differences are observed in comparison to the Spalart-Allmaras turbulence model results. The results for both turbulence models match well for both C_f and St distributions with CLICET simulation results (using $k - \omega$ SST turbulence model as well) shown by Radenac et al. (2018) for all the cases. For clarity, the comparison is not shown here. Comparing the different thermal correction terms for various experimental cases, it can be concluded that each of them gives good results in some or other case and the selection depends on the type and distribution of roughness.

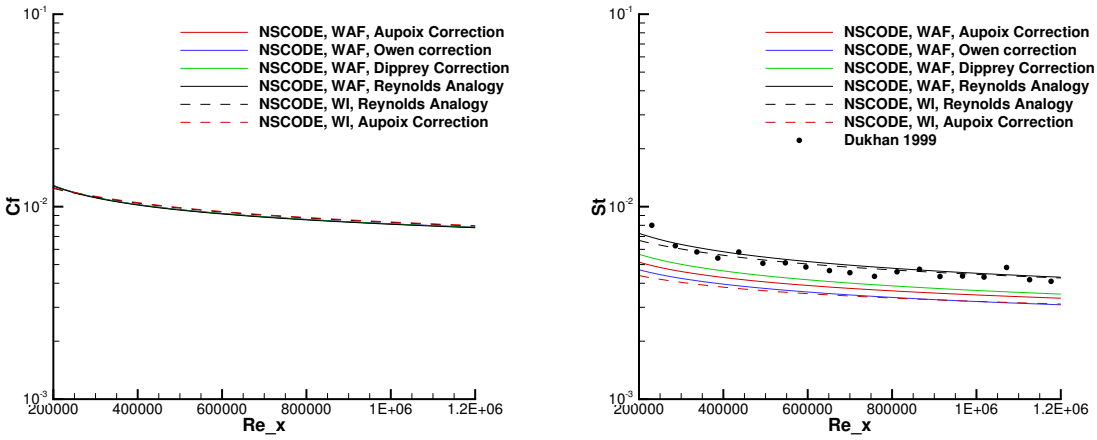

(a) (b)

Figure 4.26 a) C_f and b) St variation for Dukhan Case 1 using $k-\omega$ SST turbulence model

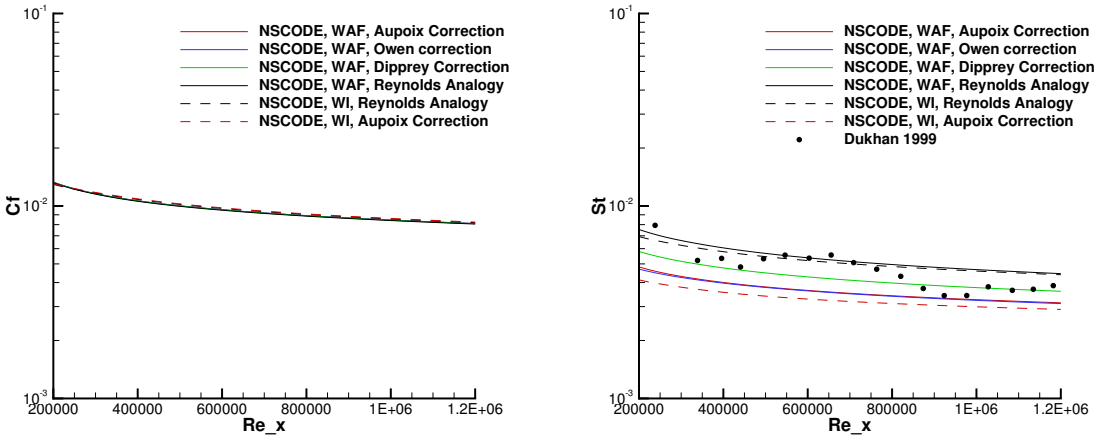

(a) (b)

Figure 4.27 a) C_f and b) St variation for Dukhan Case 2 using $k-\omega$ SST turbulence model

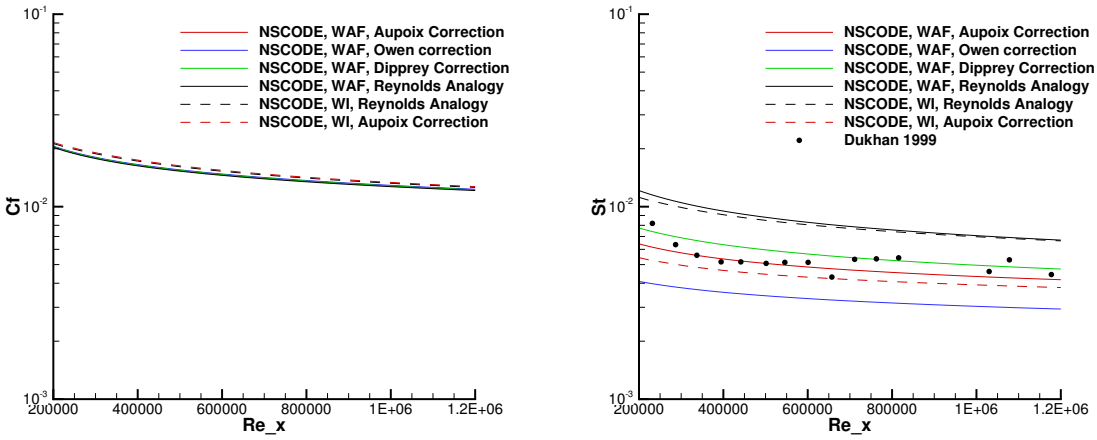

(a) (b)

Figure 4.28 a) C_f and b) St variation for Dukhan Case 3 using $k-\omega$ SST turbulence model

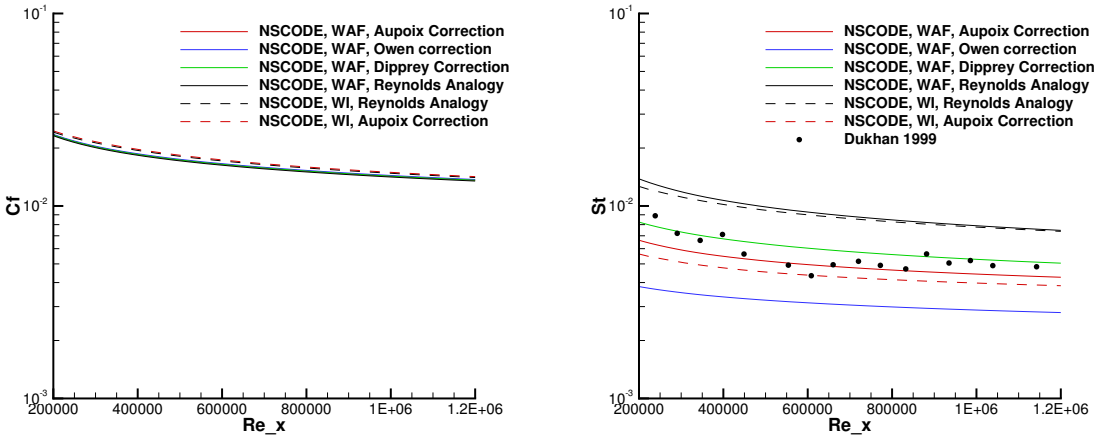

(a) (b)

Figure 4.29 a) C_f and b) St variation for Dukhan Case 4 using $k-\omega$ SST turbulence model

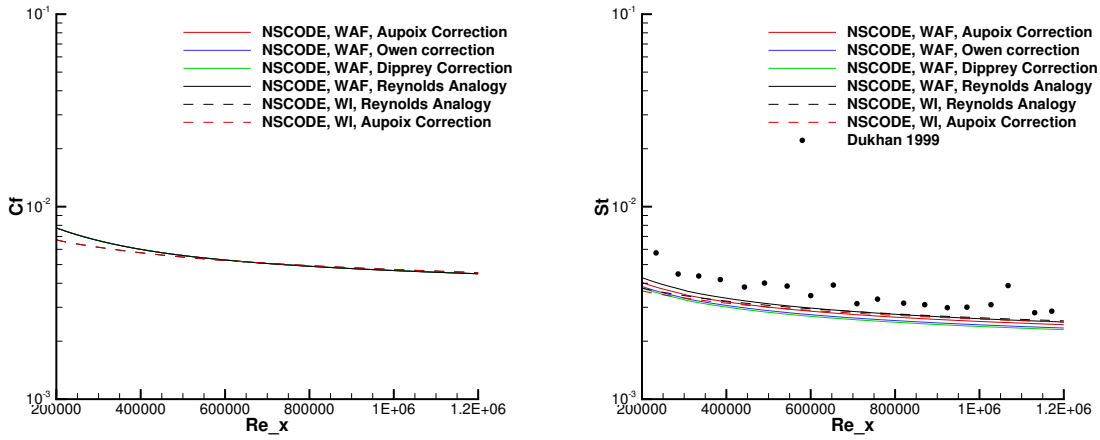

(a) (b)

Figure 4.30 a) C_f and b) St variation for Dukhan Case 5 using $k-\omega$ SST turbulence model

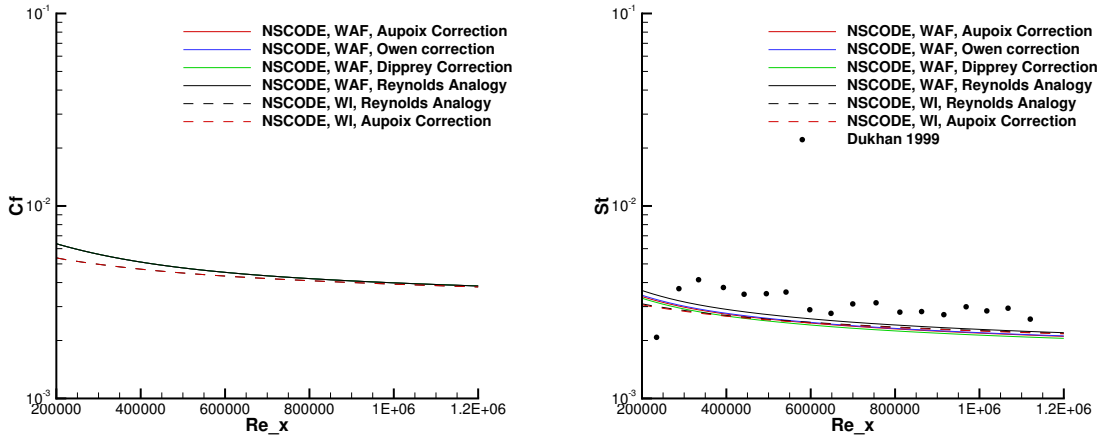

(a) (b)

Figure 4.31 a) C_f and b) St variation for Dukhan Case 6 using $k-\omega$ SST turbulence model

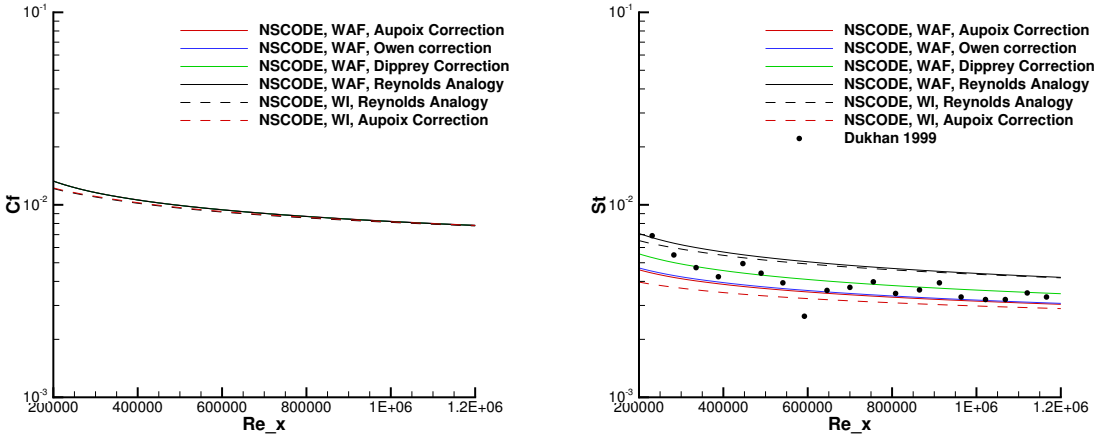

(a) (b)

Figure 4.32 a) C_f and b) St variation for Dukhan Case 7 using $k-\omega$ SST turbulence model

CHAPTER 5 CONCLUSION

5.1 Synthesis of work

The thesis is focused on exploring different strategies to model heat transfer over rough surfaces. Both low-Reynolds and high-Reynolds turbulence model approaches are considered and analyzed to understand their advantages and disadvantages.

Different roughness extensions for Spalart-Allmaras and $k-\omega$ SST turbulence model are examined. Spalart-Allmaras turbulence model along with Boeing extension gives good predictions of the skin-friction coefficient for different experimental cases. Four roughness extensions for $k-\omega$ SST turbulence model are compared. Aupoix-Cole and Aupoix-Niku roughness extensions overcome the drawbacks of the other extensions, and the former gives the best predictions. The extensions are unable to predict the heat transfer over rough surfaces using the Reynolds analogy assumption as it is not valid in the presence of rough surfaces. In order to overcome this deficiency, thermal correction by Aupoix (2015) is implemented. The model ensures the consistency between the predictions of friction drag and heat transfer over rough surfaces, thereby giving much superior agreement with experimental results.

Log-law based wall functions are also implemented for both Spalart-Allmaras and $k-\omega$ SST turbulence models. They are validated with several academic cases. The wall function approach gives good skin-friction coefficient and Stanton number results for a wide range of near-wall spacing. The first cell center in the buffer layer leads to a slight deviation in results due to the non-linearity of turbulence and flow variables in that region.

The wall functions are extended to incorporate the effect of roughness. The wall function roughness extension is closely linked to the underlying low-Re turbulence model roughness extension. The near-wall spacing dependence of wall functions is explored for rough walls and is found to be physically consistent. The consistent nature of the roughness extension outperforms other rough wall functions available in the literature and exhibits relatively low near-wall spacing dependence. Two different roughness functions namely Nikuradse and Colebrook-Grigson are examined. The two corrections give similar results in the fully rough region, however, they vary in the transitionally rough regime. Three roughness boundary conditions for the wall function approach using $k-\omega$ SST turbulence model are also compared. It is observed that the consistency of boundary conditions for k, ω and ν_t ensures superior results. The roughness extension of wall functions is validated by comparing with low-Re turbulence model simulations for flat-plate and NACA0012 cases with different values of

equivalent sand-grain roughness.

Different thermal corrections are incorporated and a comparative study is performed. It is observed that all three thermal corrections give a good result when compared with experimental cases. However, none of the corrections performs well for all the cases. A particularly interesting experimental case with two different roughness element types having the same skin-friction coefficient but different Stanton number distributions is also considered. As Aupoix correction incorporates an additional physical parameter namely corrected surface area ratio to account for wetted surface area effects, it gives good results for both the roughness elements that are tested. The other corrections were not able to replicate this behavior as they rely on a single parameter i.e. equivalent sand-grain roughness. Aupoix Correction for both low-Reynolds number turbulence model and wall function approaches seems to be an adequate model for simulating the effects of heat transfer over rough surfaces. However, the extraction of the corrected surface area parameter requires details of the rough surface geometry which is generally not provided with experiments. Even though the Aupoix correction is the most physical amongst the three corrections, in the presence of randomly-distributed rough surface, the other two thermal corrections for wall functions can be used as they give quantitatively acceptable results.

5.2 Limitations of the proposed solution

Extensions to incorporate the effect of roughness in both the low and high Reynolds number turbulence model face the following limitations.

5.2.1 Low-Re turbulence model

- The roughness extensions of low-Reynolds number turbulence model are based on the shift of the logarithmic region of the velocity profile. The logarithmic law is not valid at a low local Reynolds number. Therefore, the results at the rough leading edge are questionable. There is a lack of good experimental data for the heat transfer on rough airfoils to validate it.

5.2.2 High-Re turbulence model

- Wall function approach gives accurate results for flows at a high Reynolds number. At lower Reynolds number i.e. leading edge of the airfoil, the assumption of a fully developed turbulent flow while using wall functions leads to an overestimation of results.

- The wall function approach for rough walls may suffer from numerical restrictions i.e. for higher values of k_s, a fine mesh near the wall could decrease the convergence rate and the robustness.

- Wall functions are solved using the Newton-Raphson method which is sensitive to the initial condition. This can cause convergence issues at very high values of equivalent sand-grain roughness. This behavior is observed for the high angle of attack rough NACA 0012 case.

- The use of a single velocity scale for wall functions results in near-zero heat flux at the stagnation point.

5.3 Recommendations for future work

Roughness extensions for low and high-Reynolds number turbulence model provide good predictions of both C_f and St when accompanied by the appropriate thermal correction. These methods can be further improved. The recommendations for future work are as follows,

5.3.1 Low-Re turbulence model

- The convergence issues with roughness extensions for $k-\omega$ SST turbulence models are avoided in the present study by reducing the stiffness of the equation. This involves modification of k boundary condition from Dirichlet to Neumann and the use of a higher value of wall spacing ($y^+ \approx 0.3$). Convergence can be improved by solving the turbulence models equations differently and more work should be done to improve the robustness.

- Aupoix thermal correction yields promising results, however, it requires specification of two additional parameters. These parameters are rarely available for an irregular roughness case such as in situations involving icing. The low-Reynolds number turbulence models are more suitable for icing applications with their better leading edge predictions as compared to the wall function approach which gives near-zero wall heat flux at the stagnation point. Owen and Dipprey thermal corrections of wall functions should be extended to low-Reynolds turbulence model method as they require only a single input parameter and give good results for most of the validation cases. Thermal diffusivity models can be extended to rough surfaces to serve this purpose.

5.3.2 High-Re turbulence model

- Assumptions behind the wall function approach fail in the leading edge region. Therefore, this approach should be followed by an adaptive approach which switches to the low-Reynolds turbulence model approach at low values of y^+ and at the leading edge. As the wall functions give good results over a large range of y^+, meshes with the local refinement at the leading edge can also be tested.

- The rough wall functions that are implemented are based on an incompressible flow assumption. As roughness studies are mostly conducted on an incompressible flat plate, this is a viable assumption. For more general applications, they should be extended to compressible flows.

- Robustness of wall function approach can be further improved by using better relaxation techniques that are not very sensitive to the initial guess.

- Wall functions with two velocity scales would lead to better predictions in the stagnation region (Lacombe et al., 2019). The use of two scales in the wall function approach is limited to two-equation turbulence models. The boundary condition of turbulence models used in the current approach makes it ill-conditioned to use turbulent kinetic energy as a second velocity scale. Therefore, a different boundary condition must be tested for this approach. The other boundary condition which is found in the literature using two velocity scale wall functions is also tested. However, for rough walls, the boundary condition leads to discrepancy in results and convergence issues at high values of equivalent sand-grain roughness ($k_s^+ \approx 500$). More work in this direction is needed.

- Immersed boundary method (IBM) is a promising prospect for ice-shape prediction simulations as it eases the mesh generation requirement over a complicated iced geometry. Wall functions are frequently utilized to provide adequate boundary condition for IBM. The wall function approach presented in this thesis is robust and gives good predictions of heat transfer on rough surfaces for a large range of k_s^+/y^+. An interesting prospect could be to use the wall functions with IBM code and gauge its performance for the ice-shape prediction.

REFERENCES

Acharya, M. , Bornstein, J. , and Escudier, M. P. , "Turbulent boundary layers on rough surfaces", *Experiments in Fluids*, vol. 4, no. 1, pp. 33–47, 1986. DOI: 10.1007/BF00316784

Allen, J. J. , Shockling, M. A. , Kunkel, G. J. , and Smits, A. J. , "Turbulent flow in smooth and rough pipes", *Philosophical Transactions of the Royal Society A: Mathematical, Physical and Engineering Sciences*, vol. 365, no. 1852, pp. 699–714, 2007. DOI: 10.1098/rsta.2006.1939

Allmaras, S. , Johnson, F. , and Spalart, P. , "Modifications and clarifications for the implementation of the spalart-allmaras turbulence model", in *Seventh International Conference on Computational Fluid Dynamics (ICCFD7)*, 2012, pp. 1–11.

Apsley, D. , "Cfd calculation of turbulent flow with arbitrary wall roughness", *Flow, Turbulence and Combustion*, vol. 78, no. 2, pp. 153–175, 2007. DOI: 10.1007/s10494-006-9059-x

Arpaci, V. and Larsen, P. , *Convection Heat Transfer*. Prentice Hall, 1984.

Aupoix, B. , "A General Strategy to Extend Turbulence Models to Rough Surfaces: Application to Smith's k-L Model", *Journal of Fluids Engineering*, vol. 129, no. 10, p. 1245, 2007. DOI: 10.1115/1.2776960

Aupoix, B. , "Roughness Corrections for the k–ω Shear Stress Transport Model: Status and Proposals", *Journal of Fluids Engineering*, vol. 137, no. 2, p. 021202, 2014. DOI: 10.1115/1.4028122

Aupoix, B. , "Improved heat transfer predictions on rough surfaces", *International Journal of Heat and Fluid Flow*, vol. 56, pp. 160–171, 2015. DOI: 10.1016/j.ijheatfluidflow.2015.07.007

Aupoix, B. and Spalart, P. R. , "Extensions of the Spalart - Allmaras turbulence model to account for wall roughness", *International Journal of Heat and Fluid Flow*, vol. 24, no. 4, pp. 454–462, 2003. DOI: 10.1016/S0142-727X(03)00043-2

Bettermann, D. , "Contribution à l'étude de la couche limite turbulente le long de plaques rugueuses", Center National de la Recherche Scientifique, Tech. rep. 65-6, 1965.

Bons, J. , "A Critical Assessment of Reynolds Analogy for Turbine Flows", *Journal of Heat Transfer*, vol. 127, no. 5, p. 472, 2005. DOI: 10.1115/1.1861919

Bourgault-Cote, S. and Laurendeau, E. , "Two-Dimensional/Infinite Swept Wing Ice Accretion Model", in *53rd AIAA Aerospace Sciences Meeting*, series AIAA SciTech Forum. American Institute of Aeronautics and Astronautics, 2015. DOI: 10.2514/6.2015-0535

Bradshaw, P. , "A note on "critical roughness height" and "transitional roughness"", *Physics of Fluids*, vol. 12, no. 6, pp. 1611–1614, 2000. DOI: 10.1063/1.870410

Bradshaw, P. and Huang, P. G. , "The law of the wall in turbulent flow", in *Proceedings of Osborne Reynolds Centenary Symposium*, Manchester, England, UK, 1995, pp. 165–188.

Carlson, J.-R. , Vatsa, V. , and White, J. A. , "Node-Centered Wall Function Models for the Unstructured FLow Code Fun3D", in *22nd AIAA Computational Fluid Dynamics Conference*, series AIAA AVIATION Forum. American Institute of Aeronautics and Astronautics, 2015. DOI: 10.2514/6.2015-2758

Center, N. L. R. . (2018) Turbulence modelling resource. Retrieved from URL: https://turbmodels.larc.nasa.gov/

Chedevergne, F. , "Analytical wall function including roughness corrections", *International Journal of Heat and Fluid Flow*, vol. 73, no. August, pp. 258–269, 2018. DOI: 10.1016/j.ijheatfluidflow.2018.08.001

Chedevergne, F. and Aupoix, B. , "Accounting for wall roughness effects in turbulence models : a wall function approach", 7^{th} *European Conference for Aeronautics and Aerospace Sciences (EUCASS)*, 2017. DOI: 10.13009/EUCASS2017-372

Chien, K. Y. , "Predictions of Channel and Boundary-Layer Flows with a Low-Reynolds-Number Turbulence Model", *AIAA Journal*, vol. 20, no. 1, pp. 33–38, 1982. DOI: 10.2514/3.51043

Chitsomboon, T. , "Effects of Artificial Viscosity on the Accuracy of High-Reynolds-Number k - ϵ Turbulence Model", Institute for Computational Mechanics in Propulsion, Lewis Research Center, Cleveland, Ohio, Tech. rep., 1994.

Colebrook, C. F. and White, C. M. , "Experiments with fluid friction in roughened pipes", *Proceedings of the Royal Society of London A: Mathematical, Physical and Engineering Sciences*, vol. 161, no. 906, pp. 367–381, 1937. DOI: 10.1098/rspa.1937.0150

Coleman, H. W. , Hodge, B. K. , and Taylor, R. P. , "Generalized Roughness Effects on Turbulent Boundary Layer Heat Transfer", Mississippi State University, ADA141943, Tech. rep., 1983.

Craft, T. J. , Gerasimov, A. V. , Iacovides, H. , and Launder, B. E. , "Progress in the generalization of wall-function treatments", *International Journal of Heat and Fluid Flow*, vol. 23, no. 2, pp. 148–160, 2002. DOI: 10.1016/S0142-727X(01)00143-6

Danvin, F. , Mathiaud, J. , and Aupoix, B. , "Study on k-ω shear stress transport model corrections applied to rough wall turbulent hypersonic boundary layers", in 7^{th} *European Conference For Aeronautics And Space Sciences (EUCASS)*, 2017. DOI: 10.13009/EUCASS2017-604

Dipprey, D. and Sabersky, R. , "Heat and momentum transfer in smooth and rough tubes at various prandtl numbers", *International Journal of Heat and Mass Transfer*, vol. 6, no. 5, pp. 329–353, 1963. DOI: 10.1016/0017-9310(63)90097-8

Dirling, J. , "A method for computing roughwall heat transfer rates on reentry nosetips", *8th Thermophysics Conference*, no. 73, 1973. DOI: 10.2514/6.1973-763

Dukhan, N. , Masiulaniec, K. C. , De Witt, K. J. , and Van Fossen, G. J. , "Acceleration effect on the stanton number for castings of ice-roughened surfaces", *Journal of Aircraft*, vol. 36, no. 5, pp. 896–898, 1999. DOI: 10.2514/2.2527

Durbin, P. A. , "Limiters and wall treatments in applied turbulence modeling", *Fluid Dynamics Research*, vol. 41, no. 1, p. 012203, 2009. DOI: 10.1088/0169-5983/41/1/012203

Dvorak, F. A. , "Calculation of turbulent boundary layers on rough surfaces in pressure gradient." *AIAA Journal*, vol. 7, no. 9, pp. 1752–1759, 1969. DOI: 10.2514/3.5386

Eça, L. and Hoekstra, M. , "Numerical aspects of including wall roughness effects in the SST k-ω eddy-viscosity turbulence model", *Computers and Fluids*, vol. 40, no. 1, pp. 299–314, 2011. DOI: 10.1016/j.compfluid.2010.09.035

Flack, K. A. and Schultz, M. P. , "Review of Hydraulic Roughness Scales in the Fully Rough Regime", *Journal of Fluids Engineering*, vol. 132, no. 4, p. 041203, 2010. DOI: 10.1115/1.4001492

Fuhrman, D. R. , Dixen, M. , and Jacobsen, N. G. , "Physically-consistent wall boundary conditions for the k-ω turbulence model", *Journal of Hydraulic Research*, vol. 48, no. 6, pp. 793–800, 2010. DOI: 10.1080/00221686.2010.531100

Gant, S. , "Development and Application of a New Wall Function for Complex Turbulent Flows", PhD thesis, University of Manchester Institute of Science and Technology, U.K., 2002. Retrieved from URL: http://s177835660.websitehome.co.uk/research/THESIS/thesis.pdf

Goldberg, U. and Batten, P. , "Rough Surface Wall Function Treatment With Single Equation Turbulence Models", *Journal of Fluids Engineering*, vol. 139, no. 8, p. 081204, 2017. DOI: 10.1115/1.4036245

Grabow, R. M. and White, C. O. , "Surface Roughness Effects Nosetip Ablation Characteristics", *AIAA Journal*, vol. 13, no. 5, pp. 605–609, 1975. DOI: 10.2514/3.49772

Grigson, C. , "Drag losses of new ships caused by hull finish", *Journal of Ship Research*, vol. 36, pp. 182–196, 1992.

Hasanzadeh, K. , Laurendeau, E. , and Paraschivoiu, I. , "Grid-Generation Algorithms for Complex Glaze-Ice Shapes Reynolds-Averaged Navier-Stokes Simulations", *AIAA Journal*, vol. 54, no. 3, pp. 847–860, 2016. DOI: 10.2514/1.J054076

Healzer, J. , Moffat, R. , and Kays, W. , "The turbulent boundary layer on a porous, rough plate - Experimental heat transfer with uniform blowing", in *Thermophysics and Heat Transfer Conference*, series Fluid Dynamics and Co-located Conferences. American Institute of Aeronautics and Astronautics, 1974. DOI: 10.2514/6.1974-680

Hellsten, A. , Laine, S. , Hellsten, A. , and Laine, S. , "Extension of the k-ω-SST turbulence model for flows over rough surfaces", in *22nd Atmospheric Flight Mechanics Conference*, series Guidance, Navigation, and Control and Co-located Conferences. American Institute of Aeronautics and Astronautics, 1997. DOI: 10.2514/6.1997-3577

Hosni, M. H. , "Measurement and calculation of surface roughness effects on turbulent flow and heat transfer", PhD thesis, Mississipi State University, U.S.A, 1989.

Retrieved from URL: https://search.proquest.com/docview/303809868?accountid=40695

Hosni, M. H. , Coleman, H. W. , Garner, J. W. , and Taylor, R. P. , "Roughness element shape effects on heat transfer and skin friction in rough-wall turbulent boundary layers", *International Journal of Heat and Mass Transfer*, vol. 36, no. 1, pp. 147–153, 1993. DOI: 10.1016/0017-9310(93)80074-5

Hosni, M. , Coleman, H. , and Taylor, R. , "Measurements and calculations of rough-wall heat transfer in the turbulent boundary layer", *Journal of Heat and Mass Transfer*, vol. 34, no. 4-5, pp. 1067–1082, 1991. DOI: 10.1016/0017-9310(91)90017-9

Jameson, A. , Schmidt, W. , and Turkel, E. L. I. , "Numerical solution of the Euler equations by finite volume methods using Runge Kutta time stepping schemes", in *14th Fluid and Plasma Dynamics Conference*, series Fluid Dynamics and Co-located Conferences. American Institute of Aeronautics and Astronautics, 1981. DOI: 10.2514/6.1981-1259

Jayatillaka, C. , "The influence of prandtl number and surface roughness on the resistance of the laminar sub-layer to momentum and heat transfer", *Progress in Heat and Mass Transfer*, p. 1:193, 1969.

Jiménez, J. , "Turbulent flows over rough walls", *Annual Review of Fluid Mechanics*, vol. 36, no. 1, pp. 173–196, 2004. DOI: 10.1146/annurev.fluid.36.050802.122103

Kader, B. A. and Yaglom, A. M. , "Heat and mass transfer laws for fully turbulent wall flows", *International Journal of Heat and Mass Transfer*, vol. 15, no. 12, pp. 2329–2351, 1972. DOI: 10.1016/0017-9310(72)90131-7

Kader, B. , "Temperature and concentration profiles in fully turbulent boundary layers", *International Journal of Heat and Mass Transfer*, vol. 24, no. 9, pp. 1541 – 1544, 1981. DOI: 10.1016/0017-9310(81)90220-9

Kalitzin, G. , Medic, G. , Iaccarino, G. , and Durbin, P. , "Near-wall behavior of rans turbulence models and implications for wall functions", *Journal of Computational Physics*, vol. 204, no. 1, pp. 265 – 291, 2005. DOI: 10.1016/j.jcp.2004.10.018

Kays, W. and Crawford, M. , *Convective Heat and Mass Transfer*, 3rd ed. McGraw-Hill, New-York, 1993.

Knopp, T. , Alrutz, T. , and Schwamborn, D. , "A grid and flow adaptive wall-function method for RANS turbulence modelling", *Journal of Computational Physics*, vol. 220, no. 1, pp. 19–40, 2006. DOI: 10.1016/j.jcp.2006.05.003

Knopp, T. , Eisfeld, B. , and Calvo, J. B. , "A new extension for k-ω turbulence models to account for wall roughness", *International Journal of Heat and Fluid Flow*, vol. 30, no. 1, pp. 54–65, 2009. DOI: 10.1016/j.ijheatfluidflow.2008.09.009

Kontogiannis, A. , Prakash, A. , Laurendeau, E. , and Moens, F. , "Sensitivity of Glaze Ice Accretion and Iced Aerodynamics Prediction to Roughness", in *26th Annual Conference of the Computational Fluid Dynamics Society of Canada*, Winnipeg, Manitoba, 2018.

Lacombe, F. , Pelletier, D. , and Garon, A. , "Compatible wall functions and adaptive remeshing for the k-ω SST model", *AIAA Scitech 2019 Forum*, pp. 1–20, 2019. DOI: 10.2514/6.2019-2329

Launder, B. and Spalding, D. , "The numerical computation of turbulent flows", *Computer Methods in Applied Mechanics and Engineering*, vol. 3, no. 2, pp. 269–289, 1974. DOI: 10.1016/0045-7825(74)90029-2

Lavoie, P. , "Modeling of thin water films on swept wings in icing condition", PhD thesis, Polytechnique Montreal, 2017. Retrieved from URL: https://publications.polymtl.ca/2558/

Ligrani, P. M. and Moffat, R. J. , "Structure of transitionally rough and fully rough turbulent boundary layers", *Journal of Fluid Mechanics*, vol. 162, p. 69–98, 1986. DOI: 10.1017/S0022112086001933

MacDonald, M. , Hutchins, N. , and Chung, D. , "Roughness effects in turbulent forced convection", *Journal of Fluid Mechanics*, vol. 861, p. 138–162, 2019. DOI: 10.1017/jfm.2018.900

McClain, S. T. , Hodge, B. K. , and Bons, J. P. , "Predicting Skin Friction and Heat Transfer for Turbulent Flow Over Real Gas Turbine Surface Roughness Using the Discrete Element Method", *Journal of Turbomachinery*, vol. 126, no. 2, pp. 259–267, 2004. DOI: 10.1115/1.1740779

Medida, S. , Baeder, J. D. , Nigam, N. , and Chen, P. , "Variable Surface Roughness Modeling for Skin Friction", *52nd Aerospace Sciences Meeting*, pp. 1–18, 2014. DOI: 10.2514/6.2014-0587

Menter, F. R. , "Two-equation eddy-viscosity turbulence models for engineering applications", *AIAA Journal*, vol. 32, no. 8, pp. 1598–1605, 1994. DOI: 10.2514/3.12149

Menter, F. R. , Ferreira, J. , Esch, T. , and Konno, B. , "The SST Turbulence Model with Improved Wall Treatment for Heat Transfer Predictions in Gas Turbines", *International Gas Turbine Congress 2003*, pp. 1–7, 2003.

Mills, A. F. and Hang, X. , "On the Skin Friction Coefficient for a Fully Rough Flat Plate", *Journal of Fluids Engineering*, vol. 105, no. 3, pp. 364–365, 1983. DOI: 10.1115/1.3241008

Montreuil, E. , Chazottes, A. , Guffond, D. , Murrone, A. , Caminade, F. , and Catris, S. , "ECLIPPS: 1. Three-Dimensional CFD Prediction of the Ice Accretion", in *1st AIAA Atmospheric and Space Environments Conference*. American Institute of Aeronautics and Astronautics, 2009. DOI: 10.2514/6.2009-3969

Moody, L. , "Friction factors for pipe flow", *Trans. ASME*, no. 8, pp. 671–677, 1944.

Nichols, R. H. and Nelson, C. C. , "Wall Function Boundary Conditions Including Heat Transfer and Compressibility", *AIAA Journal*, vol. 42, no. 6, pp. 1107–1114, 2004. DOI: 10.2514/1.3539

Nikuradse, J. , "Laws of flow in rough pipes", *VDI Forschungsheft*, p. 361, 1933.

Nunner, W. , "Heat transfer and pressure drop in rough tubes", *VDI Forschungsheft*, vol. 22, no. 455, pp. 5–39, 1956.

Owen, P. R. and Thomson, W. R. , "Heat transfer across rough surfaces", *Journal of Fluid Mechanics*, vol. 15, no. 3, pp. 321–334, 1963. DOI: 10.1017/S0022112063000288

Perry, A. E. , Schofield, W. H. , and Joubert, P. N. , "Rough wall turbulent boundary layers", *Journal of Fluid Mechanics*, vol. 37, no. 02, p. 383, 1969. DOI: 10.1017/S0022112069000619

Pigeon, A. , Levesque, A. T. , and Laurendeau, E. , "Two-dimensional navier-stokes flow solver developments at École polytechnique de montréal", in *CFD Society of Canada 22nd Annual Conference*, Toronto, CA, 2014.

Pimenta, M. M. , Moffat, R. J. , and Kays, W. M. , "The turbulent boundary layer: An experimental study of the transport of momentum and heat with the effect of roughness", Thermosciences Division, Department of Mechanical Engineering, Stanford University, Tech. rep. HMT-21, 1975.

Poinsatte, P. E. , Van Fossen, G. J. , and De Witt, K. J. , "Roughness effects on heat transfer from a NACA 0012 airfoil", *Journal of Aircraft*, vol. 28, no. 12, pp. 908–911, 1991. DOI: 10.2514/3.46116

Popovac, M. and Hanjalic, K. , "Compound wall treatment for rans computation of complex turbulent flows and heat transfer", *Flow, Turbulence and Combustion*, vol. 78, no. 2, p. 177, 2007. DOI: 10.1007/s10494-006-9067-x

Prakash, A. and Laurendeau, E. , "A wall function approach to account for rough surface heat transfer in spalart-allmaras turbulence model", in *AIAA Aviation 2019 Forum*, 2019. DOI: 10.2514/6.2019-2918

Press, W. H. , Teukolsky, S. A. , Vetterling, W. T. , and Flannery, B. P. , *Numerical Recipes in C: The Art of Scientific Computing*, 2nd ed. Cambridge University Press, 1992.

Radenac, E. , Kontogiannis, A. , Bayeux, C. , and Villedieu, P. , "An extended rough-wall model for an integral boundary layer model intended for ice accretion calculations", in *Atmospheric and Space Environments Conference*, 2018. DOI: 10.2514/6.2018-2858

Reichardt, H. , "Vollständige darstellung der turbulenten geschwindigkeitsverteilung in glatten leitungen", *ZAMM - Journal of Applied Mathematics and Mechanics / Zeitschrift für Angewandte Mathematik und Mechanik*, vol. 31, no. 7, pp. 208–219, 1951. DOI: 10.1002/zamm.19510310704

Reynolds, W. , Kays, W. M. , and Kline, S. J. , "Heat Transfer in Turbulent Boundary Incompressible boundary layer I - Constant Wall Temperature", NASA Memorandum, Tech. rep., 1958.

Rohatgi, A. . (2018) Webplotdigitizer (version = 4.1). Retrieved from URL: https://automeris.io/WebPlotDigitizer

Rotta, J. C. , "Turbulent boundary layers in incompressible flow", *Progress in Aerospace Sciences*, vol. 2, no. 1, pp. 1–95, 1962. DOI: 10.1016/0376-0421(62)90014-3

Schlichting, H. , "Experimentelle Untersuchungen zum Rauhigkeits-problem", *Ingenieur-Archiv VII*, vol. 1, 1936.

Sondak, D. L. , "Wall functions for the k-epsilon turbulence model in generalized nonorthogonal curvilinear coordinates", PhD thesis, Iowa State University, 1992. Retrieved from URL: https://lib.dr.iastate.edu/rtd/9954

Spalart, P. and Allmaras, S. , "A one-equation turbulence model for aerodynamic flows", in *30th Aerospace Sciences Meeting and Exhibit*, series Aerospace Sciences Meetings. American Institute of Aeronautics and Astronautics, 1992. DOI: 10.2514/6.1992-439

Spalding, D. B. , "A Single Formula for the "Law of the Wall"", *Journal of Applied Mechanics*, vol. 28, no. 3, pp. 455–458, 1961. DOI: 10.1115/1.3641728

Suga, K. , Craft, T. , and Iacovides, H. , "An analytical wall-function for turbulent flows and heat transfer over rough walls", *International Journal of Heat and Fluid Flow*, vol. 27, no. 5, pp. 852 – 866, 2006, special issue of the 6th International Symposium on Engineering Turbulence Modelling and Measurements – ETMM6. DOI: j.ijheatfluidflow.2006.03.011

Swanson, R. C. and Turkel, E. , "Multistage Schemes with Multigrid for Euler and Navier-Strokes Equations: Components and Analysis", *NASA Report*, no. August 1997, p. 83, 1997.

Tarada, F. , "Heat transfer to rough turbine blading", PhD thesis, University of Sussex, Brington, England, 1987. Retrieved from URL: https://ethos.bl.uk/OrderDetails.do?uin=uk.bl.ethos.379448

Taylor, R. P. , Coleman, H. W. , and Hodge, B. K. , "Prediction of Turbulent Rough-Wall Skin Friction Using a Discrete Element Approach", *Journal of Fluids Engineering*, vol. 107, no. 2, pp. 251–257, 1985. DOI: 10.1115/1.3242469

Townsend, A. , *The Structure of Turbulent Shear Flow*, 2nd ed. Cambridge University Press, 1976.

Waigh, D. R. and Kind, R. J. , "Improved Aerodynamic Characterization of Regular Three-Dimensional Roughness", *AIAA Journal*, vol. 36, no. 6, pp. 1117–1119, 1998. DOI: 10.2514/2.491

Wilcox, D. C. , "Reassessment of the scale-determining equation for advanced turbulence models", *AIAA Journal*, vol. 26, no. 11, pp. 1299–1310, 1988. DOI: 10.2514/3.10041

Wilcox, D. C. , "Formulation of the k-w Turbulence Model Revisited", *AIAA Journal*, vol. 46, no. 11, pp. 2823–2838, 2008. DOI: 10.2514/1.36541

Wilcox, D. , *Turbulence Modeling for CFD*. DCW Industries Inc., 1994.

Yoder, D. A. , "Comparison of Turbulent Thermal Diffusivity and Scalar Variance Models", in *54th AIAA Aerospace Sciences Meeting*, series AIAA SciTech Forum. American Institute of Aeronautics and Astronautics, 2016. DOI: 10.2514/6.2016-1561

Zhu, J. and Shih, T.-H. , "An NPARC turbulence module with wall functions", in *34th Aerospace Sciences Meeting and Exhibit*, series Aerospace Sciences Meetings. American Institute of Aeronautics and Astronautics, 1996. DOI: 10.2514/6.1996-382

APPENDIX A COMPARISON OF DIFFERENT WALL FUNCTION PROFILES

Log-law based wall functions are implemented in NSCODE as part of this study. Wall function results are known to depend on the near wall spacing (y^+). For complicated geometries, it is difficult to limit y^+ within a certain range of values. Therefore, it is important to assess the variation of results with near wall spacing and give suggestions to reduce it. This appendix compares different velocity and temperature profiles to assess their performance for the 2-D zero pressure gradient flat plate case. Similar observations are also observed for the NACA 0012 airfoil case, however, they are not presented.

Velocity profile

The following velocity wall function profiles are tested to understand the effect of the profile on mesh dependency characteristics of wall functions.

- Standard wall function (Eq. (2.27))
- Spalding wall function (Spalding, 1961, Eq. (2.33))
- Reichardt wall function (Reichardt, 1951, Eq. (2.34))
- Knopp wall function (Knopp et al., 2006, Eq. (2.35) and Eq. (2.36))
- Spalart-Allmaras wall model (Allmaras et al., 2012, Eq. (2.38))
- Look-up table (Kalitzin et al., 2005)

The different velocity profiles are shown in Figure A.1. A 2-D zero pressure gradient flat plate case by NASA Turbulence Modeling Resource (Center (2018)) is used to compare the different profiles. The case parameters and first cell height for different test meshes are mentioned in Table 4.3. The standard wall function formulation used is slightly different from Eq. (2.27). Here, the shift from the viscous sublayer to logarithmic profile is done at $y^+ = 11.25$. The slight overshoot in the velocity profile at the edge of the boundary layer is due to the use of artificial dissipation.

The results are presented for Spalart-Allmaras turbulence model in Figures A.2 - A.7. All the wall function profiles predict the skin-friction coefficient and velocity profile close to that the

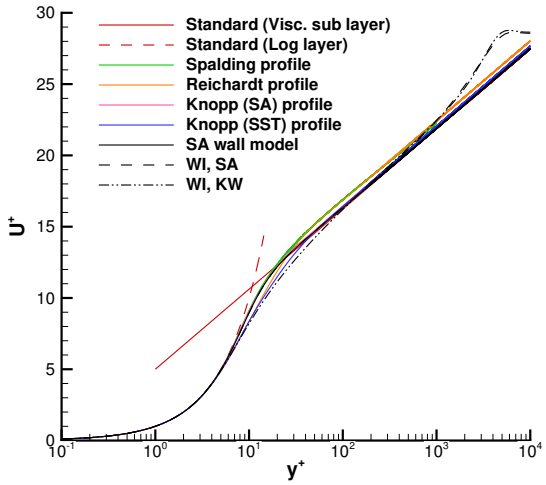

Figure A.1 Different velocity wall function profiles

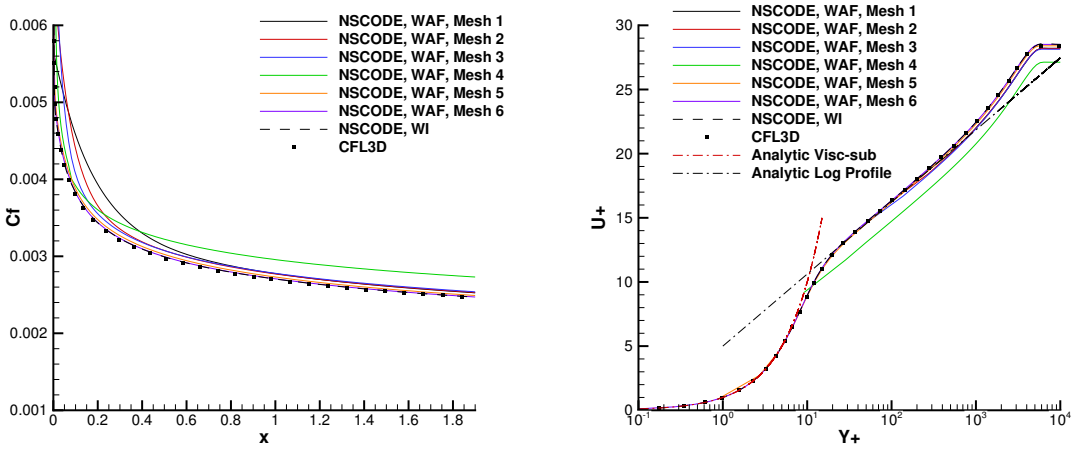

(a) (b)

Figure A.2 a) C_f distribution and b) velocity profile at $x = 1.9$ m for Standard log-law profile

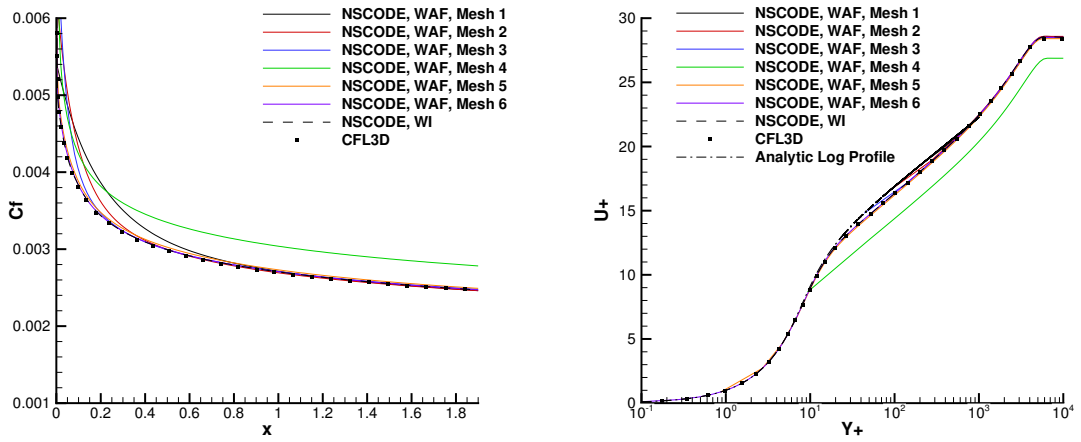

(a) (b)

Figure A.3 a) C_f distribution and b) velocity profile at $x = 1.9$ m for Spalding profile

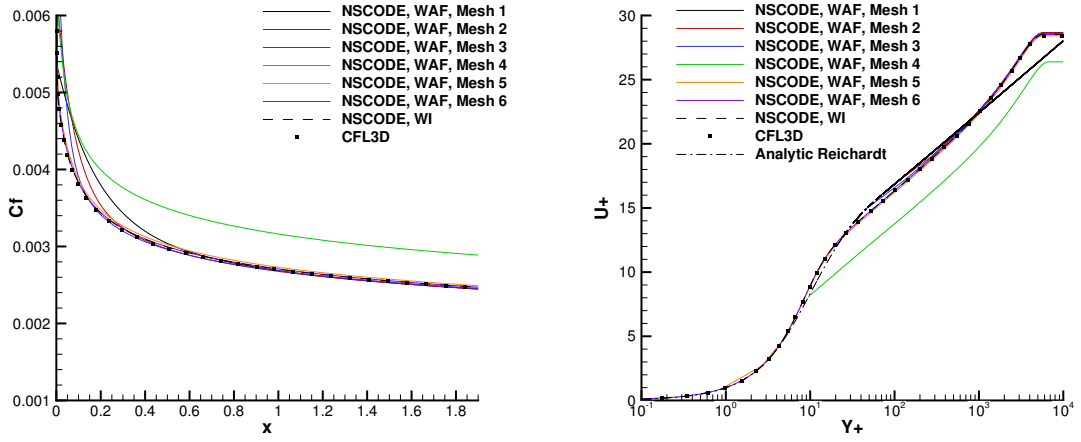

(a) (b)

Figure A.4 a) C_f distribution and b) velocity profile at $x = 1.9$ m for Reichardt profile

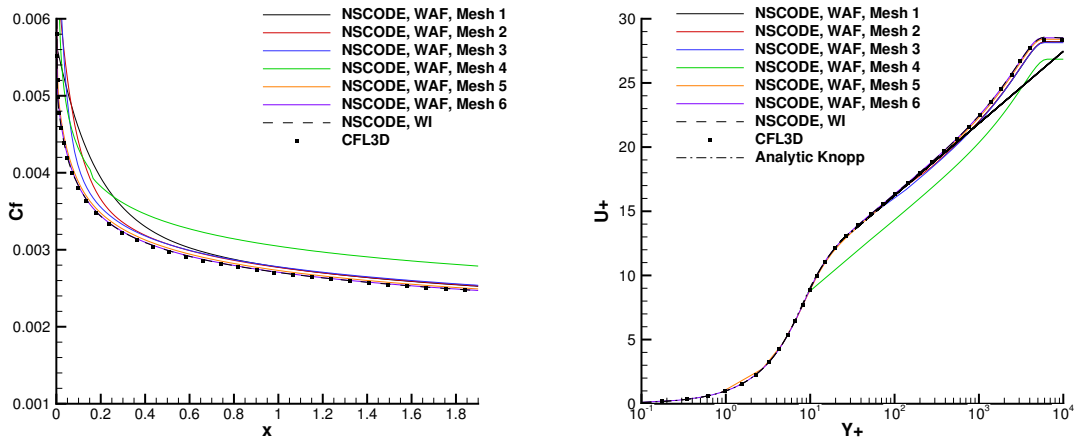

(a) (b)

Figure A.5 a) C_f distribution and b) velocity profile at $x = 1.9$ m for Knopp profile

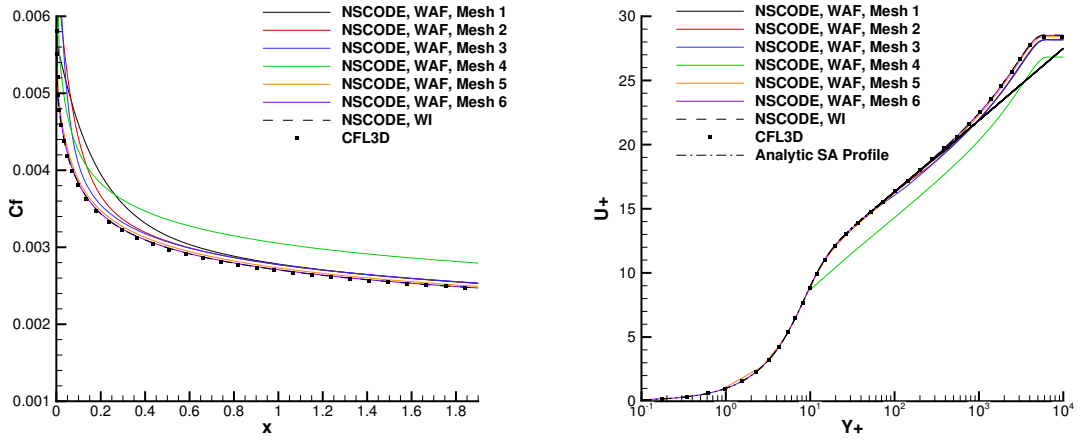

(a) (b)

Figure A.6 a) C_f distribution and b) velocity profile at $x = 1.9$ m for Spalart-Allmaras wall model

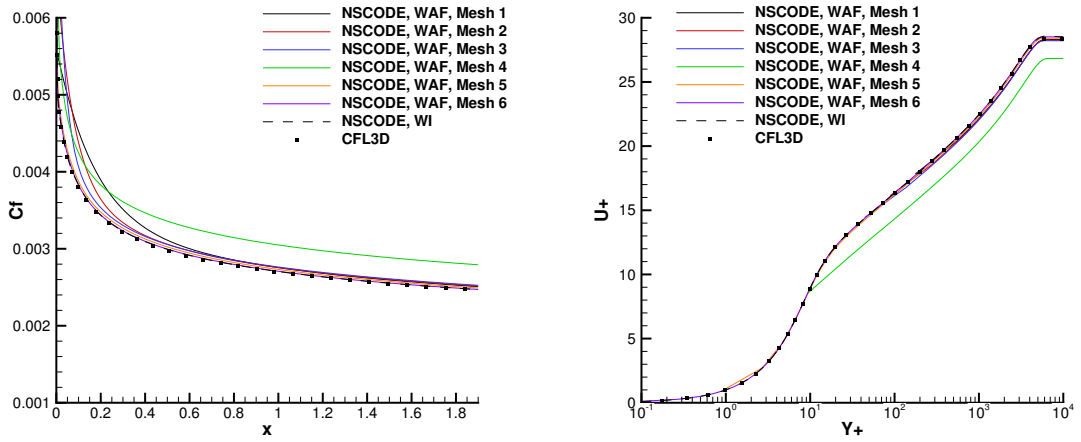

(a) (b)

Figure A.7 a) C_f distribution and b) velocity profile at $x = 1.9$ m for Look-up table approach

results obtained using the low-Re turbulence model approach (both NSCODE and CFL3D). The results for Spalding and Reichardt profiles are slightly better than the others. Spalart-Allmaras wall model and the look-up table approach use the velocity profile of the low-Re turbulence model approach. Still, the predictions are not as good as those obtained from Spalding and Reichardt profiles. This is due to the use of a coarse mesh for non-wall layer cells. There exist non-linearity of the gradients of velocity and turbulence variables in the near wall region and therefore, a coarse mesh leads to wrong computation of gradients and results in numerical errors. This argument is supported by Kalitzin et al. (2005), who remarked that the use of an exact turbulence model consistent wall function profile also does not give near-wall spacing independent solutions due to numerical errors. Artificial dissipation also affects the wall function results. This is discussed in Appendix B. Keeping these limitations in mind, Spalding profile is selected in the thesis as it gave the results that are closest to those from low-Re turbulence model simulations. $k-\omega$ SST turbulence model is also tested and the results lead to a similar conclusion. Hence, the results are not presented.

Viscous dissipation effect

The use of a compressible flow solver makes the temperature profile susceptible to the Mach number dependence. At higher Mach numbers i.e. ($Ma = 0.2$), this leads to dependence of temperature profile on the wall temperature input. The reason for this is the presence of the viscous dissipation term in the RANS energy equation. The magnitude of this term increases with Mach number. The term is considered negligible and is usually not modeled

in an incompressible flow solver. Therefore, incompressible flow solvers do not exhibit such behavior. The effect is quantified by carrying out low-Reynolds number turbulence model simulations at different Mach numbers.

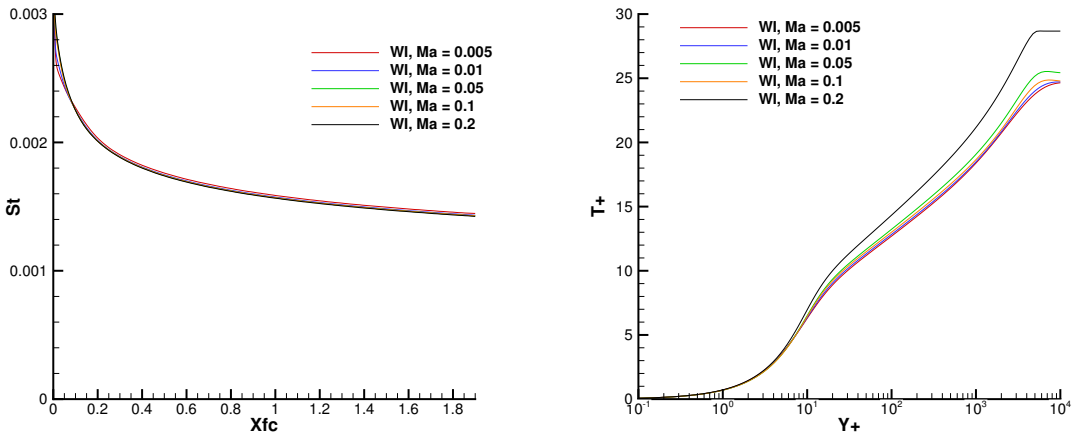

(a) (b)

Figure A.8 a) St distribution and b) temperature profile at $x = 1.9$m at different Mach numbers

From Figure A.8, it is observed that with the decrease in Mach number from $Ma = 0.2$ to $Ma = 0.1$, the temperature profile changes considerably. It seems to converge at lower values of Mach number. However, the computed Stanton number does not show a significant variation. Note that the Stanton number is computed using Eq. (3.1). This shows that the comparison of the temperature profile with the semi-analytic temperature profile at higher Mach number is not ideal. As the law of the wall is derived using an incompressible flow assumption, the comparison of the temperature profile should be made at conditions under which the magnitude of the viscous dissipation is small. Agreement in results for wall functions with those from low-Re turbulence model simulations is a good validation parameter. Note that the Van-Driest transformation is often used in a compressible flow regime to transform flow variables so that they match the semi-analytic solution. This transformation is typically used for high Mach number flows. With this transformation, the profiles are expected to match even at higher Mach numbers. As the work in this thesis comprises of cases with $Ma < 0.35$, the transformation is not used.

Temperature profile

The following temperature profiles are tested in conjunction with an isothermal wall boundary condition.

- Kader wall function (Kader, 1981, Eq. (2.40))
- Jayatillaka wall function(Jayatillaka, 1969, Eq. (2.42))
- Arpaci wall function (Arpaci and Larsen, 1984, Eq. (2.44))
- Look-up table approach (Kalitzin et al., 2005)

The various temperature profiles are compared in Figure A.9. The case parameters are similar to the velocity profile case. The overshoot in the temperature profile at the edge of the boundary layer might be due to the artificial dissipation.

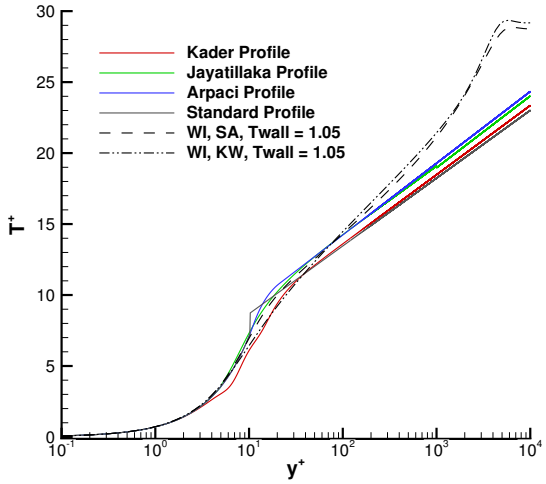

Figure A.9 Different temperature wall function profiles

Figures A.10 - A.13 shows the results for Spalart-Allmaras turbulence model. All the temperature profiles give good agreement with the results from low-Re turbulence model simulations using NSCODE and semi-empirical equation by Reynolds et al. (1958) (Eq. (4.27)). Jayatillaka temperature profile gives the results that are closest to the low-Re turbulence model simulations. Arpaci profile gives close results as well, whereas, Kader profile leads to greater wall spacing dependence. In general St predictions are accurate, however, they show more near-wall spacing dependency as compared to C_f predictions. The results from the look-up table approach are not as good as that from Jayatillaka profile. The reason for this is

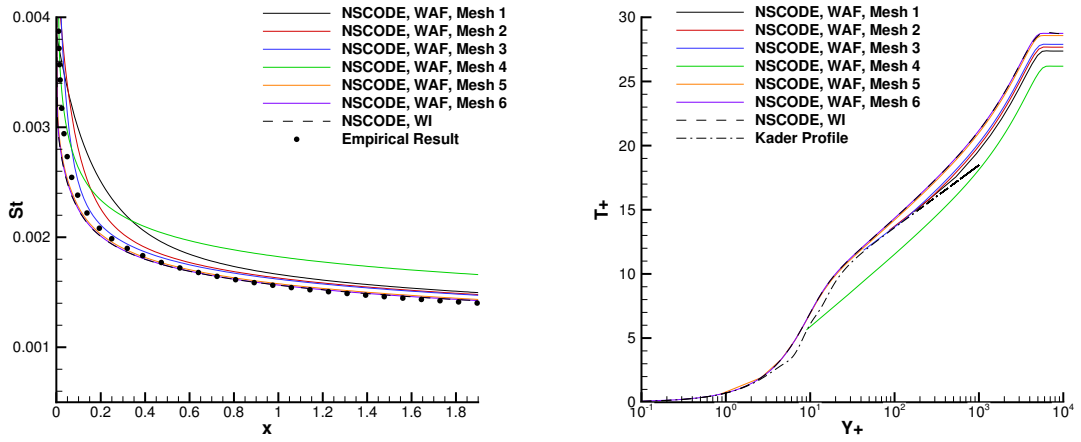

(a) (b)

Figure A.10 a) St distribution and b) temperature profile at $x = 1.9$ m for Kader temperature profile

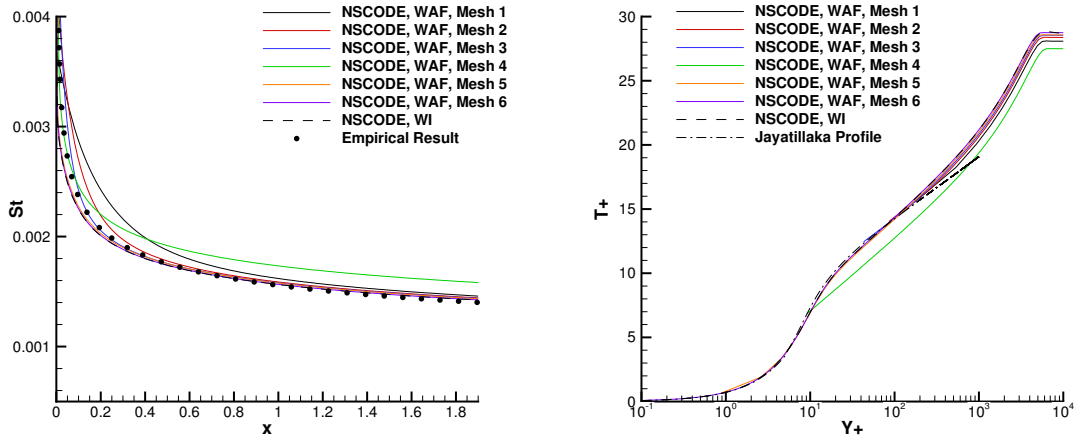

(a) (b)

Figure A.11 a) St distribution and b) temperature profile at $x = 1.9$ m for Jayatillaka temperature profile

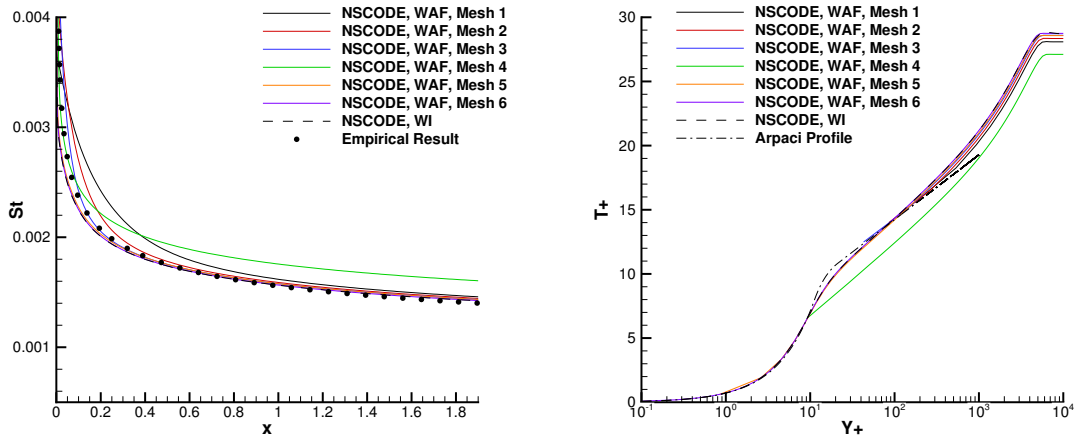

(a) (b)

Figure A.12 a) St distribution and b) temperature profile at $x = 1.9$ m for Arpaci temperature profile

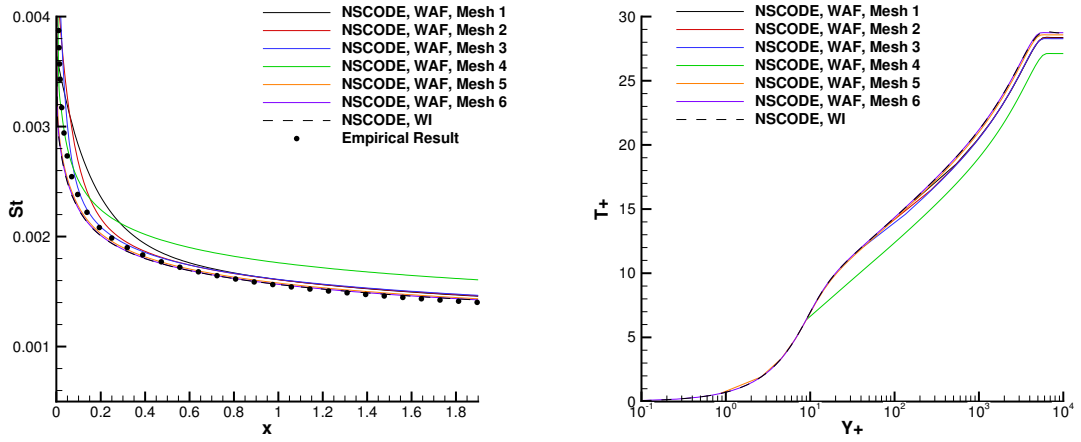

(a) (b)

Figure A.13 a) St distribution and b) temperature profile at $x = 1.9$ m for Look-up table approach

the same as the one explaining the discrepancy between the skin-friction coefficient results presented in Section A: Velocity profile.

APPENDIX B EFFECT OF ARTIFICIAL DISSIPATION ON WALL FUNCTION RESULTS

The wall function results obtained using the default artificial dissipation coefficients (i.e. $\kappa^{(2)} = \frac{1}{4}$ and $\kappa^{(4)} = \frac{1}{32}$) for a smooth flat plate case are not very close to the low-Re turbulence model results. This is attributed to the effect of the spatial discretization scheme, and the effect of artificial dissipation creeps into the solution of wall functions. The use of a coarse mesh results affects the calculated velocity gradient in the boundary layer leading to a large amount of dissipation being added, thereby reducing the accuracy (Chitsomboon, 1994). Zhu and Shih (1996) overcame this by turning off the artificial dissipation near the wall. Note that in NSCODE, RANS equations are discretized using centered 2^{nd} -order spatial scheme in space along with scalar and matrix dissipation. The present work uses matrix dissipation for all cases. Scalar dissipation leads to even higher discrepancy in wall function results. The two user-defined constants for these dissipation schemes are $\kappa^{(2)}$ and $\kappa^{(4)}$. The value for $\kappa^{(2)}$ is usually taken to be between $\frac{1}{4}$ and $\frac{1}{2}$, whereas, the value for $\kappa^{(4)}$ is normally between $\frac{1}{32}$ and $\frac{1}{64}$. $\kappa^{(2)}$ is mainly concerned with the resolution of sharp pressure gradients in the presence of shocks. For a zero-pressure gradient flat plate, it does not yield a significant difference. Nichols and Nelson (2004) remarked the effect of fourth-order dissipation term on the wall function results and suggested turning it off for the wall cells. Therefore, a parametric study to understand the effect of the value of $\kappa^{(4)}$ on wall function results is performed. For this study, several values of $\kappa^{(4)}$ between 1/32 and 1/1024 are tested. A 2-D zero-pressure gradient flat plate case from NASA turbulence modeling resource (Center, 2018) is tested. The case parameters are the same as those mentioned in Table 4.2. Mesh 2 from Table 4.3 is used to compare the effect of artificial dissipation on the wall function solution. Spalding (Eq. (2.33)) and Jayatillaka (Eq. (2.42)) profiles are used as velocity and temperature wall functions respectively. Other profiles also lead to similar observations.

The results are shown in Figure B.1. visc4 in the legend refers to $\kappa^{(4)}$. Larger value of $\kappa^{(4)}$ leads to higher C_f. As $\kappa^{(4)}$ reduces, the C_f becomes closer with the low-Re turbulence model result. Converging nature of the results is observed and further reduction of $\kappa^{(4)}$ doesn't yield significant changes. Similar behavior in the results is observed for St distribution as well. A lower value of $\kappa^{(4)}$ leads to the shift of the velocity and temperature profiles towards the low-Re turbulence model profile. $k-\omega$ SST turbulence model also shows similar dependence. It can be concluded that spatial discretization schemes have a significant impact on the accuracy of wall function simulations. Majority of the wall function literature lacked this information

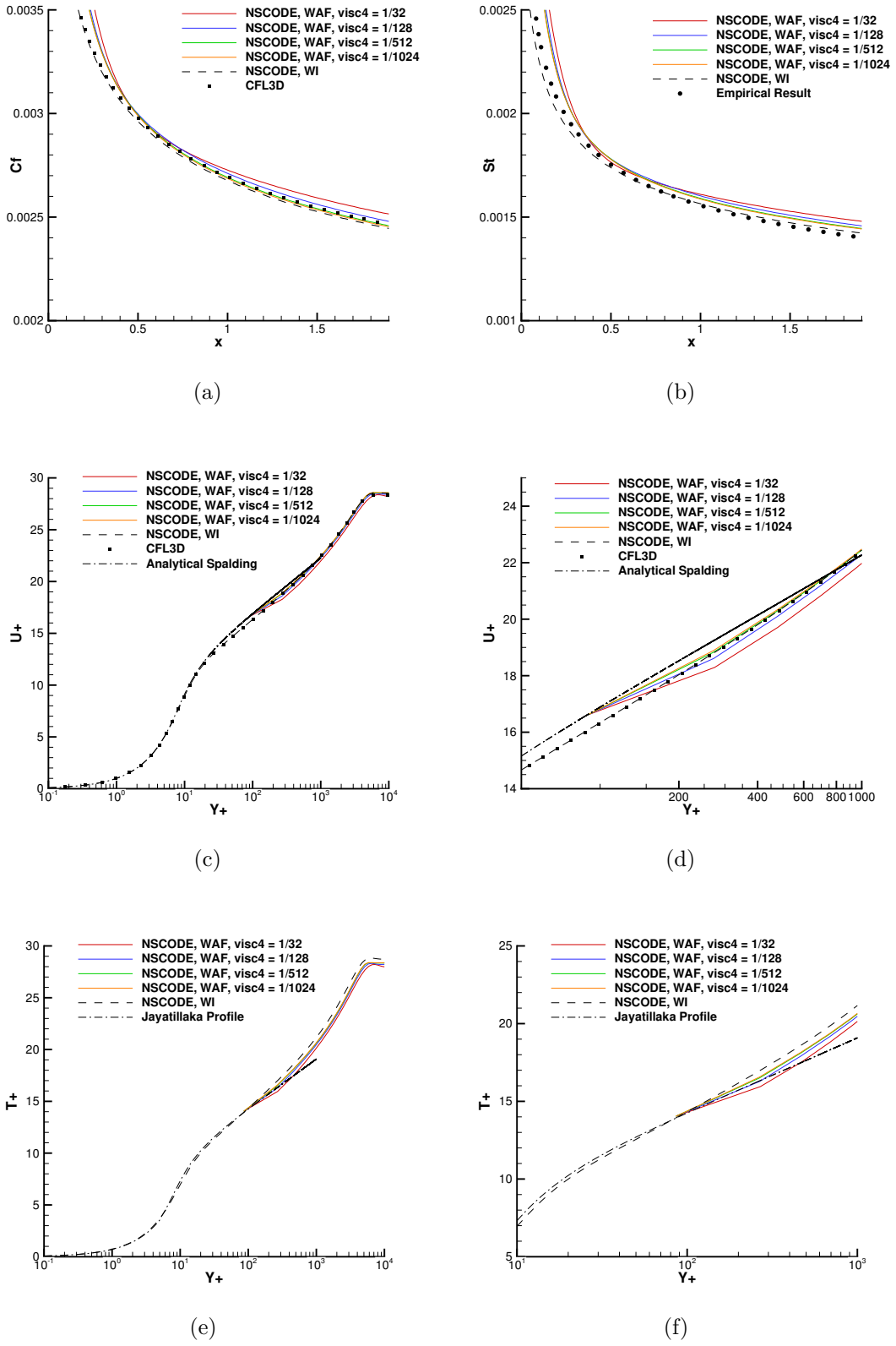

Figure B.1 Effect of artificial dissipation on a) C_f distribution, b) St distribution, c) Velocity profile at $x = 1.9$ m (d) Zoomed-in view), e) Temperature profile at $x = 1.9$ m (f) Zoomed-in view)

probably because other numerical schemes do not lead to similar errors. Nevertheless, this stresses the importance of a good study comparing different numerical schemes and analyzing their impact on wall function solutions. This is not the goal of the current thesis and therefore, only a concise parametric study is performed. For the verification and validation simulations in the flat plate case, $\kappa^{(4)} = \frac{1}{512}$ or $\frac{1}{1024}$ is taken. For NACA0012 case, such low values lead to numerical stability problem especially at a higher angle of attack. Therefore, for such cases, $\kappa^{(4)} = \frac{1}{128}$ is taken.